Investigation of SiC fiber reinforced metal matrix composites for nuclear fusion application

By

Yina Du

Contents

Acknowledgement

Time flies, and my almost 4-year doctoral career is coming to an end. First of all, I would like to thank my supervisors, Prof. Hinoki and Prof. Miyauchi. This dissertation was completed under the careful guidance from Prof. Hinoki and Prof. Miyauchi. Prof. Hinoki supports my work so much, no matter materials either or test, and gives me the most freedom in what I want to research. In addition, Prof. Hinoki gives me a lot of valuable suggestions and careful guidance about how to do research, how to write a research journal, and how to be a researcher. All in all, I have benefited from Prof Hinoki's influence on my academic career. I would deeply like to thank Prof. Miyauchi's encouragement and help not only in scientific research but also in life.

I would also like to thank Mr. Kawasaki, Mr. Shinoda, Mr. Hayshi, Mr. Omura, Prof. Nishihara and Dr. Takakura for all of their technical assistance and patient guidance about material fabrication and equipment operation etc. And also thanks to Dr. Nozawa and Dr. Ruan to help the tensile test at the high temperature, as well as Dr. Kondo to help coating films. I would like to thank Dr. Huang for giving me a lot of advice about research. Besides, I would like to express my appreciation to the member in Prof. Miyauchi's lab and Prof. Hinoki's group, Mr. Lee, Mr. Zhong, Mr. Wang, Mr. Wu, Mr. Kiyohara, Mr. Liu, Mr. Teranishi, and Mr. Nakamura for the help of my research and life.

In addition, many thanks to secretaries, Mrs. Fujiwara, Mrs. Wada and Mrs. Kitagawa, for the help about non-scientific parts of living. Besides, I am grateful to the MEXT scholarship for their financial support to live in Japan.

Finally, I would like to thank my parents for their support to pursue a PhD, and thank Ximalaya, Jinjiang and Qidian novel readers for bringing joy to me.

Abstract

High temperature refractory metals such as tungsten (W) and molybdenum (Mo) are promising candidates for structural and armor materials in fusion reactor applications. However, these body centered cubic (BCC) materials are prone to brittleness caused by neutron irradiation hardening and recrystallization at high temperatures. This results in a critical drawback for these materials, as the ductile brittle transition temperature (DBTT) can shift to higher than 900 °C for W. The conventional methods used to improve toughness have not been sufficient to meet the design requirements, making it necessary to develop new toughening mechanisms that allow metals to maintain their toughness even under embrittlement conditions. The objective of this work is to develop metal matrix composites by reinforcing them with silicon carbide (SiC) based fibers. SiC's strength is stable even after irradiation, making it an ideal reinforcement material. The underlying mechanism is similar to that of fiber reinforced ceramic composites, relying on energy dissipation through debonding and friction at the fiber/matrix interface.

Typically, long fiber reinforced composites consist of fiber, matrix and interface. Composites with various fiber architectures including unidirectional (UD) Hi-Nicalon type S SiC fiber, 2 dimension (2D) SiC fiber as well as SiC and W woven fiber were developed. For matrix, W powder, foils with various thicknesses of 0.05 mm and 0.08 mm, and Mo were used in this work. Furthermore, the candidate interfaces, advanced ceramics coatings, such as oxides (ZrO_2, TiO_2 and Er_2O_3), nitrides (ZrN and TiN), carbides (TiC and ZrC), also as diffusion barrier were evaluated by preparing SiC/diffusion barrier/metal joints using hot press in order to prevent the reaction between metals and SiC. All composites were fabricated by hot press. Moreover, the recrystallization behavior of foils used in composites were also investigated. The mechanical property of composite was evaluated by the tensile test at room temperature. Microscopic analysis was carried by scanning electron microscope (SEM).

The results show the composites indeed show the pseudo ductile behavior except composites sintered at higher temperature (1900 °C) due to the strong interface between fiber and matrix caused by the reactions between SiC and W. Therefore, 1700 °C is the recommended sintering temperature to fabricate the SiC fiber reinforced W composites considering the balance between high density to obtain high strength and weak interface to acquire the pseudo ductility. In addition, the best composite in this work is that the

unidirectional SiC fiber reinforced W composite with 0.08 mm foil fabricated at 1700 °C showed the highest strength of 197 MPa and best pseudo-ductility, suggesting that composites with UD fiber show the higher mechanical property compared with that of the composites reinforced by 2D fiber in specified direction because half of fibers do not work during the tensile test in this work. The crack deflection and pull-out fiber can be viewed, supporting the main motivation of this thesis. Moreover, the thermal diffusivity and heat capacity were measured by laser flash analysis (LFA) and differential scanning calorimetry (DSC) respectively to calculate the thermal conductivity. The highest thermal conductivity is composite reinforced by 2D SiC/W fiber of 57.2 W/(m·K) in in-plane direction due to higher content of W, only slightly higher than 1700 °C sintered unidirectional fiber reinforced W composite with 0.08 mm foils of 55.6 W/(m·K). Therefore, the best composite in this work is 1700 °C sintered unidirectional fiber reinforced W composite based on the result of mechanical and thermal properties. In addition, the best diffusion barrier from such candidates is Er_2O_3. But Er_2O_3 as interface in composite needs to be studied further. Based on the results in this work, it can be found that the brittle metals reinforced by ceramic fiber is an effective method to acquire the toughness under the temperature lower than DBTT for metal matrix. Besides, it can be assumed that composite with appropriate interface shows better mechanical property. In addition, it is expected that the pseudo-ductile behavior will be obtained even if metals are brittle caused by neutron irradiation in the reactor.

Chapter 1 Background and Motivation

1.1 Introduction

With the development of society and the advancement of science and technology, people's demand for energy is increasing. In the process of exploring new energy sources, solar energy and nuclear energy are considered to be the most promising new energy sources in the future and have received widespread attention from all over the world. In 1942, the world's first reactor achieved a controlled release of nuclear fission energy, and since then mankind has entered the era of nuclear energy. The nuclear energy has fission energy and fusion energy. However, for fission energy used by mankind, there is a big trouble that is how to deal with the nuclear waste. Moreover, nuclear disasters occurred like Chernobyl and serious safety hazards such as the Fukushima nuclear power plant accident in Japan. Compared with nuclear fission power generation, nuclear fusion power generation has many advantages [1]. The first is that nuclear fusion releases much more energy than nuclear fission. The second is rich in resources and third is low cost. The fourth is safe and reliable. Because once the system is in trouble the nuclear reaction will stop automatically due to the reduce of temperature. Therefore, the accident happened in fission nuclear plant never happened in fusion reaction. Thus, once the controlled nuclear fusion energy can be used, it is the hope of mankind to finally solve the energy problem in the long run, it can be enjoyed by the world for hundreds of millions of years.

The controlled thermonuclear fusion energy is the ideal new energy which can solve mankind's future energy needs and protect the environment. Research about controlled nuclear fusion energy has gone through more than years of hard work and has made great achievements. The easiest way to achieve fusion energy is from the nuclear reactions based on hydrogen isotopes, however the conditions for fusion reactions are still very harsh. At present, there are many kinds of magnetic confinement devices designed, and the most feasible controllable nuclear fusion reaction device is the circulator, called tokamak, in which the charged particles (plasma) will be confined by the Lorentz force from the magnetic fields.

At present, the ITER (International Thermonuclear Experimental Reactor) program is currently one of the world's largest major international scientific projects with the most funding and the most far-reaching impact, also used tokamak. Fig. 1.1 [2] is a schematic diagram of the device structure. However, in the development of new energy, materials are often one of the key factors restricting its success. Although the first wall material does not directly contact the plasma

of the fusion reaction, the environment where the first wall material is located is still very harsh and the working temperature can reach to 1000°C. Meanwhile it is also facing high heat load, plasma sputtering, and high-energy neutron irradiation, especially for the plasma facing materials (PFM). It is expected that the heat flux on the divertor is 10 MW/m^2 in steady state and reach to 20 MW/m^2 in transient state [3], in addition to its good compatibility with plasma, high thermal shock resistance and high thermal conductivity. Besides, it must also consider the connection and compatibility with the heat sink material. Therefore, the existing materials are not fully capable at present, which makes the first-wall or PFM material a key factor restricting the commercialization of nuclear fusion reactors.

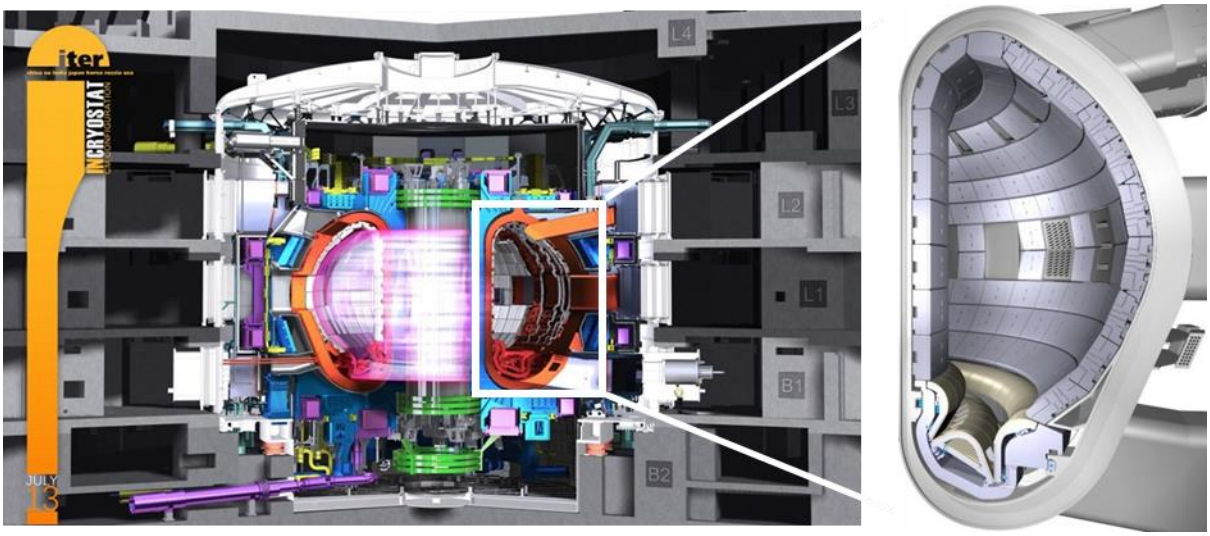

Figure 1.1 The schematic of ITER and plasma facing component [2].

1.2 The choice of plasma facing materials

1.2.1 Service environment of fusion reactor materials

In most fusion devices, hydrogen isotopes are fused into helium by reaction to generate energy, shown as follows,

$$D+T \rightarrow {}^4He\ (3.5MeV) + n\ (14.1\ MeV)$$

The 14.1 MeV neutrons do not interact with the magnetic field, but only move as straight line, usually entering the so-called "first-wall". The He ions with 3.5 MeV will interact with the

magnetic field, so that the energy of He is reduced gradually. When they interact with the divertor, the energy is reduced to 20 eV-100 eV. Because the plasma temperature inside the fusion reactor reaches hundreds of millions of degrees, the working temperature of the first wall material can reach 1000 °C.

1.2.2 Requirements for the plasma facing materials in fusion reactor service environment

Figure 1.2 The challenges of plasma facing materials faced in fusion reactor [4].

As shown in Fig. 1.2 [4], the challenges faced by fusion reactor materials are interrelated. In fusion reactor, the PFMs face the multi-field coupling interaction, that is, high thermal load, high energy neutrons, and high intensity plasma, which will degrade the material properties and affect the life of the first wall material. Therefore, as first wall materials, it is necessary that they can transfer the heat by the high thermal load in time, and resist ion and neutron radiation

effectively, as well as maintain the stability of its material structure. Thus, the first wall materials need to satisfy the following conditions,

1) It is required to have high thermal conductivity, high melting point and good thermal shock resistance. In the operation of a fusion reactor, the first wall material will be bombarded by high-energy particles and encounter high thermal load. It must be able to transfer the heat timely, reduce temperature and stress gradients to improve the stability of the material.

2) It should display good mechanical properties. The good high-temperature tensile strength and creep strength can effectively inhibit the generation of cracks during thermal shock, and materials must be tough or ductile at low temperature to avoid cracks caused by temperature gradients from transient thermal shock.

3) It should exhibit low sputtering rate. In fusion reactor, high-energy ions bombard the first wall material, which will cause sputtering damage on the surface, and the sputtered atoms will affect the progress of the fusion reaction. Because the sputtered atoms entering the plasma will cause bremsstrahlung or braking radiation with the hydrogen isotopes as nuclear fusion fuel, which even stop the fusion reaction in severe situation. Based on this, it is necessary to reduce the impurities entering plasma, especially the high atomic number (Z) impurities.

4) It should show low hydrogen isotopes retention (tritium, deuterium). To continue the thermonuclear reaction in the reactor core, it is necessary to realize the self-proliferation of tritium (T) due to extremely low content of T in nature. If the T retention in the first wall material of the reactor is high, it will affect the nuclear reaction. In addition, the retention of hydrogen isotopes will form hydrogen bubbles inevitably, which will accelerate the embrittlement of the material by irradiation and affect the performance of the material.

5) It should be low activation. In fusion reaction, it does not produce a large amount of radioactive fission products like fission reaction, and the main source of radioactivity is from the neutron activation of the first wall and the cladding material.

In short, the plasma facing materials should be able to maintain the stability and dimensional integrity of the microstructure under the severe radiation, thermal, chemical and stress conditions of the fusion reactor. Therefore, these materials should have good resistance to radiation damage, the surface can withstand high thermal loads, and have excellent mechanical properties

(high strength, high recrystallization temperature, good toughness and low ductile brittle transition temperature).

1.2.3 The selection of plasma facing materials in fusion reactor

Beryllium (Be), carbon (C) or tungsten (W) are considered as the PFMs of ITER [5]. The low-Z material Be exhibits better corrosion resistance during plasma operation, compared with carbon. In addition, it shows very high thermal conductivity (190 W/m/K at RT (room temperature)), which can remove the surface heat flow in time to avoid overheating of the first wall. Therefore, Be can be used as a candidate material for the armor. However, the melting point of Be is only about 1285 °C, which is an extremely serious weakness for PFMs.

Carbon does not melt at high temperatures and can withstand very high thermal loads without any danger of forming a liquid phase. However, the sublimation of carbon at high temperature causes brittle failure of the material, which will increase the erosion of material. On the other hand, its thermo-physical properties are excellent, especially for the CFC (C fiber reinforced C composite). Compared with the traditional fine particle graphite, fiber reinforcement will increase the strength for composite material. Besides, the thermal conductivity of CFC is about 300 W/(m·K) at RT, however the thermal conductivity decreased rapidly after neutron irradiation [6,7]. In addition, C also displays high sputtering etching rate, co-deposition retention with tritium, and neutron irradiation embrittlement.

W is the high Z candidate material in divertor and PFMs for the future Tokamak[8] because W shows low activation, high melting point, high thermal conductivity, low sputtering corrosion and low tritium retention/co-deposition etc. Therefore, ITER has determined a route from Be/C/W to Be/W and finally to full W-PFM, and W is regarded as the most likely to be fully used in reactor design after ITER in the future [9]. However, W displays embrittlement after recrystallization and neutron irradiation. Therefore, other refractory metals like molybdenum (Mo) was also attracted interest as PFM candidate for future rector to broaden the options for fusion development, and recent studies suggest that Mo is a possible alternative to PFM [10–13]. Mo as a kind of high Z refractory metal shows high melting point, low sputtering rate, and high thermal conductivity similar advantages to W. Both W and Mo show body centered cubic structure,

therefore radiation hardening also can be found in Mo materials [14–16]. Therefore, this work is to improve the brittleness of metals even after irradiation.

1.3 The issue of body centered cubic materials for plasma facing materials

1.3.1 The brittleness from structure

In order to improve the toughness of metals, it is very necessary to understand their brittle behavior. The brittleness of W material is the behavior of fracture without obvious yield or plastic deformation under the external force, suggesting that W material exhibit high strength and hardly plastic deformation. In other words, the lattice resistance that W needs to overcome for plastic deformation is relatively large, or the dislocation mobility in the material is limited. For the body-centered cubic (BCC) structure metal, the plastic deformation mainly depends on 1/2<111> screw dislocations [17,18], and the dislocations incline to slip on the (110) crystal plane. In the {110}<111> slip system of the BCC structure metals, the slip direction on the slip surface, namely the <111> direction, has only 1 or 2 directions, implying the dislocation mobility is limited, so they are more likely to exhibit brittle behavior compared to FCC (face-centered cubic) structure metals [19]. Cui et al [20] used discrete dislocation dynamics simulations and found that the energy barrier needed to overcome for 1/2<111> screw dislocation nucleation and movement is relatively large. In addition, the yield stress of W plastic deformation strongly depends on the temperature, which is the yield stress decreases significantly when the temperature rises. Giannattasio et al [21] simulated the crack tip dislocation behavior of W materials and found that increasing temperature is beneficial to dislocation nucleation.

It is worth noting that the researchers [22,23] found that the single crystal W does not have brittleness at RT through experiments, and its DBTT is only 77 K [23], even as low as 20 K [22]. Compared with single crystal W, W materials used in engineering applications are generally polycrystalline materials. Therefore, W materials exhibit brittle behavior at RT, which is related not only to the lattice strcture of W, but also to the presence of grain boundaries in the material. The influence of the grain boundary mainly has three aspects [24], 1) low grain boundary strength; 2) incompatibility of deformation between grains; 3) grain boundary limits the mobility of dislocations. Due to the low grain boundary strength, the W material at RT mainly shows the

intergranular and brittle fracture, caused by the impurity elements (C, N, O, P, S, etc.) segregated at the grain boundaries [25–27]. The incompatibility of deformation between grains at low temperature is very important, mainly because the mobility of screw dislocations depends on the number of movable slip systems of dislocations. For polycrystalline materials, if the number of movable slip dislocations are less than 5, it is difficult to continue uniform plastic deformation, so that the material exhibits low toughness behavior. Cheng et al [28] simulated the interaction between dislocations and grain boundaries in W, and the results show that dislocations are more likely to transmit strain and deform through small-angle grain boundaries. Generally, the DBTT of W materials is from 150°C to 400 °C, implying that W is usually brittle under water-cooling conditions. For brittle materials, cracking is usually sudden and catastrophic without obvious damage or warning. PFMs and structural parts must avoid cracks like this. Therefore, the high ductility at room temperature and above is very useful for the application of W. The high temperature in fusion reactor will change the microstructure of W through recovery, recrystallization then grain growth. Due to the internal stress in the grain boundary and the increase of grain size, the mechanical properties degraded, and the DBTT enhanced. Fig. 1.3 shows the recrystallization curve of W annealed at elevated temperatures for 1 h [4].

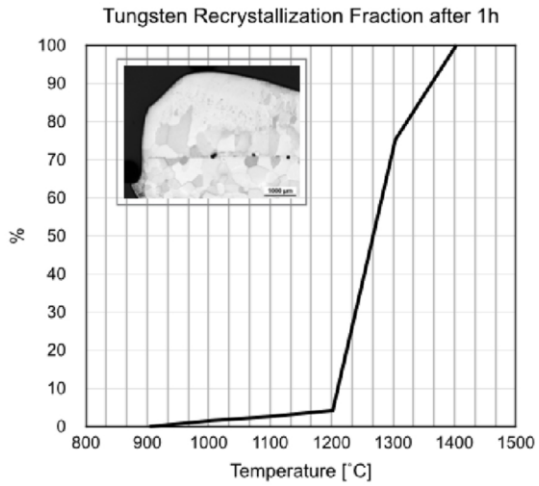

Figure 1.3 Recrystallization behavior of tungsten annealed at a given temperature for 1 h [4].

1.3.2 The embrittlement from irradiation

Irradiation embrittlement (or radiation hardening) can be found in almost any materials, including W and Mo. The lattice atoms in materials will deviate from their original position and form a large number of primary knock-on atoms (PKA) after the impact of ions or neutrons produced by nuclear reactions. And these generated PKAs will form complex defects through a further cascade collision process, such as interstitials, vacancies, dislocation loops, stacking fault tetrahedrons and voids, etc. The illustration of generation of PKAs and cascade collision is shown in Fig. 1.4 [7]. In addition, long range replacement collisions, called dynamic crowdion, exist during irradiation. When the nuclear material undergoes plastic deformation under external loads, the movement of its internal dislocations will be affected by these large amounts of radiation defects, which will greatly change its mechanical properties, such as radiation hardening, and radiation embrittlement etc. In the future fusion reactor, W will suffer the greater thermal load, and be exposed to high-energy neutrons and low-energy ions at the same time. Meanwhile, intergranular cracking was caused by recrystallization and radiation embrittlement. Besides, hydrogen isotopes retain highly for the moment. Although the solubility of hydrogen isotopes in W is extremely low, a large number of lattice defects, generated by the irradiation of energy particles, act as strong trapping sites for hydrogen isotopes and increase their retention rate significantly. Inhibiting the retention of hydrogen isotopes requires reducing the accumulation of lattice defects caused by radiation, which will also reduce the embrittlement of radiation.

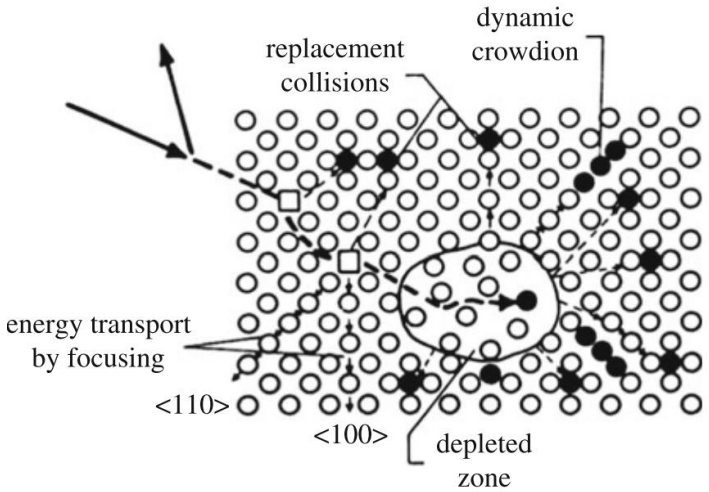

Figure 1.4 Schematic illustration of generation of PKAs and cascade collisions [29].

1.4 Methods to improve the brittleness of refractory metals

The brittle behavior of the materials is not only dependent on its lattice type and the bonding force between lattice atoms (atomic bonds), but also related to the surface energy for cracking [30,31]. The former is the lattice property of the material, which is related to the dislocation nucleation and dislocation mobility when the material undergoes plastic deformation, and the latter is related to the work-of-fracture of material. Therefore, improving the brittle behavior of W can be considered from the increase of the plastic deformation ability of the material, and the material's fracture absorption work. According to the Griffith crack theory [32], under the external force, the cracks begin to grow steadily when the stored elastic potential energy of the materials is not less than the new surface energy generated by the crack propagation, which suggests that the resistance to brittle cracking of materials can be relieved by changing the new surface morphology (increasing surface energy) formed by the fracture. In addition, toughness is the ability of materials to resist the fracture in fracture mechanics. Therefore, the method to improve the toughness of W should also be considered from the crack initiation and crack propagation.

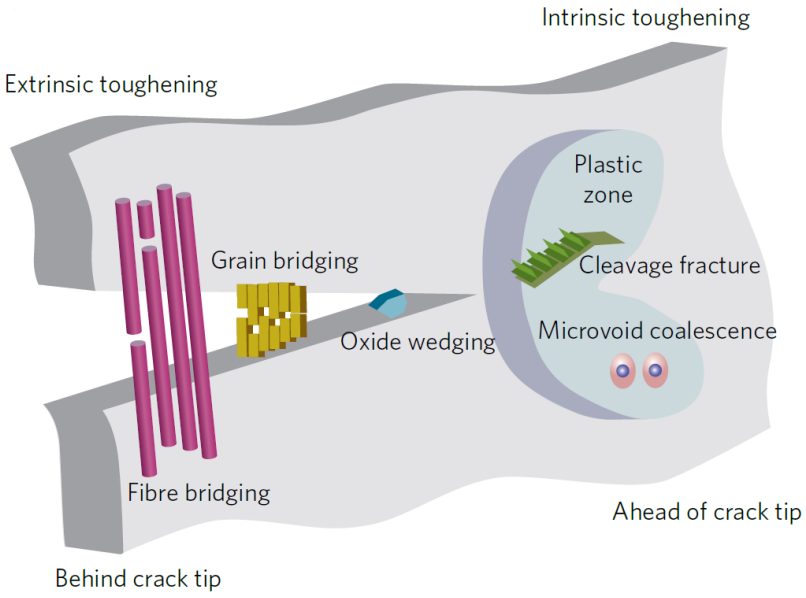

Figure 1.5 Schematic illustration showing how strength and fracture behavior can be considered in terms of intrinsic (plasticity) versus extrinsic (shielding) toughening mechanisms associated with crack extension [33].

Two toughening mechanisms are proposed by Ritchie, and the schematic diagram is shown in Fig. 1.5 [33], which can be divided into internal toughening and external toughening. Internal toughening is always related to improving the plasticity of the material, which acts on the front of the crack tip and can effectively resist crack formation and propagation. Therefore, the internal toughening mechanism is generally to increase the mobility of dislocations to produce a plastic zone at the front of the crack tip (see Fig. 1.5). Then, the movement of dislocations causes dislocations to block up or cause interface separation, leading to cleavage fracture or micro pore aggregation fracture. For the external toughening mechanism, the inherent fracture resistance of materials was not changed, and it mainly acts behind the crack tip, which can alleviate and hinder the crack propagation by changing the microstructure characteristics of the fracture surface. In composite materials, the external toughening mechanism can generally be achieved by adding fibers, flake layers, second phase particles or tough phases to provide bridging traction on the cracks. In essence, external toughening is to improve the fracture toughness of the material by increasing the energy required to form a new surface by the fracture of the material. Generally speaking, the internal toughening mechanism is for plastic materials to resist fracture, and the external toughening mechanism is for brittle materials on the contrary [33,34]. For brittle W materials at RT, two toughening mechanisms, internal toughening and external toughening, can be used to improve the toughness of W to satisfy practical engineering applications. And, a lot of research works have been carried out on high-performance W-based materials, including alloying [35-37,41-42,45-49], dispersion [50-66], machining technology [71-87] as well as fiber reinforced composites [88-93].

1.4.1 Alloying

The improvement of metals' toughness by adding alloying elements mainly focused on two aspects. One is to add alloying elements that can form a solid solution with W, and to change part of the W-W atomic bonds in the material, which is expected to improve the toughness of W. The other is to add metal elements that cannot or are slightly solid-soluble in W used as the matrix phase. The most typical materials corresponding to these two situations are W-Re alloy and W heavy alloy, respectively.

1.4.1.1 Solid solution strengthened W

Solid solution strengthening refers to the phenomenon that alloying elements are dissolved in the base metal to increase the strength of the alloy. This is because the solute atoms will cause the matrix lattice distortion, thereby hindering the dislocation slip to improve the yield strength of the alloy. We can add other solid solution elements to W to achieve high strength W-alloy through this solid solution strengthening principle. Re element has been widely added to BCC structural metals such as W, Mo and Cr to improve toughness [35]. For W, adding Re can alter the symmetry properties of the 1/2<111> screw dislocation core to increase the number of slip surfaces, and on the other hand, it can reduce the Peierls force of plastic deformation, resulting the improvement of the mobility of dislocation [36], suggesting that Re as a toughening element to improve the toughness of W materials belongs to the internal toughening mechanism. Besides, the grain boundary bonding force can also be improved by adding Re [37]. However, for nuclear material applications, the addition of Re must be restricted to satisfy the lower activation requirements [38], and to avoid the formation of brittle phases of irradiation-induced precipitation WRe (σ phase) and WRe_3 (χ phase) [39,40]. Same phenomenon can also be found in Mo-Re alloys [16]. The degree of radiation hardening is proportional to the content of Re, and the DBTT of Mo-41Re is 874 K after irradiation. Ta, V and Ti was also added to W to strengthen W by alloying, however, alloying with Ta and V does not improve the Charpy energy of W [41]. In addition, with the increase of Ta content, the fracture toughness of W-Ta alloy decreases [41,42]. Recent research on W-Ti alloy has not brought promising results, in which the alloys still show brittle at RT [43,44], suggesting that the other elements do not change the crystal structure, or vary the crystal structure in a different way from Re.

1.4.2.2 Heavy alloy

W heavy alloy is composed of W phase with high strength and high melting point, and matrix phase with high toughness and low melting point. The matrix phase is generally metal elements with FCC structure, such as Ni, Fe, Cu, Mn, Co, etc [45–49]. The low melting point of matrix phase enables W heavy alloys achieve high densification by liquid phase sintering. The ideal W heavy alloy has both the high strength of W and the good toughness of the matrix material, so it can exhibit good mechanical properties, which depends on the interfacial strength of matrix

phase and W. Senthilnathan et al [46] added an appropriate amount of Co to W-Ni-Fe alloy, and found that the addition of Co can not only increase the strength of the matrix phase, but also improve the of the interfacial strength. Adding 1 wt% Co can increase the yield strength of W-Ni-Fe from 686 MPa to 1300 MPa, and its fracture strength can reach to 1508 MPa. Moreover, the main fracture mode also changes from intergranular fracture to transgranular fracture. The main factors affect the interfacial strength between W and the added matrix phases are, 1) Intermetallic compounds formed between W and matrix phases weaken the interface; 2) Cracks and nucleation of holes are prone to occur at the W-W interface [49]; 3) Impurity elements (such as S, P, O, etc.) segregate at the interface to weaken the interface. Therefore, the rare earth elements, such as La [45] and Y [48], were added to purify the grain boundaries and increase the interface strength, so as to achieve the purpose of improving the mechanical properties of W heavy alloys. Fig. 1.6 [48] displays the tensile test results of 93W–0.03Y alloy, prepared by powder metallurgy, at 25 °C to 1000 °C. It is easy to notice the plastic deformation in W-0.03Y heavy alloy tested at RT, indicating that the plastic deformation of the W heavy alloy during stretching is mainly dominated by the plastic deformation of the matrix phase. Besides, the work hardening capacity declines noticeably with heighten the measurement temperature.

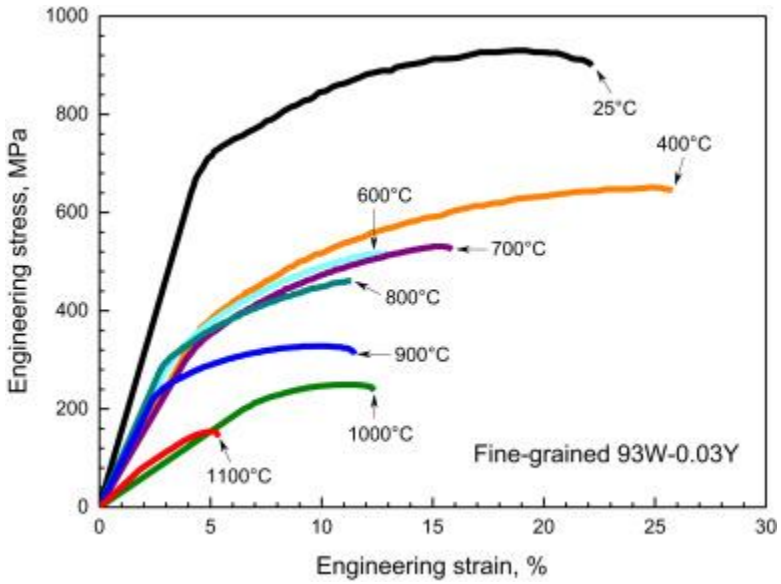

Figure 1.6 Engineering stress–strain curves of fine grain W-4.9Ni-2.1Fe-0.03Y [48].

Fig. 1.7 [48] is the SEM image of the fracture morphology of W-0.03Y at different temperatures. It can be seen that the fracture modes of the W alloy after being stretched at RT are mainly the

transcrystalline cleavage fracture in W and the ductile fracture in the matrix phase. As the temperature rises, obvious slip lines can be found on the cross-crystalline fracture of W, implying that there are obvious signs of dislocation movement in the W particles, which shows that the increase of temperature can improve the dislocation mobility effectively (see Fig. 1.7 b)). The main fracture mode of W heavy alloy changes to intergranular fracture when the tested T is 1100 °C (see Fig. 1.7 d)). In addition, the fracture morphology showed obvious peeling from the W/W interface and the W/matrix interface. Combined with the tensile properties of W heavy alloys, it can be seen that the material has good mechanical properties when the fracture mode is transcrystalline cleavage fracture in W and ductile fracture in the added matrix phase. This shows that the toughening of W heavy alloys is mainly through the plastic deformation of the matrix phase to achieve the toughening effect. This kind of mechanism that does not change the plastic deformation ability of W to achieve toughening is an external toughening mechanism.

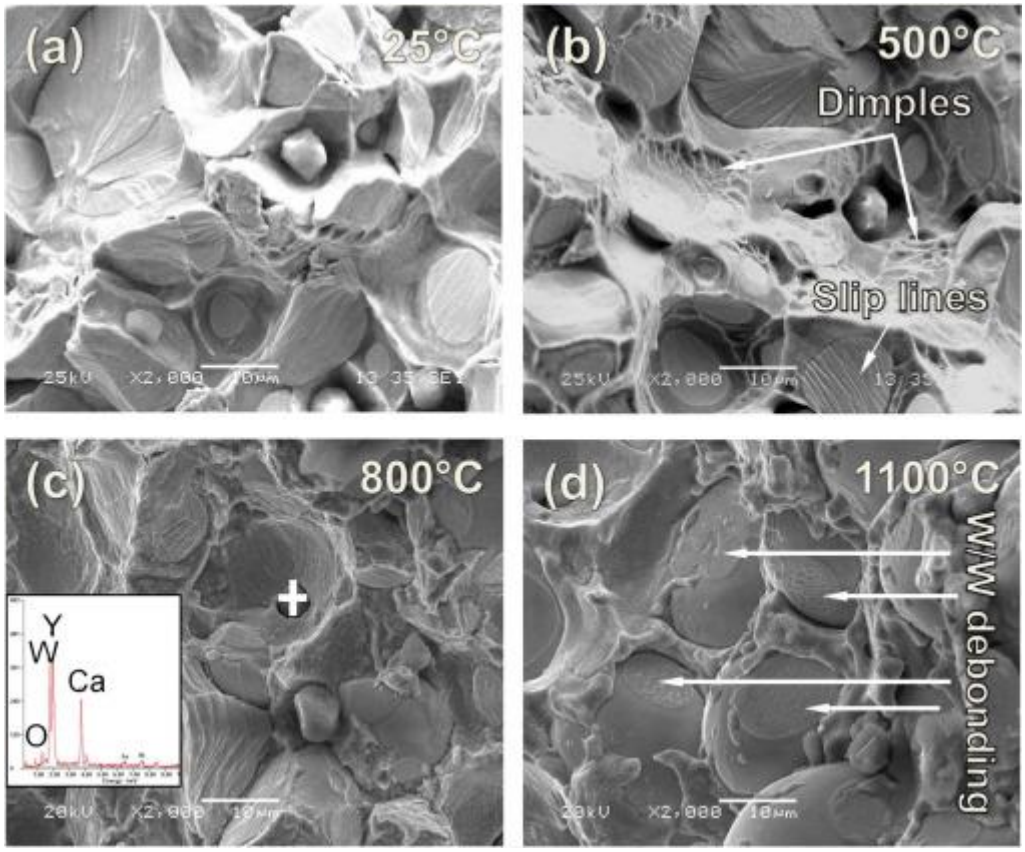

Figure 1.7 SEM fracture morphologies of 93W-4.9Ni-2.1Fe-0.03Y alloy after tensile test [48].

1.4.2 Second phase dispersion

Impurity elements, such as nitrogen, oxygen and phosphorus as well as other elements, segregate at the grain boundaries (GB) of W easily, forming an embrittlement film on the GBs. This films bring about lowering GB strength, leading to intergranular brittle fracture, and increasing the initial DBTT and low temperature brittleness significantly. The impurity elements at GBs can be reduced by adding active elements such as Y, La, Ti, Zr, etc. or by absorbing free impurities N, O, P at the GBs to form the stable compounds. In addition, the formed compounds can pin dislocations and grain boundaries, then hinder the movement of dislocations and grain boundaries, thereby improving the strength of the material, refining the grains and stabilizing the crystal structure.

Previous studies show that W-2wt%Y_2O_3 (ODS-W) composites, prepared by powder metallurgy, has ductility properties from 400 °C by 3 point bending test [50], which is no improvement compared with pure W. Huang et al [51] also reported the DBTT of pure W is about 400 °C to 500 °C. Another important additive that has attracted the attention of many researchers is La_2O_3 [52,53]. Adding 1% La_2O_3 to W can improve its cutting performance and recrystallization temperature [52,54]. However, W-10%La_2O_3 exhibit higher DBTT compared with pure W although ODS-W shows higher yield strength, indicating that ductility reduced in La_2O_3 dispersed W [55].

There is another drawback in ODS-W materials. Oxide particles cannot maintain thermodynamic stability because these reinforced particles are easily coarsened at high temperature. For example, W-Y_2O_3 composite material sintered at higher temperature lead to the loss of the dispersion strengthening effect due to the coarsening of the high-temperature sintered oxide particles, thus failing to improve the mechanical properties of tungsten [56].

Carbides also attract attention as candidate additives for the preparation of dispersion-reinforced composites. Different carbides have been studied, including TiC [57–59], TaC [60], WC [61–63], ZrC [64], HfC [65] and SiC [66] etc. Carbide dispersion-strengthened W-based alloys can not only refine grains and improve mechanical properties, but also the melting point is higher compared with these oxides Y_2O_3 (2410 °C), La_2O_3 (2217 °C), while for the carbides the melting point of carbides is about 3540 °C for ZrC, 3140 °C for TiC and 3900 °C for HfC

respectively. And generally speaking, materials with high melting point have high thermodynamic stability and low vapor pressure.

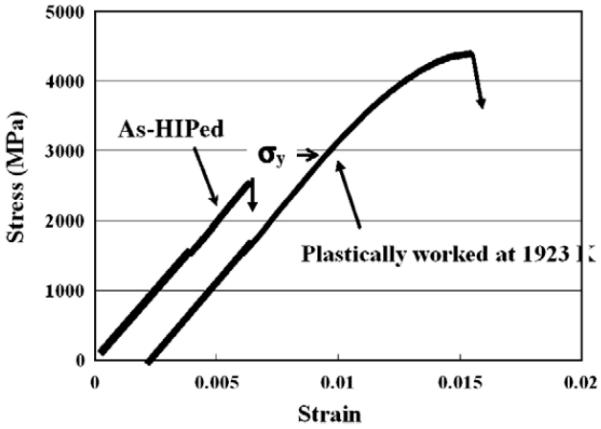

Figure 1.8 The 3 pointing bending stress strain curves for W–1.1TiC before and after compression forming at 1923 K [59].

Kurishita et al fabricated W with different ratio of TiC after hot isostatic pressing. They found that adding TiC can refine the W grains, reduce DBTT, and improve recrystallization temperature and mechanical properties [57–59]. And atmosphere during sintering has also an impact on the mechanical property. The strength of W-TiC alloy sintered in H_2 is higher than that of material sintered in Ar [57]. Besides, W-1.1wt%TiC after compression forming show the highest strength of 4.4 GPa and appreciable RT-ductility (see Fig. 1.8) [59]. In addition, W-0.3TiC, irradiated at 550 °C by He ions, displays the 10 times irradiation resistance compared with commercial pure W [58]. W-0.5wt%ZrC material were prepared by powder metallurgy. And the DBTT of W-ZrC is about 50-80 °C, which is much lower than that of pure W [64]. The ZrC particles are located in the grain boundary or phase boundary, reducing the concentration of O at the GBs. The coarsening and concentration of the dispersion at the GBs in the ODS-W alloy can be inhibited, because of the higher melting point and thermal stability of ZrC.

Due to the high thermal stability of carbides, carbides can not only refine the grains, but also stabilize the crystal structure and inhibit the growth of grains at high temperatures, which makes the addition of carbides improve the performance of tungsten-based materials as well as stabilize the microstructure of tungsten-based materials at high temperatures to improve the thermal stability of W.

However, for adding 2nd phases (oxides or carbides) dispersed tungsten materials to strength W, there is a problem to improve the toughness. Like the author descripted in 1.4.1 '*because the solute atoms will cause the matrix lattice distortion, thereby hindering the dislocation slip to improve the yield strength of the alloy*' and '*In addition, the formed compounds can pin dislocations and grain boundaries, then hinder the movement of dislocations and grain boundaries, thereby improving the strength of the material, refining the grains and stabilizing the crystal structure.*', the principle is impediment the movement of dislocations, which benefits the strength. And 2nd located in the grain boundary can suppress the grain growth of base material. Both conditions have the advantage in strength, but damage the ductility or fracture toughness. In addition, all investigation on 2nd phase dispersed W led to improved creep or strength, to higher recrystallization behaviour, and to better machining based on Hall-Petch relation. On the other hand, a clear reduction of tensile elongation could be recognized in most works[55], which match the mutually exclusive relationship between strength and fracture. In nano-scale W, it should show higher ductility due to grain boundary sliding. However, it is difficult to obtain only by adding second phase particles.

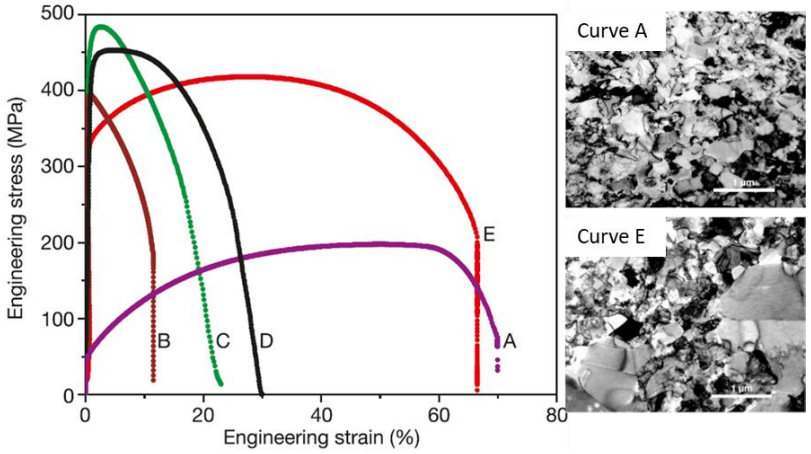

Figure 1.9 The tensile test and microstructure of Cu [67]. Curve A, annealed, coarse-grained Cu; B, room temperature rolling to 95% cold work (CW); C, liquid-nitrogen-temperature rolling to 93% CW; D, 93% CW + 180 °C, 3 min.; and E, 93% CW + 200 °C, 3 min.

Wang et al [67] prepared Cu with uneven grain size, the tensile test results and microstructure is shown in Fig. 1.9 [67]. The specimen with uniform nano-size grain show high strength (curve D), however for specimen with abnormal grain (curve E), it shows high strength

with high ductility. Therefore, the increase in ductility provided by grain boundary sliding in small grains is either insufficient to compensate for the loss of dislocation controlled ductility [67,68]. So material with dual-size grains might display high strength and high ductility, in which small grain is responsible for strength, and large grain is responsible for ductility.

1.4.3 Machining deformation technology

The influence of processing deformation on W material is mainly in 4 aspects [24,69]: 1) Refine the grain size; 2) Change the grain orientation (texture); 3) Change the crystal morphology; 4) Increase the dislocation density. These effects may be beneficial to the toughness after processing and deformation. After W is processed and deformed, the grain refinement effect is very obvious, and the large plastic deformation can refine the grains to submicron or even nanoscale (below 100 nm) [70,71].

In addition, the textured W is related to its DBTT. Fig. 1.10 [72] shows the fracture toughness results of different crack systems of single W crystal with temperature changes. It can be found that the DBTT of W with the cracks {100}<001> and {100}<011> are about 470 and 370 K, respectively, while the DBTTs of W with the cracks {110}<001> and {110}<011> are about 430 K and 370 K, respectively, which shows that W grains with different orientations have different fracture toughness and DBTT. The processed polycrystalline W displays texture orientation, and its texture type is mainly related to the processing technology. For the deformation of the BCC structure W, forging, extrusion, and wire drawing will cause a strong <110>-type texture, on the contrary, rolling deformation will produce a {111}-type texture and a <110>-type texture. Different types of textures have different Schmidt factors of deformation, so the texture orientation grains which is beneficial to toughness can be increased through processing deformation to improve the toughness of W.

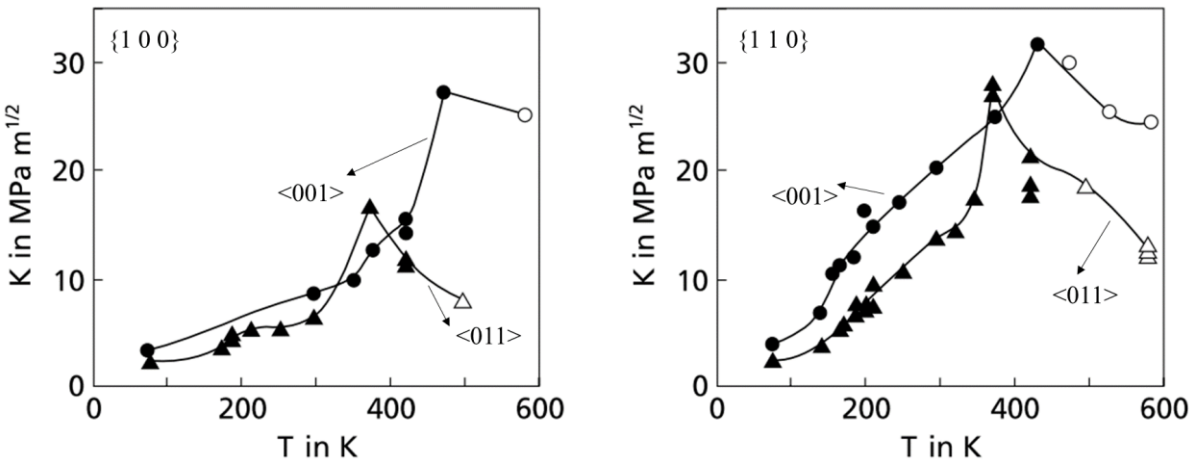

Figure 1.10 Fracture toughness of W with single crystals for the four low index crack systems at different temperature [72].

The crystal morphology of W after deformation may also affect its toughness and brittle behavior. The three-point bending test were carried out on the W deformed by rolling along different directions. It was found that the fracture perpendicular to the rolling direction showed fibrous morphology and mainly transcrystalline cleavage fracture, while the fractures in other directions were mostly intergranular fracture [73,74]. Rupp et al [73] found that, from RT to 600 °C, the fracture toughness in perpendicular to the rolling direction was significantly higher than the fracture toughness in other directions, which is not only related to the texture orientation, but should also be related to the change of grain morphology caused by deformation. In addition, a large number of dislocations are introduced during deformation, meaning that the number of movable screw dislocations and dislocation mobility increases, so the deformed W showed better plasticity and toughness [75].

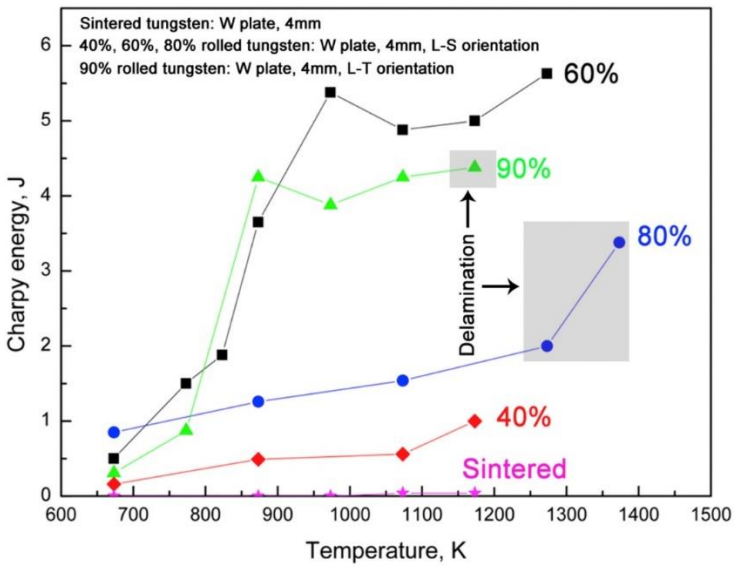

Figure 1.11 Charpy impact performance of the sintered and rolled tungsten [76].

At present, the more widely used processes for processing and deforming W materials include rolling [76] , forging [77,78], and a combination of the two processes [79,80]. There are also large plastic deformation processes such as high-pressure torsion [81] and equal channel angular extrusion [82] to process W. Zhang et al. [76] performed Charpy impact experiments on pure W with different rolling deformation ratios at different temperatures, and the corresponding fracture toughness results are shown in Fig. 1.11 [76]. It can be seen that under the experimental test conditions, pure W in the sintered state is brittle, and the toughness of W after rolling deformation is obviously improved; the fracture toughness of pure W with different deformation ratios is different, which is mainly due to the different deformation ratios. It is worth noting that when pure W with a deformation ratio of 80% and 90% is subjected to Charpy impact at a higher temperature, the fracture surface shows a layered morphology. Rieth et al. [83] performed Charpy impact experiments on W materials subjected to rolling deformation at different temperatures and also found this layered tear-like fracture morphology. This fracture morphology means that high energy is required to form a new surface when the material fractures, thereby improving the toughness of the W material by reducing the tendency of the material to crack. This method of improving the toughness of W materials can be called layered toughening, which belongs to the energy release mechanism [84]. Therefore, many studies [85–87] have performed multiple rolling deformations on W materials to obtain a layered structure W material with strong texture in order to improve the toughness of the material.

1.4.4 Fiber reinforced composites

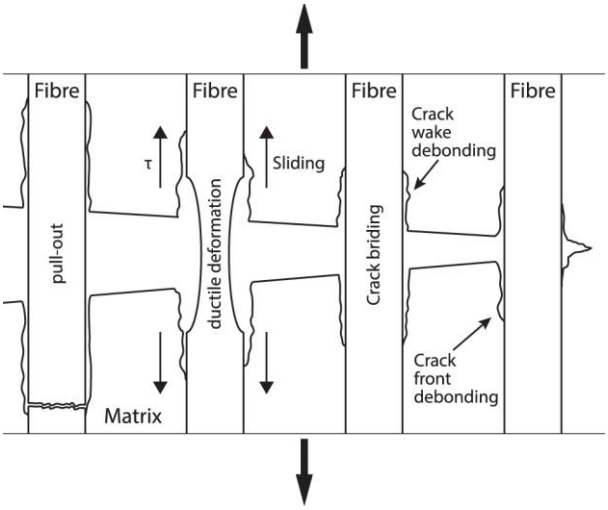

Figure 1.12 The mechanism to toughen brittle material [88].

W fiber toughened tungsten matrix composites are also considered to be one of the effective ways to improve W toughness [89–91]. W-fiber-toughened tungsten-based composites are mainly reflected in the crack propagation stage, so they belong to the external toughening mechanism. The toughening effect is mainly determined by two factors: W fiber and the interface between W fiber and W matrix. Fig. 1.12 [88] is a schematic diagram of the toughening mechanism of W fiber toughened brittle matrix composites. Since the added W fiber has good plastic deformation ability [92], under the action of external load, energy is mainly consumed in three ways: fiber deformation, fiber pull-out and crack bridging to improve the toughness of W material. This means that W fiber toughened tungsten-based composites also belong to the energy release mechanism. In addition, improving the toughness of W materials can also increase the area of the material fractured to form a new surface and the energy required. Therefore, the interface between W fiber and W matrix should be designed reasonably. The purpose of adding W fiber is that after the W material cracks, the material can continue to work and not fail. At present, researchers mainly prepare fiber-toughened tungsten-based composites by preparing a layer matrix with W long fibers [88,89]. Due to the high technological requirements for weaving W long fibers, Mao et al. [93] used powder metallurgy to successfully prepare W short fiber reinforced tungsten matrix composites. In addition, the interface between W fiber and W matrix is weakened by preparing

Er_2O_3 [94], Mo and Y_2O_3 [93] interlayers to weaken the interface, so that cracks can expand along the interface to generate a large number of new surfaces to improve the toughness of W.

1.5 The reasons to select SiC fiber

Considering that the fiber reinforced ceramic matrix composites show ductility while matrix still is brittle, fiber reinforcement method was used in this work. In addition, ceramic SiC fiber was selected as reinforcement to strengthen W and Mo. The reasons for selection SiC fiber are as follows.

1) SiC fiber-reinforced SiC-based ceramic composites (SiCf/SiC) have been studied in nuclear reactors for several decades due to its good thermophysical properties, such as thermal stability, oxidation resistance, creep resistance and high strength at high temperature [95].

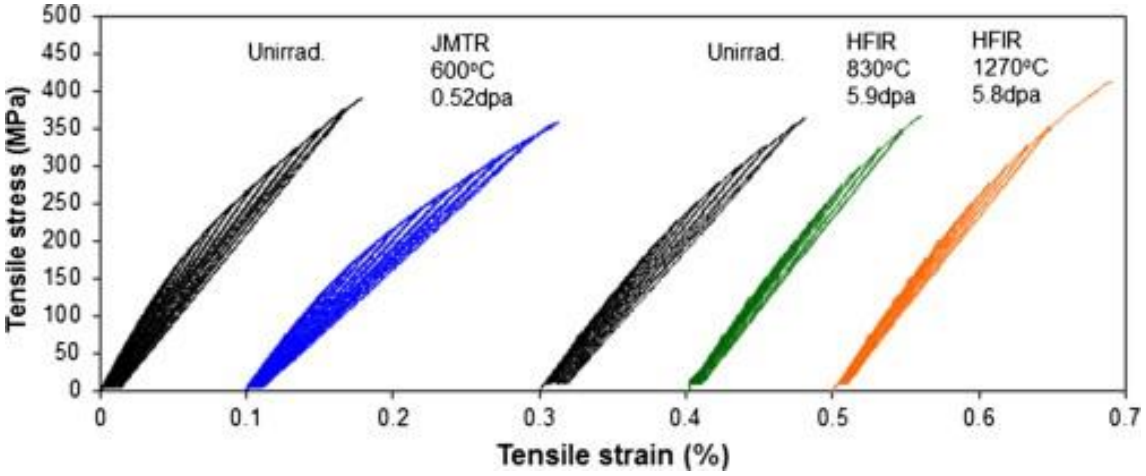

Figure 1.13 Tensile stress–strain behaviors for the unirradiated and irradiated NITE-SiC/SiC composites [96].

2) SiC materials also exhibit excellent mechanical properties in a neutron irradiation environment (see Fig. 1.13) [96,97]. The fracture strength and pseudo ductile behavior did not change much after neutron irradiation. In addition, it was found that the pure SiC and SiCf/SiC composites have high strength and good dimensional stability at irradiation doses up to 70 dpa in the temperature range of 500 to 1,000 °C [98].
3) Metals and SiC have very close thermal expansion coefficients(CTE). The CTE of W and Mo is 4.4×10^{-6} and 5.2×10^{-6} /K respectively. Besides, the ceramic fibers are very close to metals with 4.5×10^{-6} /K. In addition, the swelling of SiC is lower than 1% at 800 °C to 1300 °C in

the operating temperature window of W by neutron irradiation [96, 98], so it is considered that the stress generated at the interface is minor.

4) Besides, both Si and C are light elements with good compatibility to plasma.

1.6 Motivation and outline in this work

W and Mo are the candidates for the plasma-facing components of nuclear fusion devices due to their high melting point, high thermal conductivity and high resistance to sputtering yield. Severe radiation hardening embrittlement due to irradiation-produced defects occurred even with a low-level exposure for both metals. Therefore, fiber reinforced metal composites were developed like ceramic composites in this work. High strength SiC fiber was used as reinforcement in this work, because SiC materials also exhibit excellent mechanical properties in a neutron irradiation environment [95]. Therefore, the objective of this thesis is to investigate whether the SiC-based fiber strengthened brittle metals (W, Mo) composites show pseudo ductility at room temperature, like fiber reinforcement ceramic composite from the toughening mechanism of long fiber reinforced matrix, and optimize the strength and thermal property of fabricated composites.

Long fiber reinforced composites include fiber, matrix and interface. In this work, composite with various fiber and matrix with or without foil were fabricated by hot press at different sintering temperature. Mechanical property especially tensile test was examined at room temperature and high temperature at 1000 °C. In addition, fracture behavior and microstructure after tensile test were also investigated. Effects of the sintering temperature, the type of fibers and matrixes on mechanical property and thermal property were studied. In addition, the recrystallization behavior of foils used in this work was also analyzed. Moreover, suitable diffusion barrier between SiC and metal was evaluated from microstructure. The outline of whole work is revealed in Fig. 1.4. Chapter 2 describes the details about the fabrication of fiber reinforced composite, and the specimen for evaluating the diffusion barrier, as well as the property analysis methods. The effect of sintering temperature, fiber types, and different matrixes with or without foil on the microstructure, chemical composition, the fracture behavior, and the mechanical property and thermal property of fiber reinforced composites are presented in Chapters 3, 4 and 5, respectively. Besides, recrystallization development at high temperature can be found in this Chapter 4. Chapter 6 discusses the possible diffusion barrier based on the microstructure and

element analysis. In addition, the mechanical property and microstructure of composite with the workable diffusion barrier were also discussed. Chapter 7 summarizes and concludes the full text.

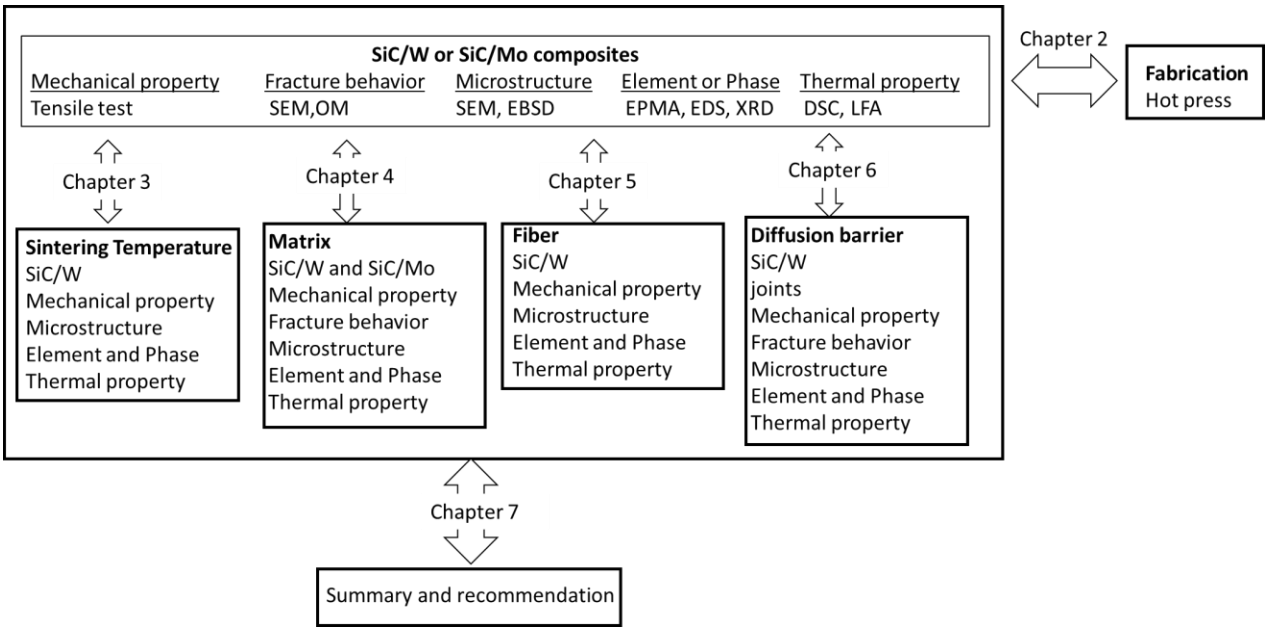

Figure 1.14 The schematic flow of this work.

References

[1] R. Toschi, Nuclear fusion, an energy source, Fusion Eng. Des. 36 (1997) 1–8. https://doi.org/10.1016/S0920-3796(97)00007-0.

[2] HOW DOES IT WORK?, (n.d.). https://www.iter.org/mach.

[3] DIVERTOR, (n.d.). https://www.iter.org/mach/divertor.

[4] J.W. Coenen, S. Antusch, M. Aumann, W. Biel, J. Du, J. Engels, S. Heuer, A. Houben, T. Hoeschen, B. Jasper, F. Koch, J. Linke, A. Litnovsky, Y. Mao, R. Neu, G. Pintsuk, J. Riesch, M. Rasinski, J. Reiser, M. Rieth, A. Terra, B. Unterberg, T. Weber, T. Wegener, J.H. You, C. Linsmeier, Materials for DEMO and reactor applications - Boundary conditions and new concepts, Phys. Scr. 2016 (2016). https://doi.org/10.1088/0031-8949/2016/T167/014002.

[5] J.M. Linke, T. Hirai, M. Rödig, L.A. Singheiser, Performance of Plasma-Facing Materials Under Intense Thermal Loads in Tokamaks and Stellarators, Http://Dx.Doi.Org/10.13182/FST04-A550. 46 (2017) 142–151. https://doi.org/10.13182/FST04-A550.

[6] L.L. Snead, Y. Katoh, W.E. Windes, R.J. Shinavski, T.D. Burchell, Ceramic composites for near term reactor application, 2008 Proc. 4th Int. Top. Meet. High Temp. React. Technol. HTR 2008. 2 (2009) 1–10. https://doi.org/10.1115/htr2008-58050.

[7] J.P. Bonal, C.H. Wu, Neutron irradiation effects on the thermal conductivity and dimensional stability of carbon fiber composites at divertor conditions, J. Nucl. Mater. 228 (1996) 155–161. https://doi.org/10.1016/S0022-3115(95)00247-2.

[8] M. Rieth, S.L. Dudarev, S.M. Gonzalez De Vicente, J. Aktaa, T. Ahlgren, S. Antusch, D.E.J. Armstrong, M. Balden, N. Baluc, M.F. Barthe, W.W. Basuki, M. Battabyal, C.S. Becquart, D. Blagoeva, H. Boldyryeva, J. Brinkmann, M. Celino, L. Ciupinski, J.B. Correia, A. De Backer, C. Domain, E. Gaganidze, C. García-Rosales, J. Gibson, M.R. Gilbert, S. Giusepponi, B. Gludovatz, H. Greuner, K. Heinola, T. Höschen, A. Hoffmann, N. Holstein, F. Koch, W. Krauss, H. Li, S. Lindig, J. Linke, C. Linsmeier, P. López-Ruiz, H. Maier, J. Matejicek, T.P. Mishra, M. Muhammed, A. Muñoz, M. Muzyk, K. Nordlund, D. Nguyen-Manh, J. Opschoor, N. Ordás, T. Palacios, G. Pintsuk, R. Pippan, J. Reiser, J. Riesch, S.G. Roberts, L. Romaner, M. Rosiński, M. Sanchez, W. Schulmeyer, H. Traxler, A. Ureña, J.G. Van Der Laan, L. Veleva, S. Wahlberg, M. Walter, T. Weber, T. Weitkamp, S. Wurster, M.A. Yar, J.H. You, A. Zivelonghi, Recent progress in research on tungsten materials for nuclear fusion applications in Europe, J. Nucl. Mater. 432 (2013) 482–500. https://doi.org/10.1016/j.jnucmat.2012.08.018.

[9] O. Gruber, A.C.C. Sips, R. Dux, T. Eich, J.C. Fuchs, A. Herrmann, A. Kallenbach, C.F. Maggi, R. Neu, T. Pütterich, J. Schweinzer, J. Stober, Compatibility of ITER scenarios with full tungsten wall in ASDEX Upgrade, Nucl. Fusion. 49 (2009). https://doi.org/10.1088/0029-5515/49/11/115014.

[10] G. De Temmerman, K. Bystrov, J.J. Zielinski, M. Balden, G. Matern, C. Arnas, L. Marot, Nanostructuring of molybdenum and tungsten surfaces by low-energy helium ions, J. Vac.

Sci. Technol. A Vacuum, Surfaces, Film. 30 (2012) 041306. https://doi.org/10.1116/1.4731196.

[11] J.N. Brooks, L. El-guebaly, A. Hassanein, T. Sizyuk, IAEA Fusion Energy Conference 2014 Plasma Facing Material Alternatives to Tungsten 1, (2017) 3–10.

[12] J.K. Tripathi, T.J. Novakowski, G. Joseph, J. Linke, A. Hassanein, Temperature dependent surface modification of molybdenum due to low energy He+ ion irradiation, J. Nucl. Mater. 464 (2015) 97–106. https://doi.org/10.1016/J.JNUCMAT.2015.04.022.

[13] G. Sinclair, J.K. Tripathi, P.K. Diwakar, A. Hassanein, Melt layer erosion during ELM-like heat loading on molybdenum as an alternative plasma-facing material, Sci. Rep. 7 (2017) 1–10. https://doi.org/10.1038/s41598-017-12418-z.

[14] B. V. Cockeram, R.W. Smith, L.L. Snead, Tensile properties and fracture mode of a wrought ODS molybdenum sheet following fast neutron irradiation at temperatures ranging from 300 °C to 1000 °C, J. Nucl. Mater. 346 (2005) 165–184. https://doi.org/10.1016/J.JNUCMAT.2005.06.020.

[15] M. Li, N. Hashimoto, T.S. Byun, L.L. Snead, S.J. Zinkle, Defect cluster formation and radiation hardening in molybdenum neutron-irradiated at 80 °C, J. Nucl. Mater. 367–370 (2007) 817–822. https://doi.org/10.1016/J.JNUCMAT.2007.03.049.

[16] Y. Nemoto, A. Hasegawa, M. Satou, K. Abe, Y. Hiraoka, Microstructural development and radiation hardening of neutron irradiated Mo–Re alloys, J. Nucl. Mater. 324 (2004) 62–70. https://doi.org/10.1016/J.JNUCMAT.2003.09.007.

[17] R. Gröger, A.G. Bailey, V. Vitek, Multiscale modeling of plastic deformation of molybdenum and tungsten: I. Atomistic studies of the core structure and glide of 1/2〈1 1 1〉 screw dislocations at 0 K, Acta Mater. 56 (2008) 5401–5411. https://doi.org/10.1016/j.actamat.2008.07.018.

[18] V. Vitek, Core structure of screw dislocations in body-centred cubic metals: Relation to symmetry and interatomic bonding, Philos. Mag. 84 (2004) 415–428. https://doi.org/10.1080/14786430310001611644.

[19] C. Thomser, V. Bailescu, S. Brezinsek, J.W. Coenen, H. Greuner, T. Hirai, J. Linke, C.P. Lungu, H. Maier, G. Matthews, P.H. Mertens, R. Neu, V. Philipps, V. Riccardo, M. Rubel, C. Ruset, A. Schmidt, I. Uytdenhouwen, Plasma facing materials for the jet iter-like wall, Fusion Sci. Technol. 62 (2012) 1–8. https://doi.org/10.13182/FST12-A14103.

[20] Y. Cui, G. Po, N. Ghoniem, Temperature insensitivity of the flow stress in body-centered cubic micropillar crystals, Acta Mater. 108 (2016) 128–137. https://doi.org/10.1016/j.actamat.2016.02.008.

[21] A. Giannattasio, Z. Yao, E. Tarleton, S.G. Roberts, Brittle-ductile transitions in polycrystalline tungsten, Philos. Mag. 90 (2010) 3947–3959. https://doi.org/10.1080/14786435.2010.502145.

[22] D. Hull, REFORMATION AND FRACTURE OF TUNGSTEN SINGLE CRYSTALS of Metallurgy , The The deformation behaviour and fracture modes of tungsten single

crystals have been studied as a function of orientation . The orientation of the crystals was varied systematically ar, (1965).

[23] S.R. Malooft, PLASTIC DEFORMATION OF TUNGSTEN SINGLE LOW TEMPERATURES * CRYSTALS In spite of the early interest in the plastic defor- mation of b . c . c . metals most of the fundamental studies have been carried out on f . c . c . metals and ionic salts . Recently , d, (1966).

[24] B.G. Butler, J.D. Paramore, J.P. Ligda, C. Ren, Z.Z. Fang, S.C. Middlemas, K.J. Hemker, Mechanisms of deformation and ductility in tungsten – A review, Int. J. Refract. Met. Hard Mater. 75 (2018) 248–261. https://doi.org/10.1016/j.ijrmhm.2018.04.021.

[25] A. Joshi, D.F. Stein, Intergranular brittleness studies in Tungsten Using Auger Spectroscopy, Metall. Trans. 1 (1970) 2543–2546. https://doi.org/10.1007/BF03038381.

[26] Tran-Huu-Loi, J.P. Morniroli, M. Gantois, M. Lahaye, Brittle fracture of polycrystalline tungsten, J. Mater. Sci. 20 (1985) 199–206. https://doi.org/10.1007/BF00555913.

[27] B. Gludovatz, S. Wurster, T. Weingartner, A. Hoffmann, R. Pippan, Influence of impurities on the fracture behaviour of tungsten, Philos. Mag. 91 (2011) 3006–3020. https://doi.org/10.1080/14786435.2011.558861.

[28] Y. Cheng, M. Mrovec, P. Gumbsch, Atomistic simulations of interactions between the 1/2 〈111〉 edge dislocation and symmetric tilt grain boundaries in tungsten, Philos. Mag. 88 (2008) 547–560. https://doi.org/10.1080/14786430801894577.

[29] G.S. Was, Fundamentals of radiation materials science: Metals and alloys, second edition, 2016. https://doi.org/10.1007/978-1-4939-3438-6.

[30] J. Pokluda, P. Šandera, On the Intrinsic Ductility and Brittleness of Crystals, Phys. Status Solidi. 167 (1929) 543–550. https://doi.org/10.1002/pssb.2221670216.

[31] E. Orowan, Fracture and strength of solids, Reports Prog. Phys. 12 (1949) 185–232. https://doi.org/10.1088/0034-4885/12/1/309.

[32] A.A. Griffits, The phenomena of rupture and flow in solids, Masinovedenie. (1995) 9–14. https://doi.org/10.1098/rsta.1921.0006.

[33] R.O. Ritchie, The conflicts between strength and toughness, Nat. Mater. 10 (2011) 817–822. https://doi.org/10.1038/nmat3115.

[34] L. Ji, S. Zou, M. Shen, Y. Xin, Radio frequency underwater discharge operation and its application to Congo Red degradation, Plasma Sci. Technol. 14 (2012) 111–117. https://doi.org/10.1088/1009-0630/14/2/06.

[35] W.D. Kzopp, REVIEW OF DUCTILIZING OF GROUP Il 1 l l 1 l 1, Group. (1968).

[36] L. Romaner, C. Ambrosch-Draxl, R. Pippan, Effect of rhenium on the dislocation core structure in tungsten, Phys. Rev. Lett. 104 (2010) 1–4. https://doi.org/10.1103/PhysRevLett.104.195503.

[37] W. Setyawan, R.J. Kurtz, Effects of transition metals on the grain boundary cohesion in tungsten, Scr. Mater. 66 (2012) 558–561.

https://doi.org/10.1016/j.scriptamat.2012.01.002.

[38] L. El-Guebaly, R. Kurtz, M. Rieth, H. Kurishita, A. Robinson, W-Based Alloys for Advanced Divertor Designs: Options and Environmental Impact of State-of-the-Art Alloys, Fusion Sci. Technol. 60 (2011) 185–189. https://doi.org/10.13182/fst11-a12349.

[39] W.F. Seng, P.A. Barnes, Calculations of cobalt suicide and carbide formation on SiC using the Gibbs free energy, Mater. Sci. Eng. B Solid-State Mater. Adv. Technol. 76 (2000) 225–231. https://doi.org/10.1016/S0921-5107(00)00457-8.

[40] A. Hasegawa, M. Fukuda, S. Nogami, K. Yabuuchi, Neutron irradiation effects on tungsten materials, Fusion Eng. Des. 89 (2014) 1568–1572. https://doi.org/10.1016/j.fusengdes.2014.04.035.

[41] S. Wurster, N. Baluc, M. Battabyal, T. Crosby, J. Du, C. García-Rosales, A. Hasegawa, A. Hoffmann, A. Kimura, H. Kurishita, R.J. Kurtz, H. Li, S. Noh, J. Reiser, J. Riesch, M. Rieth, W. Setyawan, M. Walter, J.H. You, R. Pippan, Recent progress in R&D on tungsten alloys for divertor structural and plasma facing materials, J. Nucl. Mater. 442 (2013) 181–189. https://doi.org/10.1016/j.jnucmat.2013.02.074.

[42] S. Wurster, B. Gludovatz, A. Hoffmann, R. Pippan, Fracture behaviour of tungsten-vanadium and tungsten-tantalum alloys and composites, J. Nucl. Mater. 413 (2011) 166–176. https://doi.org/10.1016/j.jnucmat.2011.04.025.

[43] M. V. Aguirre, A. Martín, J.Y. Pastor, J. Llorca, M.A. Monge, R. Pareja, Mechanical properties of Y2O3-doped W-Ti alloys, J. Nucl. Mater. 404 (2010) 203–209. https://doi.org/10.1016/j.jnucmat.2010.07.016.

[44] M. V. Aguirre, A. Martín, J.Y. Pastor, J. Llorca, M.A. Monge, R. Pareja, Mechanical behavior of W-Y2O3 and W-Ti Alloys from 25 °C to 1000 °C, Metall. Mater. Trans. A Phys. Metall. Mater. Sci. 40 (2009) 2283–2290. https://doi.org/10.1007/s11661-009-9956-4.

[45] G.C. Wu, Q. You, D. Wang, Influence of the addition of Lanthanum on a W-Mo-Ni-Fe heavy alloy, Int. J. Refract. Met. Hard Mater. 17 (1999) 299–304. https://doi.org/10.1016/S0263-4368(99)00015-3.

[46] N. Senthilnathan, A.R. Annamalai, G. Venkatachalam, Microstructure and mechanical properties of spark plasma sintered tungsten heavy alloys, Mater. Sci. Eng. A. 710 (2018) 66–73. https://doi.org/10.1016/j.msea.2017.10.080.

[47] Y. Şahin, Recent Progress in Processing of Tungsten Heavy Alloys, J. Powder Technol. 2014 (2014) 1–22. https://doi.org/10.1155/2014/764306.

[48] X. Gong, J. Fan, F. Ding, Tensile mechanical properties and fracture behavior of tungsten heavy alloys at 25-1100 °C, Mater. Sci. Eng. A. 646 (2015) 315–321. https://doi.org/10.1016/j.msea.2015.08.079.

[49] A. Kumari, G. Prabhu, M. Sankaranarayana, T.K. Nandy, Effect of solution treatment temperature and cooling rate on the mechanical properties of tungsten heavy alloy, Mater. Sci. Eng. A. 688 (2017) 225–236. https://doi.org/10.1016/j.msea.2017.01.113.

[50] M. Battabyal, R. Schäublin, P. Spätig, N. Baluc, W-2wt.%Y 2O 3 composite: Microstructure and mechanical properties, Mater. Sci. Eng. A. 538 (2012) 53–57. https://doi.org/10.1016/j.msea.2012.01.011.

[51] B. Huang, L. Chen, W. Qiu, X. Yang, K. Shi, Y. Lian, X. Liu, J. Tang, Correlation between the microstructure, mechanical/thermal properties, and thermal shock resistance of K-doped tungsten alloys, J. Nucl. Mater. 520 (2019) 6–18. https://doi.org/10.1016/j.jnucmat.2019.03.056.

[52] Y. Shen, Z. Xu, K. Cui, J. Yu, Microstructure of a commercial W-1% La2O3 alloy, J. Nucl. Mater. 455 (2014) 234–241. https://doi.org/10.1016/j.jnucmat.2014.06.004.

[53] L. Xu, Q. Yan, M. Xia, L. Zhu, Preparation of La2O3 doped ultra-fine W powders by hydrothermal-hydrogen reduction process, Int. J. Refract. Met. Hard Mater. 36 (2013) 238–242. https://doi.org/10.1016/j.ijrmhm.2012.09.005.

[54] I. Smid, M. Akiba, G. Vieider, L. Plöchl, Development of tungsten armor and bonding to copper for plasma-interactive components, J. Nucl. Mater. 258–263 (1998) 160–172. https://doi.org/10.1016/S0022-3115(98)00358-4.

[55] M. Rieth, B. Dafferner, Limitations of W and W-1%La2O3 for use as structural materials, J. Nucl. Mater. (2005). https://doi.org/10.1016/j.jnucmat.2005.03.013.

[56] H.O. Munekazu IINUMA, Toshiyuki TANAKA, Mizuo MIZUNO, Tomoyuki KATSUZAKI, NII-Electronic Library Service, Chem. Pharm. Bull. (2002) 2091. http://www.mendeley.com/research/geology-volcanic-history-eruptive-style-yakedake-volcano-group-central-japan/.

[57] H. Kurishita, S. Kobayashi, K. Nakai, H. Arakawa, S. Matsuo, T. Takida, K. Takebe, M. Kawai, Current status of ultra-fine grained W-TiC development for use in irradiation environments, Phys. Scr. T. T128 (2007) 76–80. https://doi.org/10.1088/0031-8949/2007/T128/015.

[58] H. Kurishita, S. Kobayashi, K. Nakai, T. Ogawa, A. Hasegawa, K. Abe, H. Arakawa, S. Matsuo, T. Takida, K. Takebe, M. Kawai, N. Yoshida, Development of ultra-fine grained W-(0.25-0.8)wt%TiC and its superior resistance to neutron and 3 MeV He-ion irradiations, J. Nucl. Mater. 377 (2008) 34–40. https://doi.org/10.1016/j.jnucmat.2008.02.055.

[59] H. Kurishita, S. Matsuo, H. Arakawa, T. Sakamoto, S. Kobayashi, K. Nakai, T. Takida, M. Kato, M. Kawai, N. Yoshida, Development of re-crystallized W-1.1%TiC with enhanced room-temperature ductility and radiation performance, J. Nucl. Mater. 398 (2010) 87–92. https://doi.org/10.1016/j.jnucmat.2009.10.015.

[60] S. Antusch, D.E.J. Armstrong, T. Ben Britton, L. Commin, J.S.K.L. Gibson, H. Greuner, J. Hoffmann, W. Knabl, G. Pintsuk, M. Rieth, S.G. Roberts, T. Weingaertner, Mechanical and microstructural investigations of tungsten and doped tungsten materials produced via powder injection molding, Nucl. Mater. Energy. 3–4 (2015) 22–31. https://doi.org/10.1016/j.nme.2015.04.002.

[61] E.M. Garcia-Ayala, S. Tarancon, Z. Gonzalez, B. Ferrari, J.Y. Pastor, A.J. Sanchez-

Herencia, Processing of WC/W composites for extreme environments by colloidal dispersion of powders and SPS sintering, Int. J. Refract. Met. Hard Mater. 84 (2019) 105026. https://doi.org/10.1016/j.ijrmhm.2019.105026.

[62] A. Šestan, J. Zavašnik, M.M. Kržmanc, M. Kocen, P. Jenuš, S. Novak, M. Čeh, G. Dehm, Tungsten carbide as a deoxidation agent for plasma-facing tungsten-based materials, J. Nucl. Mater. 524 (2019) 135–140. https://doi.org/10.1016/j.jnucmat.2019.06.030.

[63] S. Chanthapan, A. Kulkarni, J. Singh, C. Haines, D. Kapoor, Sintering of tungsten powder with and without tungsten carbide additive by field assisted sintering technology, Int. J. Refract. Met. Hard Mater. 31 (2012) 114–120. https://doi.org/10.1016/j.ijrmhm.2011.09.014.

[64] R. Liu, Z.M. Xie, J.F. Yang, T. Zhang, T. Hao, X.P. Wang, Q.F. Fang, C.S. Liu, Recent progress on the R&D of W-ZrC alloys for plasma facing components in fusion devices, Nucl. Mater. Energy. 16 (2018) 191–206. https://doi.org/10.1016/j.nme.2018.07.002.

[65] Y.K. Wang, S. Miao, Z.M. Xie, R. Liu, T. Zhang, Q.F. Fang, T. Hao, X.P. Wang, C.S. Liu, X. Liu, L.H. Cai, Thermal stability and mechanical properties of HfC dispersion strengthened W alloys as plasma-facing components in fusion devices, J. Nucl. Mater. 492 (2017) 260–268. https://doi.org/10.1016/j.jnucmat.2017.05.038.

[66] M.A. Umer, D. Lee, O.A. Waseem, H.J. Ryu, S.H. Hong, Fabrication of protective-coated SiC reinforced tungsten matrix composites with reduced reaction phases by spark plasma sintering, Met. Mater. Int. 22 (2016) 493–500. https://doi.org/10.1007/s12540-016-5700-y.

[67] Y. Wang, M. Chen, F. Zhou, E. Ma, High tensile ductility in a nanostructured metal, Nature. 419 (2002) 912–915. https://doi.org/10.1038/nature01133.

[68] R.Z. Valiev, I. V. Alexandrov, Y.T. Zhu, T.C. Lowe, Paradox of strength and ductility in metals processed by severe plastic deformation, J. Mater. Res. 17 (2002) 5–8. https://doi.org/10.1557/JMR.2002.0002.

[69] C. Bonnekoh, P. Lied, W. Pantleon, T. Karcher, H. Leiste, A. Hoffmann, J. Reiser, M. Rieth, The brittle-to-ductile transition in cold-rolled tungsten sheets: On the loss of room-temperature ductility after annealing and the phenomenon of 45° embrittlement, Int. J. Refract. Met. Hard Mater. 93 (2020) 105347. https://doi.org/10.1016/j.ijrmhm.2020.105347.

[70] P. Li, X. Wang, K.M. Xue, Y. Tian, Y.C. Wu, Microstructure and recrystallization behavior of pure W powder processed by high-pressure torsion, Int. J. Refract. Met. Hard Mater. 54 (2016) 439–444. https://doi.org/10.1016/j.ijrmhm.2015.10.004.

[71] A. V. Ganeev, R.K. Islamgaliev, R.Z. Valiev, Refinement of tungsten microstructure upon severe plastic deformation, Phys. Met. Metallogr. 115 (2014) 139–145. https://doi.org/10.1134/S0031918X14020070.

[72] P. Gumbsch, Brittle fracture and the brittle-to-ductile transition of tungsten, J. Nucl. Mater. 323 (2003) 304–312. https://doi.org/10.1016/j.jnucmat.2003.08.009.

[73] D. Rupp, R. Mönig, P. Gruber, S.M. Weygand, Fracture toughness and microstructural

characterization of polycrystalline rolled tungsten, Int. J. Refract. Met. Hard Mater. 28 (2010) 669–673. https://doi.org/10.1016/j.ijrmhm.2010.05.006.

[74] M. Zhao, Z. Zhou, M. Zhong, J. Tan, Effect of hot rolling on the microstructure and fracture behavior of a bulk fine-grained W-Y2O3 alloy, Mater. Sci. Eng. A. 646 (2015) 19–24. https://doi.org/10.1016/j.msea.2015.08.045.

[75] J. Reiser, J. Hoffmann, U. Jäntsch, M. Klimenkov, S. Bonk, C. Bonnekoh, A. Hoffmann, T. Mrotzek, M. Rieth, Ductilisation of tungsten (W): On the increase of strength AND room-temperature tensile ductility through cold-rolling, Int. J. Refract. Met. Hard Mater. 64 (2017) 261–278. https://doi.org/10.1016/j.ijrmhm.2016.10.018.

[76] X. Zhang, Q. Yan, S. Lang, M. Xia, C. Ge, Texture evolution and basic thermal–mechanical properties of pure tungsten under various rolling reductions, J. Nucl. Mater. 468 (2016) 339–347. https://doi.org/10.1016/J.JNUCMAT.2015.04.001.

[77] R. Liu, Z.M. Xie, T. Zhang, Q.F. Fang, X.P. Wang, T. Hao, C.S. Liu, Y. Dai, Mechanical properties and microstructures of W-1%Y2O3 microalloyed with Zr, Mater. Sci. Eng. A. 660 (2016) 19–23. https://doi.org/10.1016/J.MSEA.2016.02.072.

[78] Y.K. Wang, S. Miao, Z.M. Xie, R. Liu, T. Zhang, Q.F. Fang, T. Hao, X.P. Wang, C.S. Liu, X. Liu, L.H. Cai, Thermal stability and mechanical properties of HfC dispersion strengthened W alloys as plasma-facing components in fusion devices, J. Nucl. Mater. 492 (2017) 260–268. https://doi.org/10.1016/J.JNUCMAT.2017.05.038.

[79] X. Zhang, Q. Yan, S. Lang, M. Xia, C. Ge, Basic thermal–mechanical properties and thermal shock, fatigue resistance of swaged + rolled potassium doped tungsten, J. Nucl. Mater. 452 (2014) 257–264. https://doi.org/10.1016/J.JNUCMAT.2014.05.032.

[80] Z.M. Xie, R. Liu, S. Miao, X.D. Yang, T. Zhang, Q.F. Fang, X.P. Wang, C.S. Liu, Y.Y. Lian, X. Liu, G.N. Luo, High thermal shock resistance of the hot rolled and swaged bulk W–ZrC alloys, J. Nucl. Mater. 469 (2016) 209–216. https://doi.org/10.1016/J.JNUCMAT.2015.10.052.

[81] P. Li, X. Wang, K.M. Xue, Y. Tian, Y.C. Wu, Microstructure and recrystallization behavior of pure W powder processed by high-pressure torsion, Int. J. Refract. Met. Hard Mater. 54 (2016) 439–444. https://doi.org/10.1016/J.IJRMHM.2015.10.004.

[82] T. Hao, Z.Q. Fan, T. Zhang, G.N. Luo, X.P. Wang, C.S. Liu, Q.F. Fang, Strength and ductility improvement of ultrafine-grained tungsten produced by equal-channel angular pressing, J. Nucl. Mater. 455 (2014) 595–599. https://doi.org/10.1016/J.JNUCMAT.2014.08.044.

[83] M. Rieth, A. Hoffmann, Influence of microstructure and notch fabrication on impact bending properties of tungsten materials, Int. J. Refract. Met. Hard Mater. 28 (2010) 679–686. https://doi.org/10.1016/J.IJRMHM.2010.04.010.

[84] J. Reiser, L. Garrison, H. Greuner, J. Hoffmann, T. Weingärtner, U. Jäntsch, M. Klimenkov, P. Franke, S. Bonk, C. Bonnekoh, S. Sickinger, S. Baumgärtner, D. Bolich, M. Hoffmann, R. Ziegler, J. Konrad, J. Hohe, A. Hoffmann, T. Mrotzek, M. Seiss, M. Rieth, A. Möslang, Ductilisation of tungsten (W): Tungsten laminated composites, Int. J.

Refract. Met. Hard Mater. 69 (2017) 66–109. https://doi.org/10.1016/J.IJRMHM.2017.07.013.

[85] Q. Wei, L.J. Kecskes, Effect of low-temperature rolling on the tensile behavior of commercially pure tungsten, Mater. Sci. Eng. A. 491 (2008) 62–69. https://doi.org/10.1016/J.MSEA.2008.01.013.

[86] H.L. Ding, Z.M. Xie, Q.F. Fang, T. Zhang, Z.J. Cheng, Z. Zhuang, X.P. Wang, C.S. Liu, Determination of the DBTT of nanoscale ZrC doped W alloys through amplitude-dependent internal friction technique, Mater. Sci. Eng. A. 716 (2018) 268–273. https://doi.org/10.1016/J.MSEA.2018.01.055.

[87] H.Y. Guo, M. Xia, L.C. Chan, K. Wang, X.X. Zhang, Q.Z. Yan, M.C. He, J. Lu, C.C. Ge, Nanostructured laminar tungsten alloy with improved ductility by surface mechanical attrition treatment, Sci. Rep. 7 (2017) 1–11. https://doi.org/10.1038/s41598-017-01458-0.

[88] J. Riesch, Y. Han, J. Almanstötter, J.W. Coenen, T. Höschen, B. Jasper, P. Zhao, C. Linsmeier, R. Neu, Development of tungsten fibre-reinforced tungsten composites towards their use in DEMO - Potassium doped tungsten wire, in: Phys. Scr., 2016. https://doi.org/10.1088/0031-8949/T167/1/014006.

[89] H. Gietl, J. Riesch, J.W. Coenen, T. Höschen, C. Linsmeier, R. Neu, Tensile deformation behavior of tungsten fibre-reinforced tungsten composite specimens in as-fabricated state, Fusion Eng. Des. 124 (2017) 396–400. https://doi.org/10.1016/J.FUSENGDES.2017.02.054.

[90] R. Neu, J. Riesch, A. V. Müller, M. Balden, J.W. Coenen, H. Gietl, T. Höschen, M. Li, S. Wurster, J.H. You, Tungsten fibre-reinforced composites for advanced plasma facing components, Nucl. Mater. Energy. 12 (2017) 1308–1313. https://doi.org/10.1016/J.NME.2016.10.018.

[91] J. Riesch, J.Y. Buffiere, T. Höschen, M. Di Michiel, M. Scheel, C. Linsmeier, J.H. You, In situ synchrotron tomography estimation of toughening effect by semi-ductile fibre reinforcement in a tungsten-fibre-reinforced tungsten composite system, Acta Mater. 61 (2013) 7060–7071. https://doi.org/10.1016/J.ACTAMAT.2013.07.035.

[92] J. Riesch, J. Almanstötter, J.W. Coenen, M. Fuhr, H. Gietl, Y. Han, T. Höschen, C. Linsmeier, N. Travitzky, P. Zhao, R. Neu, Properties of drawn W wire used as high performance fibre in tungsten fibre-reinforced tungsten composite, IOP Conf. Ser. Mater. Sci. Eng. 139 (2016). https://doi.org/10.1088/1757-899X/139/1/012043.

[93] Y. Mao, J.W. Coenen, J. Riesch, S. Sistla, J. Almanstötter, B. Jasper, A. Terra, T. Höschen, H. Gietl, C. Linsmeier, C. Broeckmann, Influence of the interface strength on the mechanical properties of discontinuous tungsten fiber-reinforced tungsten composites produced by field assisted sintering technology, Compos. Part A Appl. Sci. Manuf. 107 (2018) 342–353. https://doi.org/10.1016/J.COMPOSITESA.2018.01.022.

[94] B. Jasper, S. Schoenen, J. Du, T. Hoeschen, F. Koch, C. Linsmeier, R. Neu, J. Riesch, A. Terra, J.W. Coenen, Behavior of tungsten fiber-reinforced tungsten based on single fiber push-out study, Nucl. Mater. Energy. 9 (2016) 416–421. https://doi.org/10.1016/j.nme.2016.04.010.

[95] T. Hinoki, Y. Katoh, A. Kohyama, Effect of fiber properties on neutron irradiated SiC/SiC composites, Mater. Trans. 43 (2002) 617–621. https://doi.org/10.2320/matertrans.43.617.

[96] T. Koyanagi, K. Ozawa, T. Hinoki, K. Shimoda, Y. Katoh, Effects of neutron irradiation on mechanical properties of silicon carbide composites fabricated by nano-infiltration and transient eutectic-phase process, J. Nucl. Mater. 448 (2014) 478–486. https://doi.org/10.1016/j.jnucmat.2013.10.005.

[97] L.L. Snead, T. Nozawa, Y. Katoh, T.S. Byun, S. Kondo, D.A. Petti, Handbook of SiC properties for fuel performance modeling, J. Nucl. Mater. 371 (2007) 329–377. https://doi.org/10.1016/j.jnucmat.2007.05.016.

[98] S.J. Zinkle, A. Möslang, T. Muroga, H. Tanigawa, Multimodal options for materials research to advance the basis for fusion energy in the ITER era, Nucl. Fusion. 53 (2013). https://doi.org/10.1088/0029-5515/53/10/104024.

[99] S.J. Zinkle, N.M. Ghoniem, Operating temperature windows for fusion reactor structural materials, Fusion Eng. Des. 51–52 (2000) 55–71. https://doi.org/10.1016/S0920-3796(00)00320-3.

Chapter 2 The fabrication and evaluation methods of SiC fiber reinforced metal composites

2.1 Introduction

The divertor environment in the fusion reactor is extremely harsh for materials owing to heat load and sputtering by plasma and neutron. Tungsten (W) is the most promising candidate for divertor, but its brittleness properties caused by high ductile-brittle transition temperature (DBTT) and further embrittlement in a neutron irradiation environment are restrictions. In addition, the toughness deteriorates caused by the recrystallization behavior, causing the narrow operating temperature window of W between DBTT and recrystallization temperature.

To improve the toughness of brittle materials, fiber reinforcement has been developed as a successful method for decades, in which SiC fiber is widely used because of its extraordinary mechanical properties even at temperature [1] higher than the recrystallization temperature of W. In this study, a completely new method, to strengthen W with SiC ceramic filaments by hot press that can obtain excellent fracture toughness, was to give more choices for divertor application retaining excellent W features including stability to plasma sputtering and high thermal conductivity. Since tungsten and SiC have very close thermal expansion coefficients, and the swelling of SiC at the operating temperature window of W (800 °C to 1300 °C [2]) by neutron irradiation is lower than 1% [3], so the stress generated at the interface is minor due to the mismatch of CTE (coefficient of thermal expansion). In addition, SiC materials also exhibit excellent mechanical properties in a neutron irradiation environment [4]. In this work, SiC fiber as reinforcement was used to fabricate W composites by hot-press, then the mechanical property was examined by tensile test to evaluate whether the SiC fiber can raise the toughness of W or not. In addition, to prevent the reactions between SiC and metals, diffusion couples with or without coating were also prepared.

2.2 Methods to fabricate fiber reinforced composites

Two methods were used to fabricate the composites in this study. The schematic diagram about the fabrication of composites in this work is shown as Fig. 2.1. Composites with or without diffusion barrier and with or without W foils were synthesized by hot-press sintered in graphite die with 40 × 40 mm^2 or 40× 40 × 22 mm^2 size at different temperature from 1500 °C to 1900 °C in Ar atmosphere for 1 h with 20 MPa pressure using continuous woven Hi-Nicalon type S SiC

fiber (NGS Advanced Fibers Co., Ltd.), the thickness of fiber tow is about 0.1 mm. W or Mo powder (grain size 0.6 um, Kojundo Chemical Laboratory Co. Ltd) and W or Mo foil (Kstrading Co., Ltd) as raw materials in this work. And C interface is produced by pyrolysis of phenolic resin (PR-50273, Sumitomo Bakelite Co., Ltd). For both methods, fibers were desized at 500 °C before they were used, and also slurry was prepared.

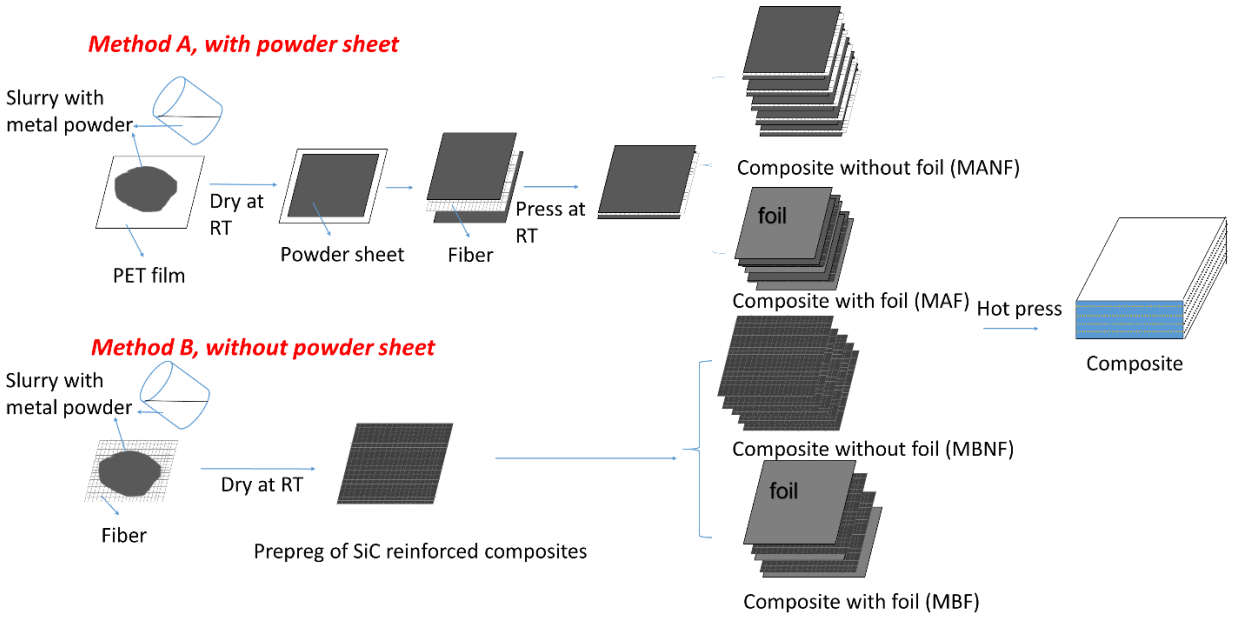

Figure 2.1 Preparation methods of SiC fiber reinforce metal composites.

For method A (MA), only woven SiC fiber was used. W powder sheet was prepared firstly. W powders and PVB (5:1 with weight ratio) dispersed in isopropanol by ball milling by ball-milling for 24 h using W balls to prepare slurry for composites. Subsequently, the slurry was poured on the PET film, later the slurry dried at room temperature. After drying, then woven fibers and the powder sheets stacked together were pressed to sandwich-like under 5 MPa at room temperature. The thickness of dried powder sheet is about 0.042 mm. Then the pressed prepreg was cut to a suitable size for hot press. The image of the arrangement pepreg before hot pressure was shown in Fig. 2.2. Besides, W foils are also used in this work due to high density, and they were washed by NaOH solution (0.98 wt%) using ultrasonic cleaning to remove WO_3 on the surface of W foil.

In addition, for method B (MB), W powder and PVB (30:1 with weight ratio) were dispersed in acetone. Then fibers were infiltrated in W slurry directly, then also dried at room

temperature. In addition, all composites were hot-pressed in a graphite die at different temperature (1500 °C, 1700 °C and 1900 °C) for 1 h under a pressure of 20 MPa in argon atmosphere, and the sintering curve revealed at Fig. 2.3. Moreover, the pressure at about 200 °C is to press the softened W powders with PVB to fiber bundle.

Figure 2.2 The prepreg of MANF before sintering.

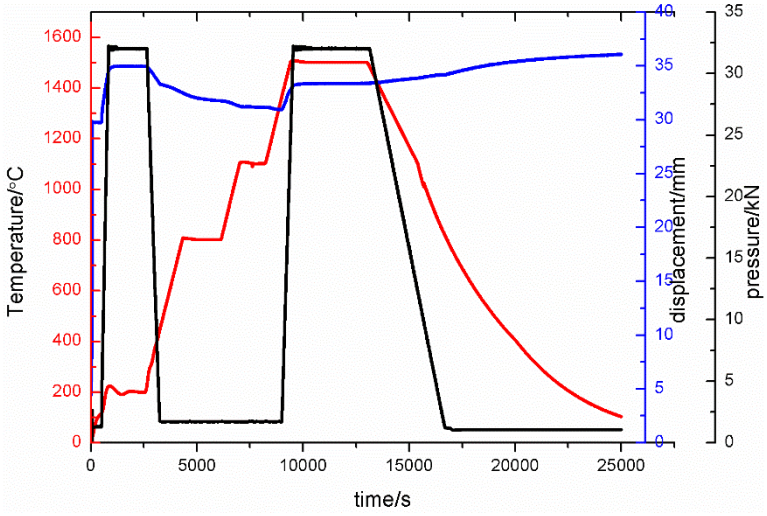

Figure 2.3 Typical sintering process in this work. (red for temperature; black for pressure; blue for the displacement change during sintering).

2.3 The choice of solvent

The sedimentation of the solute is important in a slurry, especially for MA. The W powders should be stable during drying without deposition. The sedimentation coefficient ($s=\frac{m}{6\pi\eta r}$, where m is the excess mass of the particle over and above the mass of an equivalent volume of the fluid

in which the particle is situated, η is the viscosity of the medium, and r is the radius of the particle) of a particle characterizes its sedimentation during centrifugation. From this equation, the higher η of the slurry, the lower sedimentation coefficient. However, high η slurry might be difficult to disperse uniformly, and difficult to go inside of the fiber bundle. Therefore, the viscosity of the slurry measured by the viscometer at the beginning to select a suitable solvent.

Table 2.1 The viscosity of slurry with different weight ratio in different solvent.

η/(dPa·s)	20 wt% slurry	30 wt% slurry	35 wt% slurry	40 wt% slurry
Acetone	≤ 0.3	0.5	0.83	2.2
Ethanol	0.32	0.75	2.1	4.7
Isopropanol	0.41	1.1	3.4	5.8

The viscosity of slurry with 3 kinds of solvents, i.e., ethanol, acetone, and isopropanol were tested in this work for MA. In addition, the weight ratio also has an effect on η, therefore the slurry with different weight ratio from 20 wt% to 40 wt% were also investigated. The viscosity values were exhibited in Table 2.1. Moreover, the dried W powder sheets were shown in Fig. 2.4, and the acceptable solvents and weight ratio were marked the red rectangle. When acetone as the solvent, W powders settle on the PET film until the weight ratio is 35 wt%, and only 40 wt% slurry of 2.2 dPa·s can remove from PET film without remained powders (see Fig. 2.4 a4)). For slurry with ethanol, the 35 wt% solute is enough, and the value of η is 2.1 dPa·s lower than 40 wt% slurry with acetone. However, 1.1 dPa·s η slurry used isopropanol with 30 wt% W powders can already obtain an ideal sheet. Therefore, isopropanol was selected as solvent for MA, and the W powders in slurry is 30 wt%.

Figure 2.4 The tungsten powder sheet for MA. a) for acetone as solvent and the weight ratio are from 20 wt% to 40 wt% respectively; b) for ethanol as solvent; c) for isopropanol as solvent.

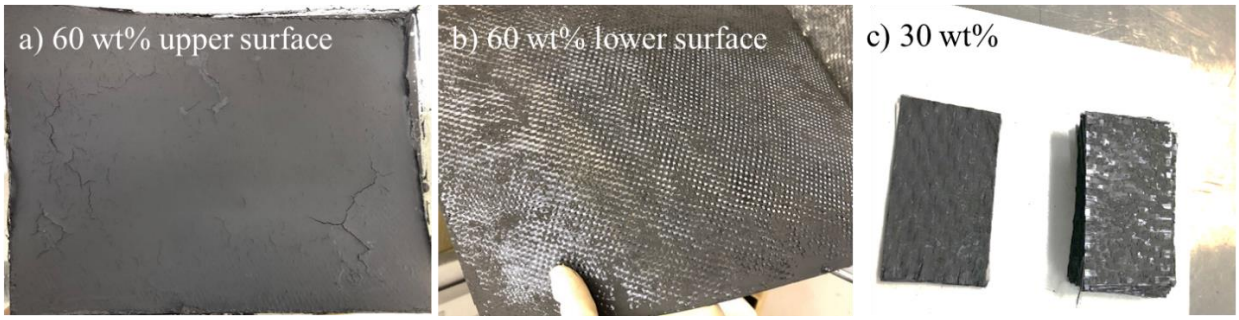

Figure 2.5 The photo of upper and lower surfaces of SiC fiber with W powder by a), b) 60 wt% and c) 30 wt%.

Acetone as solvent was used in slurry for MB, because it is easy to go inside of the fiber bundle due to the lowest viscosity. In addition, the appropriate ratio of solute was studied. 2 weight ratio were investigated, 60 wt% and 30 wt% respectively. The slurry was prepared as the same way as MA. Details were described in 2.2. The SiC fiber with dried W powder prepreg is shown in Fig. 2.5. When the weight ratio is 60 wt%, the viscosity is 0.43 dPa·s, and the slurry can't disperse in the fiber bundle uniformly, which caused the large difference between upper and lower surface. On the upper surface, only dried W powders can be found, while there are little powders

in most area on the lower surface. For prepreg from 30 wt% slurry, the powders distributed more uniform on both sides compared with prepreg from 60 wt% slurry. Therefore, the weight ratio is 30 wt% for MB.

2.4 The fabrication of diffusion couple

Dipping method might be a suitable way for coating fiber because the surface of the inner side fiber in the fiber tow can be coated easily, and on the other side, the interface between fiber and coating is not very dense, which might satisfy the weak bonding in composites to bring additional toughness by crack deflection and fiber frictional sliding to consume energy.

Seven kinds of materials (oxides (ZrO_2, TiO_2, & Er_2O_3), carbides (ZrC, & TiC), nitrides (ZrN, & TiN)) were prepared by dipping method and evaluated as diffusion barrier for SiC/W system in this work, besides sputtering method (nitrides) were also investigated to prevent the reaction. And the substrate is CVD-SiC plate in all cases to replace SiC fiber. Because it is convenient to coat on a plate than fiber by both dipping and sputtering method, and a joined specimen are easy to prepare and analyze the reacted thickness. Subsequently, to investigate which coating is feasible, the sandwich-like specimens were prepared by joining the coated CVD-SiC plates and W foils at the similar condition with sintering SiC_f/W composites to simulate the sintering procedure of composites (see Fig. 2.6), namely 1700 °C for 1h with 20 MPa in Ar atmosphere.

Before joining, the dipped CVD-SiC plates were dried at 120 °C for 10 min, then annealed at 500 °C for 1h in air to generate oxides coating. And for carbides, carbon black powders were added to the liquid precursor before dipping, then mixed well by ultrasonic treatment. Afterwards, similar condition with generating oxides was used to prepare C dispersed oxide film. Subsequently, the coated SiC was annealed at 1600 °C for 2h in Ar atmosphere to produce carbide coating by carbothermic reduction reaction. Besides, for nitrides, two kinds of methods (sputtering and dipping method), were used in this work. To produce nitrides coating by dipping method, oxide films were generated firstly, later the oxides coated SiC plates were annealed at 1400 °C for 2h in flowing N_2 to generate nitrides. To fabricate the carbides and nitrides coating by multiple dipping from oxides, high temperature annealing was carried out after dipped every time. In addition, the sputtered nitrides coatings were generated from metals (Ti and Zr) film with about 300 nm

thickness after annealing at the same condition with a nitride film by dipping, which were coated at the Osaka Research Institute of Industrial Science and Technology. In addition, approximately 300 nm C is deposited firstly before the metal was coated to prevent the reactions between metals (Zr and Ti) and SiC.

The uncoated CVD-SiC joined with W foils was also investigated for comparison. And for the diffusion barriers by dipping method, SiC was dipped from once to 5 times. The used precursors to coat diffusion barrier films in this work were coating materials from Kojundo Chemical Laboratory Co., LTD. (TIK03LB for Ti-based coating, ZRK03LB for Zr-based coating, and ERK0E1LB for Er-based coating). The used W foils with thickness of 0.05 mm were purchased from E-metals Co., Ltd.

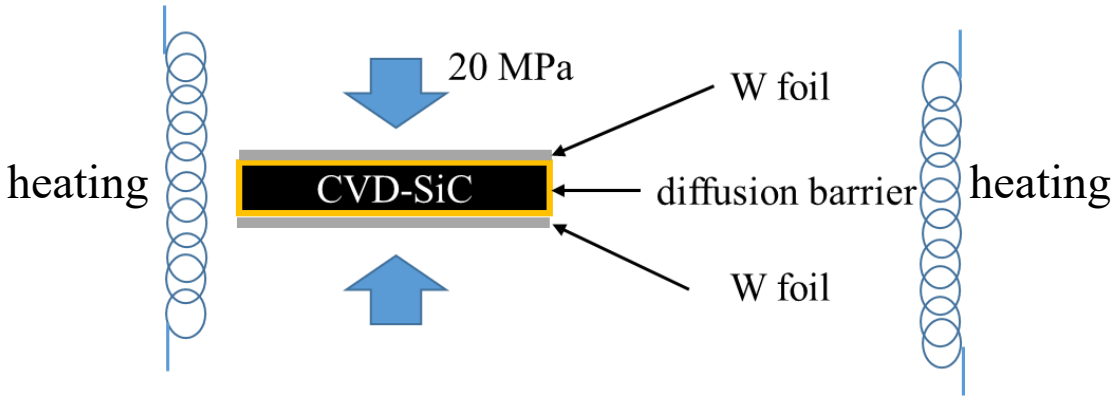

Figure 2.6. Schematic diagram of W joined with diffusion barrier coated CVD-SiC

2.5 Property evaluation

2.5.1 Tensile test

Tensile tests were carried out by Instron-5581 at room temperature to assess the mechanical properties. The size of testing bar is 3×1.5×40 mm^3. For composite with foils by both methods, the rolling direction was parallel to the 40 mm side, which is also the same as the loading direction. All surfaces were grinded, and two pieces of strain gauge were pasted to 3×40 mm^2 surface respectively before measurement. The strength is from the equation of $\sigma = \frac{F}{A}$, here σ is tensile test

strength, F is the loading on the specimen, and A is cross-sectional area of the tested sample. Six bars were measured for each composite, in which 3 bars were annealed at 1000 °C for 1 h.

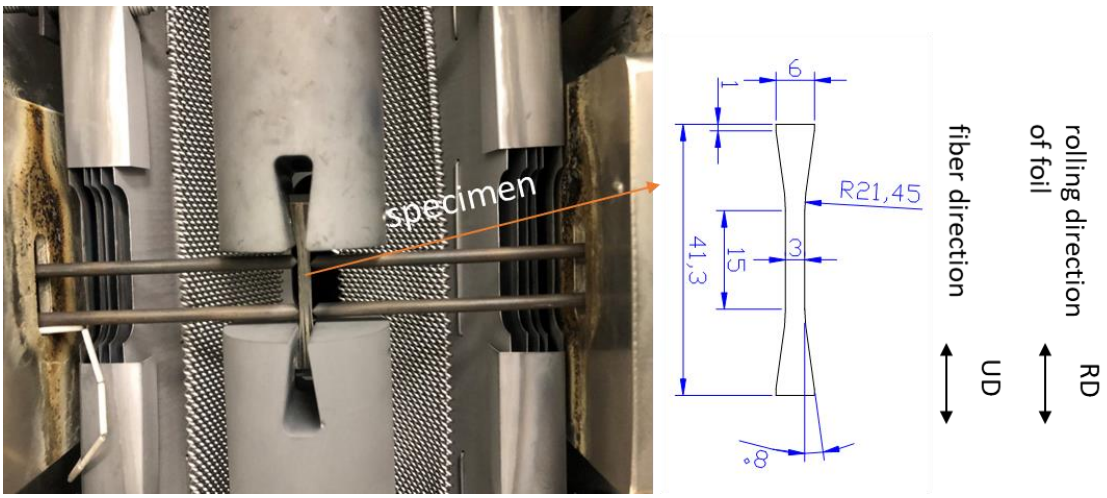

Figure 2.7 The fixture and the geometry of specimen for tensile test at high temperature

In this work, we also focus on the tensile strength at 1000 °C of SiC$_f$/W composites. Moreover, before heating, the pressure in the furnace was reduced to $\leqslant 10^{-4}$ Pa to avoid the influence of oxygen. The geometry of the sample and the used fixture for high temperature tensile test are displayed in Fig. 2.7. Herein, the thickness is 2 mm. The 2 stick-like matter on both sides act as strain gauge to measure the real deformation.

2.5.2 Thermal property

The heat capacity was measured by differential scanning calorimetry (DSC, Rigaku Co.), and thermal diffusivity of composites were tested by light flash apparatus (LFA, Netzsch) using the specimen with a diameter of 6 mm and thickness of 2 mm from through-plane (x) and in-plane (y) directions. Then the thermal conductivity was calculated by the equation of $\lambda = Cp * \rho * a$ (λ, thermal conductivity; ρ, density; a, thermal diffusivity; Cp, heat capacity), in which density is calculated from geometry due to the large difference of the values tested by densimeter and from size.

2.5.3 Microstructure and phase/element analysis

Microstructure of composites were observed by scanning electron microscopy in secondary electrons (SE) mode (SEM, ZEISS Ultra-55). In this work, electron probe micro analyzer (EPMA, JEOL JXA-8500F) is used for element analysis because energy-dispersive X-ray spectroscopy (EDS, EDAX) cannot distinguish W and Si element for the reason that Kα emission energy between W and Si is too close. EDS was used to evaluate the distribution of Mo. The phase analysis was carried out by X-ray diffraction (XRD, Rigaku) using Co target.

2.5.4 Density

The real density (ρr) and volume (Vr) is measured by Shimadzu AccuPyc II 1340 using helium gas. Before voulume test, the weight (m1) was measured firstly. Besides, to understand the open porosity (Po), the mass in pure water (m2) and the mass (m3) of the same specimen filled with water were also measured. Thus, Po can be cacluted by $Po = \frac{m3-m1}{m3-m2}$. Then the relative density (RD) in this work is from the equation of $RD = 1 - \frac{Vr}{Vs}$ (Vs is volume calculated from size.), and the close porosity (Pc) can be from $Pc = \frac{Vr}{Vs} - Po$. In addition, desnsity was also calculated from geometry.

References

[1] Hiroshi Ichikawa, Recent Advances in Nicalon Ceramic Fibres, Ann. Chim. Sci. Mat. 25 (2000) 523–528.

[2] S.J. Zinkle, N.M. Ghoniem, Operating temperature windows for fusion reactor structural materials, Fusion Eng. Des. 51–52 (2000) 55–71. https://doi.org/10.1016/S0920-3796(00)00320-3.

[3] L.L. Snead, T. Nozawa, Y. Katoh, T.S. Byun, S. Kondo, D.A. Petti, Handbook of SiC properties for fuel performance modeling, J. Nucl. Mater. 371 (2007) 329–377. https://doi.org/10.1016/j.jnucmat.2007.05.016.

[4] T. Hinoki, Y. Katoh, A. Kohyama, Effect of fiber properties on neutron irradiated SiC/SiC composites, Mater. Trans. 43 (2002) 617–621. https://doi.org/10.2320/matertrans.43.617.

Chapter 3 Effect of sintering temperature on properties of SiC fiber reinforced W composites

3.1 Introduction

In this work, a new way is provided for designing the structural materials in fusion nuclear systems. The SiC fiber was considered as reinforcement to W because SiC exhibits excellent properties. It has been reported that SiC material with high crystallinity exhibits very excellent properties under neutron irradiation environment and does not cause strength deterioration [1]. Furthermore, the coefficients of thermal expansion of W and ceramic fibers are very close to each other, so the generated stress at the interface by thermal load should be limited. Umer et al. [2] synthesized SiC particles reinforced W and found that the flexural strength decreased with the increment of SiC content, while the ablation resistance improved because the layer of SiO_2 appeared on the surface of ablated samples to prevent the formation of WO_3. Shi et al. [3] reported the strength of 0.8 wt% discontinuous SiC fiber reinforced W–20Cu composites had 1200 MPa by 3-point bending method and thermal conductivity was 235 W/(m·K). Nevertheless, both works did not focus on toughness and did not illustrate the strain-stress curve in the papers, and no works focused on the continuous SiCf/W system. Thus, discussing the fracture behavior and thermal properties of continuous SiC fiber reinforced W composites is necessary to give more selections for diverter application. In order to confirm the most suitable sintering temperature to balance the reactions and the relative density when fabricate the SiC fiber reinforced W composites, the composites were sintered from 1500 to 1900 °C. In this work, unidirectional SiC fibers as reinforcement were used to fabricate W based composites by hot-press to widen the operating temperature of W limited by high DBTT and recrystallization behavior, and to maintain toughness after irradiation under neutron irradiation or plasma exposure. Then the mechanical property was examined by tensile test at RT to evaluate whether the SiC fiber can enhance the ductility of W. The density, microstructure and reactions in the sintering process were also discussed, as well as the kinetics between SiC and W.

3.2 Density and porosity

The results of density by size and densitometer are given in Table 3.1. The fiber volume fraction displayed here was calculated by weight and density (3.1 g/cm^3). The results show that the densification happened when sintering temperature was increased from 1500 °C to 1900 °C. In addition, the values of density by these two methods differ greatly, which caused from high

open porosity. However, the density by size including open and closed pores is more reasonable for a bulk material.

Table 3.1 Density and porosity of sintered composites.

Sintering Temperature / ° C	1500	1600	1700	1800
Vf%	53.16	52.93	50.75	51.92
ρs / g/cm^3	9.01	9.14	10.43	11.46
ρa / g/cm^3	10.75	10.19	11.75	11.70

Note: Vf is fiber volume ratio; ρs is density calculated by geometric method; ρa is density measured by Archimedes method using helium gas.

3.2 Phase changes and microstructure after sintering

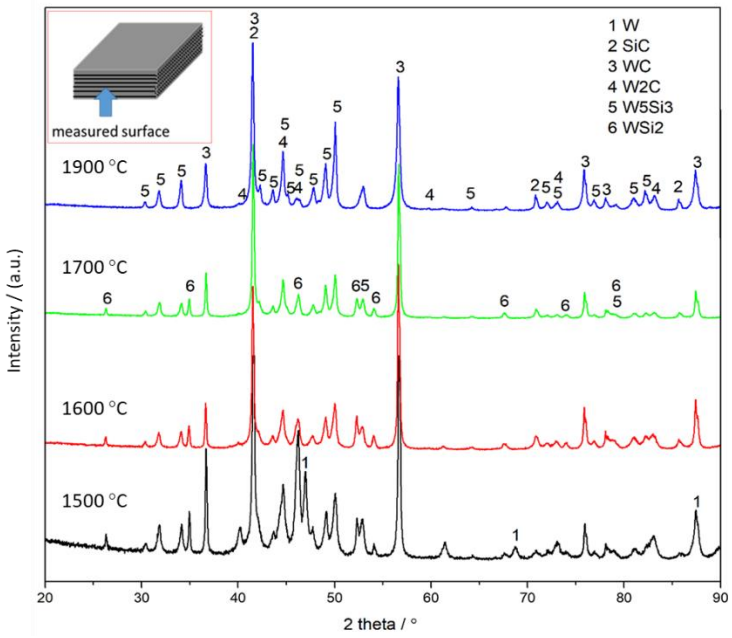

Figure 3.2 XRD patterns of composites fabricated at different temperatures.

Fig. 3.2 reveals the XRD patterns of fabricated composites, implying the effect of sintering temperature on interfacial reaction. Besides, the schematic diagram of the measured surface is also exhibited in the inset of the XRD pattern image, in which the tested surface is parallel to the direction of fiber. Phase compositions of composites changed a lot as a result of reactions between W and SiC. Two different tungsten carbides (W_2C and WC) and two different tungsten silicide phases (W_5Si_3 and WSi_2) were identified after sintering, which is different from the work of SiC powder reinforced W prepared by the SPS method. There is only W_2C and W_5Si_3 found after

sintering at 1700 °C [2]. In this work, the peak of W can only be identified at 1500 °C prepared samples because of the small grain size of raw W powder and SiC fiber as well as the relatively large surface of small diameter fiber, bringing about the severe diffusion of Si or C atom, which suggests that the reaction rate enhance a lot by increasing the sintering temperature from 1500 °C to 1900 °C. Another phenomenon is the peak of WC and W_5Si_3 becoming stronger with the sintering temperature enhancement because W_2C and WSi_2 transferred to WC and W_5Si_3 [4]. While in previous papers, W_2C always acts as a more stable phase in the W-Si-C ternary system [5–7].

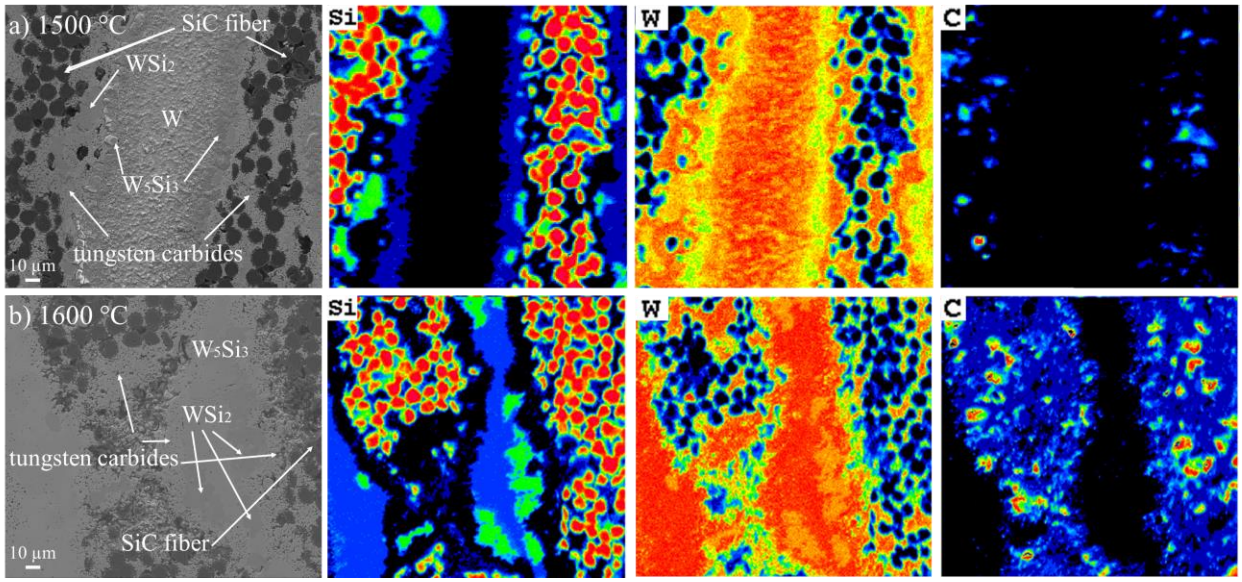

Figure 3.3 SEM images (secondary electron mode) and element analysis by EPMA mapping of composites fabricated at different temperatures. a) 1500 °C; b) 1600 °C.

Fig. 3.3 exhibits the secondary electron (SE) images and the elements' distribution measured by EPMA of composites fabricated at 1500 °C and 1600 °C. Tungsten carbides located near the SiC part, and a gap of Si distribution in matrix can be found in the EPMA results, and a similar phenomenon was observed in the paper [5], indicating that W is easier to react with Si, rather than C. Moreover, in both kinds of composites, the Si and C atoms diffused to the W region because of their smaller atomic radius than the size of W atom, in which, the region of Si atom diffused is larger than the length of C from image b), suggesting that the reaction rate between Si and W is higher than that of W and C. Moreover, Si atoms have already diffused the whole matrix in composites fabricated above 1500 °C, due to the small grain size of W as raw material, and no

W remained according to the results of EPMA (see Fig 3.3. b)) and XRD. Besides, because the reaction rate increased with temperature according to XRD, therefore the generated phases (tungsten silicides and tungsten carbides) are not appropriate as diffusion barriers in the SiC/W system, which also can be found in the microstructure images of composites.

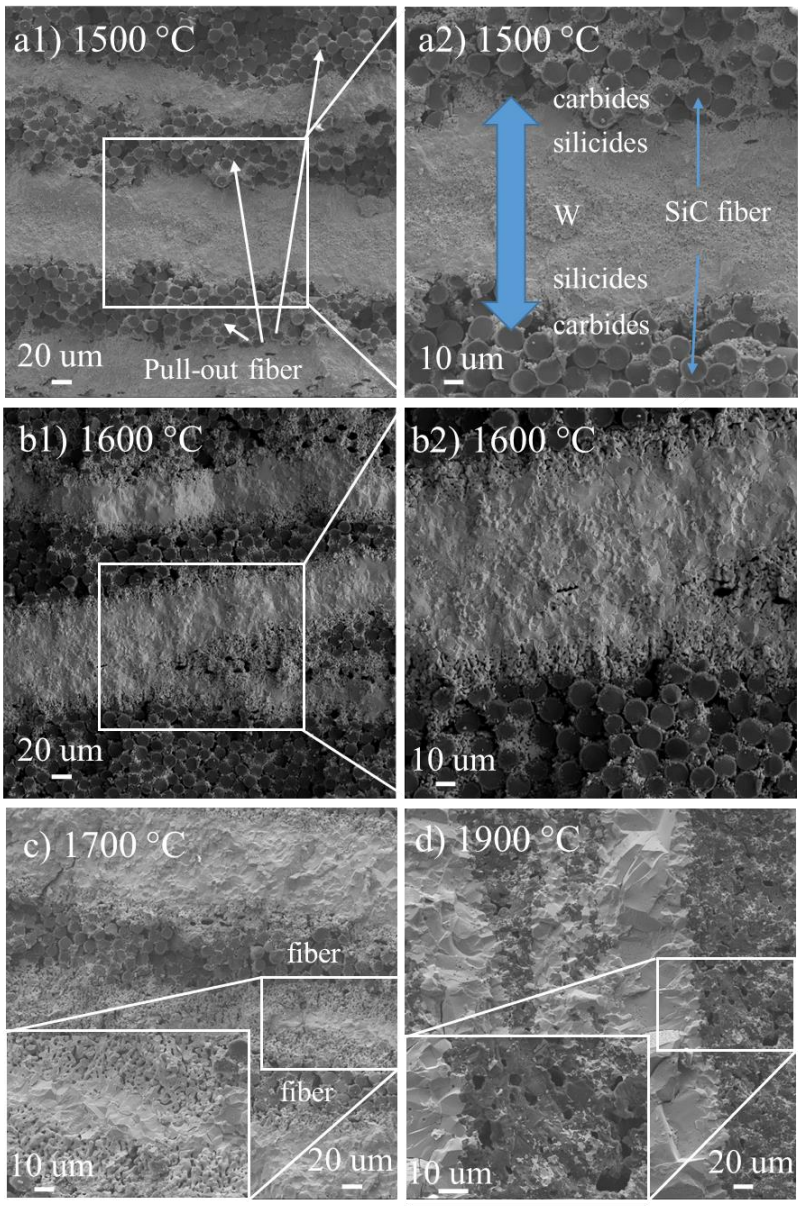

Figure 3.4 SEM images in SE (secondary electron) mode of cross-section of SiC fiber reinforced W composites. a1), a2) and b1), b2) are the images of composite fabricated at 1500 °C and 1600 °C with different magnification. c) is the image of composite sintered at 1700 °C. d) is the image of composite prepared at 1900 °C.

The morphologies of the cross-section images with different magnifications of SiCf/W composites sintered from 1500 °C to 1900 °C after tensile tests examined by SEM in SE mode are shown in Fig. 3.4. Short pull-out fiber can be observed in composites except 1900 °C sintered composites. For both composites, tiny pores in matrix near fiber tow region can be observed in W powders synthesized from 1500 °C to 1700 °C, and pores also can be found in the middle matrix part in 1500 °C prepared composite. These are unsintered regions caused by W and carbides with the higher melting point than silicides, combined with the EPMA results. Besides, five layers, namely carbides/silicides/W/silicides/carbides, can be observed at matrix in composites sintered at 1500 °C. In comparison, W layer disappeared, and 3 layers (carbides/silicdes/carbides) remained from 1600 °C. Thus, the pores at the fiber edge region is caused by the existence of carbides with high melting point, which caused the weak interface between fiber and matrix. Thereby, fiber pull out effect can be viewed. Furthermore, in the composite sintered 1900 °C, the matrix region is totally dense except for the slurry undispersed region, and fiber damaged completely. Thus, 1900 °C is too high to sinter SiC fiber reinforced W composite. Therefore, it is necessary to discover an effective interface as a diffusion barrier to impede the reaction at the high temperature.

3.3 Mechanical property

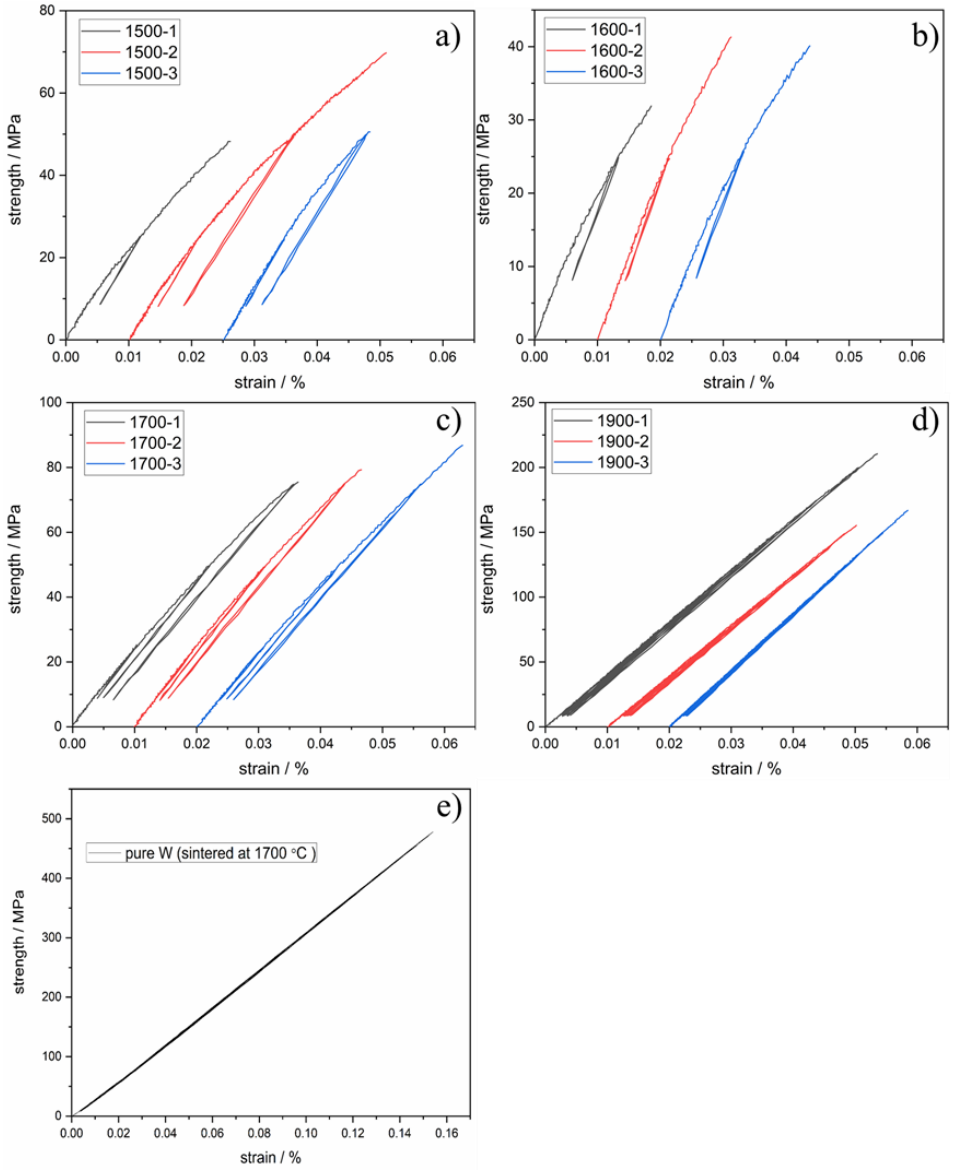

Figure 3.5 Results of tensile tests of SiCf/W composites and pure W. Images a) to d) show the strain-stress curve of composites sintered from 1500 °C to 1900 °C respectively; Image e) shows tensile test result of pure W sintered at 1700 °C. (Please note here, the strain for every bar should start from 0, and the curves were separated in order to show them clearly, same as the other tensile test results.)

Fig. 3.5 reveals the variation of tensile strength at RT of SiCf/W composites fabricated at the different sintering temperatures, in which tensile test data of pure W annealed at 1700 °C is

also shown for comparison. The load direction was the same as the fiber direction. Furthermore, it can be found that composites sintered at 1500 °C to 1700 °C exhibited pseudo ductility, compared with pure W annealed at 1700 °C (see Fig. 3.5 e)), although the tensile tests were carried out at RT, which is lower than the DBTT of W.

Furthermore, the tendency of pseudo ductility reduced with increasing the sintering temperature, and almost no pseudo-ductile behavior can be found in 1900 °C sintered samples from the stress-strain curve because of significant reaction between fiber and matrix. Because relatively low sintering temperature can decrease the reaction rate between SiC fiber and W, more unreacted fibers remained after sintering, which contributed for the higher ductility. In addition, strength increases with the enhancement of temperature. The average UTS of UD composites sintered at 1900 °C was about 178 MPa, which is almost three times higher than 56 MPa of UD1500 composites. In addition, the average UTS of composites prepared at 1600 °C and 1700 °C are 37.8 MPa and 82.9 MPa, respectively. Compared with pure W, the composites showed relatively lower UTS but more apparent pseudo ductility. It is unnecessary to consider the DBTT for fiber reinforced composites because brittleness of W isn't matter.

3.4 Thermal property

Effect of sintering temperature on thermal conductivity was characterized. Thermal conductivity (λ) of composites measured in two different directions at RT, which is thermal load vertical (through-plane, also named X direction) and parallel (through-plane, also named Y direction) to the fiber direction, respectively, was shown in Fig. 3.6. Furthermore, the geometric density with open and closed pores was used to calculate λ because of the big difference compared with the value measured by the helium pycnometer (see Tab. 1). The results show the λ increased with sintering temperature caused by densification. Moreover, it is substantial to be found that the value of λ is higher in the in-plane direction (red points) compared to the through-plane direction (black points). Because thermal conductivity of X direction is determined by mixture of W layer and SiC fiber layer with pores, while it is determined by the highest thermal conductivity layer at Y direction. The thermal conductivity of 1700 °C fabricated composite in in-plane direction showed the best result of 51.5 W/(m·K) at RT, whereas the value was 32.2 W/(m·K) in the through-plane direction. However, even the highest thermal conductivity of SiCf/W composites is still

lower than the thermal conductivity of pure W of 170 W/(m·K) [8] and W-K alloy of 160 W/(m·K) [9] as well as K doped W-3wt%Re alloy of 110 W/(m·K) [10], while similar with W-10wt%Re alloy of 60 W/(m·K) and higher than W-25wt%Re alloy of 25 W/(m·K) [11]. Because the reaction products display the low conductivity compared to W and SiC, another reason is the low relative density even for 1700 °C sintered sample.

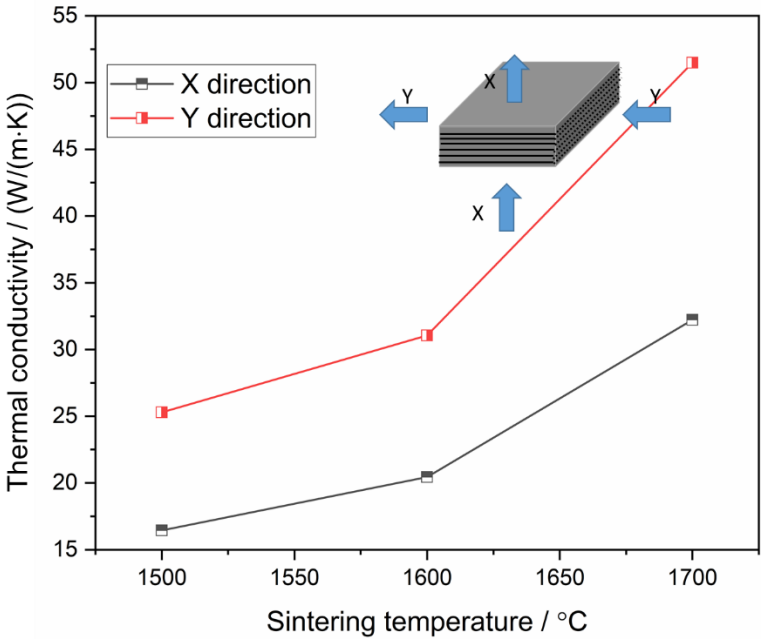

Figure 3.6 Thermal conductivity of SiCf/W composites fabricated at 1500 °C to 1700 °C in different directions (X direction, through-plane direction; Y direction, in-plane direction) measured at 25 °C.

3.5 Discussion

Table 3.2 summarizes the mechanical and thermal properties of synthesized composites. The reaction between SiC fiber and W matrix depended on sintering temperature. Only limited reactions happened in relatively lower sintering temperature (1500 °C), although more than half of W was reacted. For mechanical property, the decreasement of UTS from 1500 °C to 1600 °C is from the reduction of high strength W ratio even with higher densification. Therefore, reactivity has more contribution for UTS. Sufficient reactions between SiC and W were observed above 1600 °C. The strength increased with sinterability above 1600 °C. In addition, for composite sintered at lower temperature, short pull-out fiber can be observed. Moreover, pores at the fiber

bundle and the fiber edge caused the weak interface between fibers and matrix, so the laminate effect is also responsible for the pseudo-ductility. However, densification lead to the strong interface between fiber and matrix, causing that the laminate effect reduced with increasing the sintering temperature. Therefore, pseudo ductile behavior was limited with the sintering temperature so that no pseudo-ductility exists in composite fabricated at 1900 °C with the highest density and the most severe reaction. So, densification has a greater impact on the pseudo-ductility. While for the thermal conductivity, 1500 °C sintered composite shows the lowest thermal conductivity even if W with high thermal conductivity exists in the matrix due to low sinterability, and it increases with the sintering temperature. The ρa in the table 1 was calculated without open pores. A lot of open pores existed in the material sintered at 1500 °C. Therefore, sinterability dominates the thermal conductivity compared with reactivity. Thus, there is a tradeoff. Relatively high temperature sintering improves densification, strength and thermal conductivity, however high temperature caused severer damage in fiber and matrix. So the densification of composites and reaction between fiber and matrix need to be balanced. 1700 °C should be suitable temperature to fabricate SiC/W composites by hot press, which displayed pseudo ductile behavior with relative high UTS, as well as high thermal conductivity, however, the composition of matrix has been reacted totally, and no W remained. Based on this, to raise the pseudo-ductility and thermal conductivity of the composites, it is essential to prepare diffusion barrier to avert the reaction to remain higher content of W and keep the shape of SiC in composites after sintering.

Table 3.2 Summary of the fabricated composites' properties.

Sintering temperature/°C	Density / g/cm^3	Reaction at interface	Mechanical property		Thermal conductivity/(RT)	
			Pseudo ductility	Average UTS/MPa	X direction	Y direction
1500	9.01	very severe	yes	56.17	16.45	25.29
1600	9.14	totally changed	yes	37.76	20.45	31.06
1700	10.43	totally changed	yes	82.87	32.23	51.48
1900	11.46	totally changed	no	178.2	---	---

3.6 Conclusion

SiC fiber reinforced W composites were fabricated at different sintering temperature by hot-pressing successfully. The strength and thermal conductivity of composites increased with increment of sintering temperature due to densification, however pseudo ductility was reduced due to enhanced reaction between SiC fiber and W matrix. In addition, the stress-strain curves displayed obvious pseudo-ductile behavior for specimen sintered at 1500 °C, 1600 °C and 1700 °C compared with pure W annealed at 1700 °C even if the temperature of tensile test is lower than the DBTT of W. So SiC fiber as reinforcement to strengthen W is feasible. Concerning thermal conductivity, higher sintering temperature leaded to higher thermal conductivity. In addition, it is much higher in through-plane direction than in-plane direction. The composites fabricated at 1700 °C showed the largest strength with pseud ductility. Besides, the reaction rate increased approximately 18 times when temperature increased from 1500 °C to 1700 °C. Thus, to acquire better properties, it is necessary to recognize an effective diffusion barrier for the W and SiC system without reactions to get higher W content and protect SiC fiber.

References

[1] T. Koyanagi, K. Ozawa, T. Hinoki, K. Shimoda, Y. Katoh, Effects of neutron irradiation on mechanical properties of silicon carbide composites fabricated by nano-infiltration and transient eutectic-phase process, J. Nucl. Mater. 448 (2014) 478–486. https://doi.org/10.1016/j.jnucmat.2013.10.005.

[2] M.A. Umer, D. Lee, O.A. Waseem, H.J. Ryu, S.H. Hong, Fabrication of protective-coated SiC reinforced tungsten matrix composites with reduced reaction phases by spark plasma sintering, Met. Mater. Int. 22 (2016) 493–500. https://doi.org/10.1007/s12540-016-5700-y.

[3] X. Shi, M. Wang, S. Zhang, Q. Zhang, Fabrication and properties of W-20Cu alloy reinforced by titanium nitride coated SiC fibers, Int. J. Refract. Met. Hard Mater. 41 (2013) 60–65. https://doi.org/10.1016/j.ijrmhm.2013.02.002.

[4] S. Coşkun, M.L. Öveçoğlu, B. Özkal, M. Tanoğlu, Characterization investigations during mechanical alloying and sintering of W-20 vol% SiC composites, J. Alloys Compd. 492 (2010) 576–584. https://doi.org/10.1016/j.jallcom.2009.11.185.

[5] S.J. Son, K.H. Park, Y. Katoh, A. Kohyama, Interfacial reactions and mechanical properties of W-SiC in-situ joints for plasma facing components, J. Nucl. Mater. 329–333 (2004) 1549–1552. https://doi.org/10.1016/j.jnucmat.2004.04.285.

[6] F. Goesmann, R. Schmid-Fetzer, Stability of W as electrical contact on 6HSiC: phase relations and interface reactions in the ternary system WSiC, Mater. Sci. Eng. B. 34 (1995) 224–231. https://doi.org/10.1016/0921-5107(95)01311-3.

[7] W.F. Seng, P.A. Barnes, Calculations of cobalt suicide and carbide formation on SiC using the Gibbs free energy, Mater. Sci. Eng. B Solid-State Mater. Adv. Technol. 76 (2000) 225–231. https://doi.org/10.1016/S0921-5107(00)00457-8.

[8] S. Nogami, W. Guan, A. Hasegawa, M. Fukuda, Feasibility of utilizing tungsten rod for fusion reactor divertor, Fusion Sci. Technol. 72 (2017) 673–679. https://doi.org/10.1080/15361055.2017.1347463.

[9] B. Huang, L. Chen, W. Qiu, X. Yang, K. Shi, Y. Lian, X. Liu, J. Tang, Correlation between the microstructure, mechanical/thermal properties, and thermal shock resistance of K-doped tungsten alloys, J. Nucl. Mater. 520 (2019) 6–18. https://doi.org/10.1016/j.jnucmat.2019.03.056.

[10] M. Fukuda, A. Hasegawa, S. Nogami, Thermal properties of pure tungsten and its alloys for fusion applications, Fusion Eng. Des. 132 (2018) 1–6. https://doi.org/10.1016/j.fusengdes.2018.04.117.

[11] T. Tanabe, C. Eamchotchawalit, C. Busabok, S. Taweethavorn, M. Fujitsuka, T. Shikama, Temperature dependence of thermal conductivity in W and W-Re alloys from 300 to 1000 K, Mater. Lett. 57 (2003) 2950–2953. https://doi.org/10.1016/S0167-577X(02)01403-9.

Chapter 4 Effect of matrix on properties of SiC fiber reinforced composites

4.1 Introduction

The significant reactions were identified between W powder and SiC fiber from Chapter 3, generating tungsten silicides (W_5Si_3 and WSi_2 (47 $W/m^{-1}/K^{-1}$ [1])) and tungsten carbides (WC (63 $W/m^{-1}/K^{-1}$ [2]) and W_2C), lower than the thermal conductivity of SiC and W. Therefore, we consider using dense W foil (0.05 mm and 0.08 mm thick foil) as matrix to reduce the reaction and improve the strength of composites. While W foil displays ductile behavior, W foil will lose ductility due to recrystallization behavior at high temperature[3,4]. Therefore, the recrystallization temperature of W foils used in this work was examined by annealing in the temperature range of 600 °C to 1200 °C for 1 h (every 200 °C) in order to verify the recrystallized temperature of used foils to confirm the ductility from foil or fiber. Moreover, the variation of property of foils like residual stress and hardness were also analyzed in this work. In addition, molybdenum (Mo) is the same group element as W with BCC structure, encountering the identical issue which is lack of ductility at RT [5]. Therefore, the SiC fiber reinforced Mo composite with foils was also tried to fabricate by same method at 1500 °C with 20 MPa pressure for 1h due to lower melting point of 2623 °C than W. In addition, the recrystallizational behavior of Mo foil was also examined in this work. Then, the mechanical property of prepared composites with different matrix reinforced by unidirectional SiC fiber was evaluated by tensile test measured at RT and 1000 °C, and also phase changes during fabrication were investigated.

4.2 The recrystallization behavior of foil at high temperature

4.2.1 Recrystallization temperature of metal foils used in this work

Fig. 4.1 displays W's recrystallization behavior, in which 0.08 mm foils were annealed at elevated temperatures for 1 h from 600 °C to 1200 °C for every 200 °C, etched by plasma using CF_4 and O_2 mixture gas with the ratio of 90% and 10% before observing [6]. Furthermore, the SEM images of the foil in 1500 °C fabricated composite with 0.08 mm foil is shown in Fig. 4.1 f), in which the reaction between SiC fibers and W foil is limited. It can be found that the W grains have no noticeable change below 800 °C, while they start recovery from 1000 °C. In addition, a typical triple junction can be found in 1500 °C heat treatment W foil, indicating that the grains

have completely recrystallized at 1500 °C. Therefore, we think both foils in composites have recrystallized even after 1700 °C sintering.

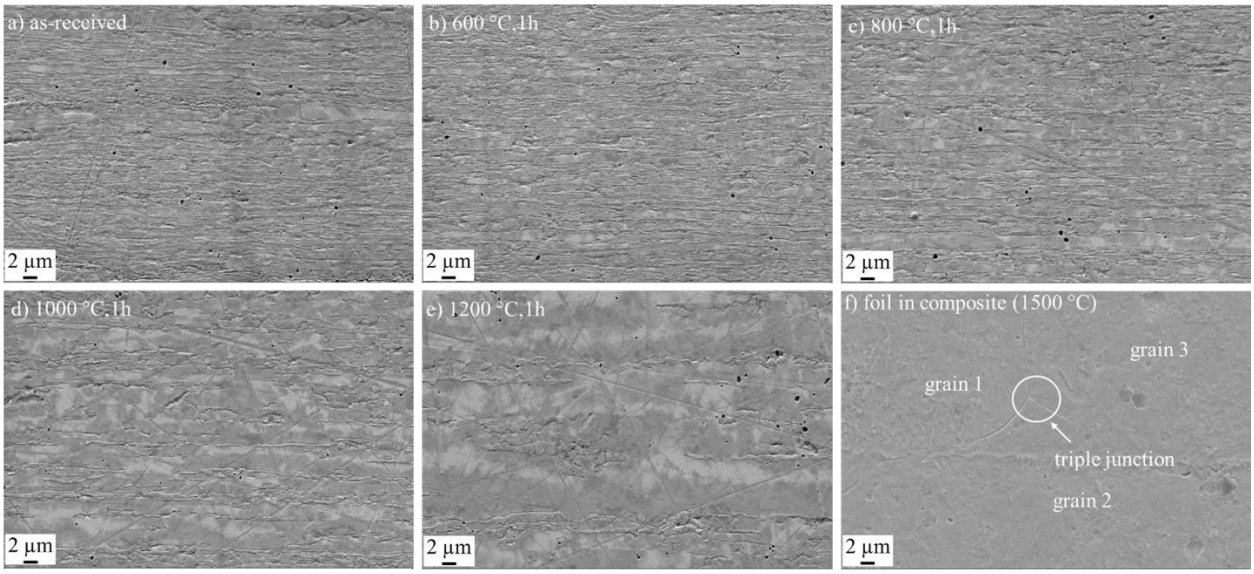

Figure 4.1 SEM images of microstructural changes of 0.08 mm W foils annealed at different temperatures. a) as-received W foil; b) 600 °C, 1h; c) 800 °C, 1h; d) 1000 °C, 1h; e) 1200 °C, 1h; f) 0.08 mm W foil in composite (1500 °C).

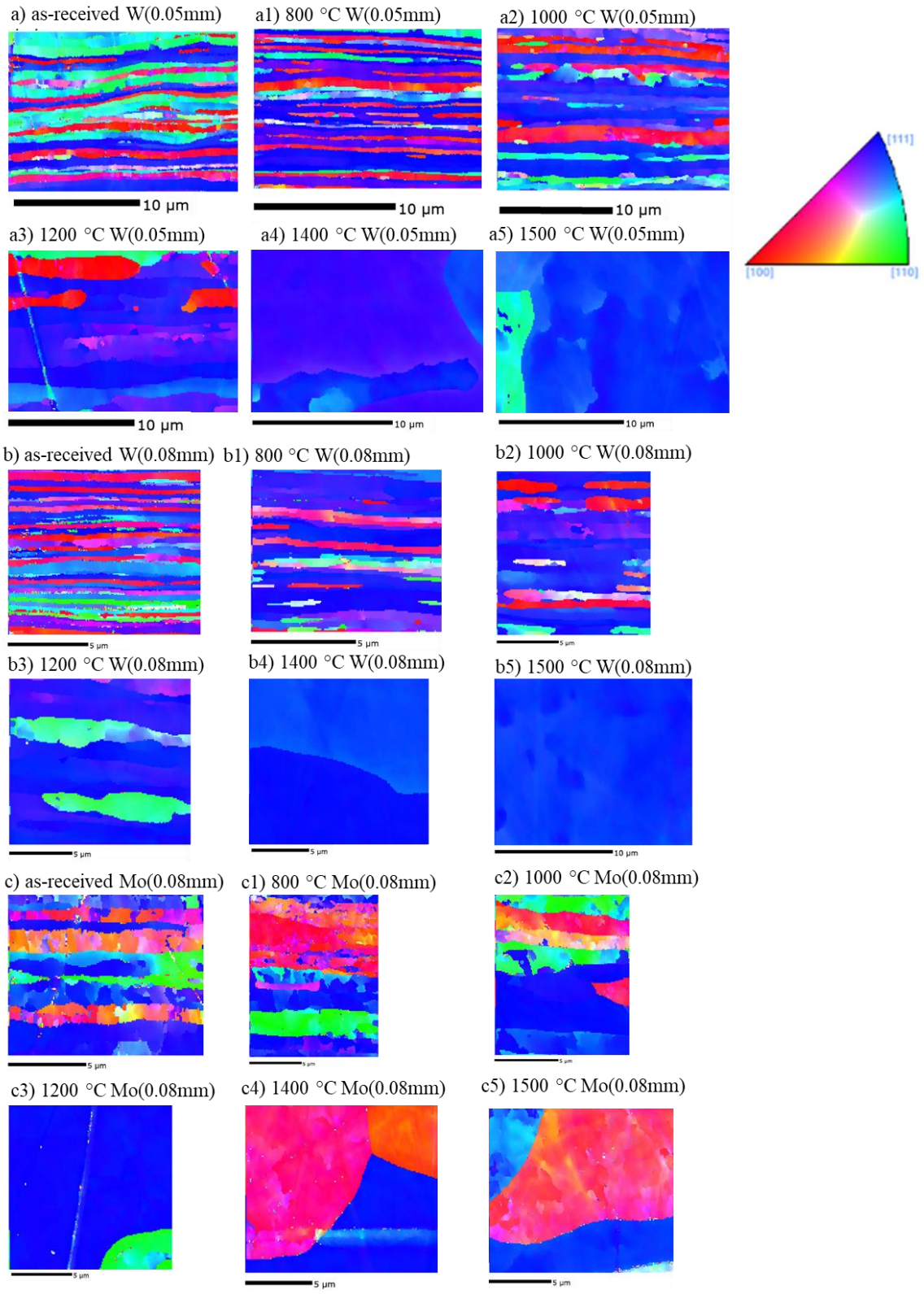

Figure 4.2 The EBSD results of as-received and annealed W and Mo foils as-received and annealed at different temperatures. a) is as-received 0.05 mm W foil; a1) to a5) are 0.05 mm W foil annealed

at different temperatures; b) is as-received 0.08 mm thick W foil; b1) to b5) are 0.08 mm W foil annealed at different temperatures; c) is as-received 0.08 mm Mo foil; c1) to c5) are the 0.08 mm Mo foil annealed at different temperatures.

EBSD measurement was also used to evaluate the recrystallized temperature, and the results of W foils with different thickness (0.05 mm and 0.08 mm) and Mo foils of 0.08mm thickness annealed at different temperatures were shown in Fig. 4.2. For W foils with different thicknesses of 0.08 mm and 0.05 mm, similar results can be noticed, which is the recrystallization behavior occurred between 1200 °C and 1400 °C and only grain growth developed at lower 1200 °C. In addition, the thickness of foils after hot rolling has no effect on recrystallized temperature. However, the recovery temperature is slightly higher than the value reported in K-doped W and K-doped W-Re materials [7]; however, both rolled W recrystallized completely as well after 1500 °C, 1h annealing [7], causing the significant variation of properties like reducing the Vickers hardness [7] and increasing the DBTT [8]. Therefore, composition has a great impact on recrystallization behavior. In addition, the recrystallized temperature of Mo foil is lower than that of W, which is between 1000 °C and 1200 °C. At 1200 °C, Mo grains have already recrystallized totally.

4.2.2 Property changes of metal foils before and after recrystallization

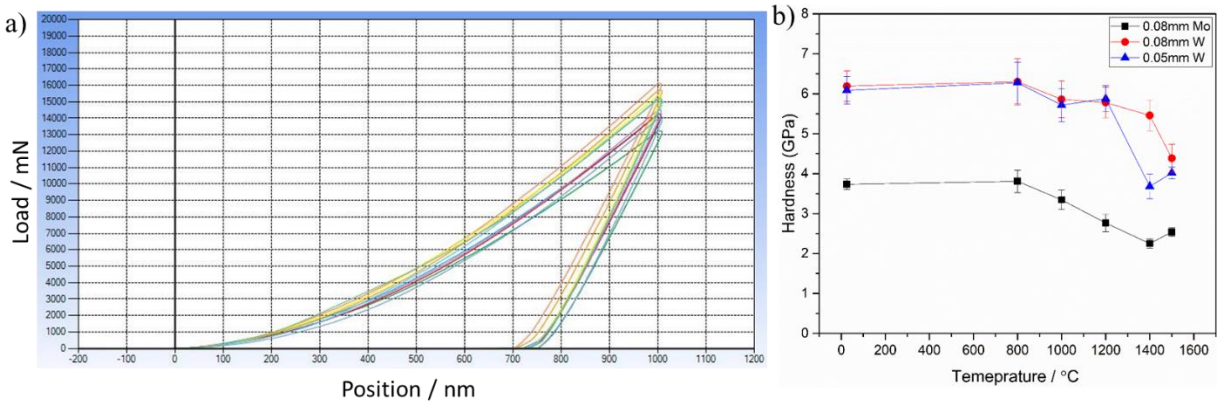

Figure 4.3 Dependence of hardness of metal foils on the temperature of annealing. a) the relationship between load and depth by nanoindentation; b) the hardness variation of foils after high temperature treatment.

Fig. 4.3 shows the alternative of nanoindentation hardness of W and Mo foils used in this work with the annealing temperature. The Berkovich tip indenter was used in this work. In addition, the highest depth was set as 1000 nm. With the increase of temperature, the hardness of foils gradually decreased. Moreover, the received rolled W have same hardness with unrelated its thickness about 6.1 $\pm$ 0.3 GPa for 0.05 mm W foil and 6.1 $\pm$ 0.4 GPa. In addition, the hardness of Mo foil is 3.7 $\pm$ 0.1 GPa at RT. This reduce of hardness is considered to be recovery caused by the release of residual stress and the disappearance of dislocation and grain boundary. The improvement of hardness at high temperature may cause from the inaccuracy of measurement. At higher temperature the grain growth takes place after recrystallization, therefore, the hardness should decrease slightly.

The differences of residual stress of all foils before and after heat treatment were evaluated by CrossCourt4 (CC4) software based on Kikuchi patterns from EBSD results. The stress distribution in 3 directions of as-received and annealed at 1500 °C foils were shown in Fig. 4.4, in which the "-" means compressive stress. According to the results, the stress scattered only in 2 directions, and no stress was detected from x_3 direction. Because electrons in SEM have limited ability to penetrate the sample, EBSD can only detect the surface stress of the sample. Therefore, this surface stress distribution from CC4 on the basis of EBSD can be regarded as a two-dimensional stress state, and its stress $\sigma 33 \approx 0$ perpendicular to the sample, while the principal strain $\varepsilon 3$ in this direction is not 0.

It is easy to be found that the stress relief caused from the recrystallization and grain growth in all foils. The stress of 0.05mm W foil without annealing in $\sigma 11$ and $\sigma 22$ is within the range of 100 GPa to -100 GPa, but data reduced to 30 GPa after heat treatment at 1500 °C. For the 0.08 mm thick foil, the residual stress decreased from the range between 100 GPa and -70 GPa to $\pm$ 20 GPa. However, it is difficult to say the effect of thickness on the residual stress just based on the results from CC4, and more detail and accurate data are required. Similar phenomenon occurred in Mo foil. The data is in the limit from 120 GPa to -60 GPa for non-annealed foil, while it's about $\pm$ 30 GPa in 1500 °C annealed foil.

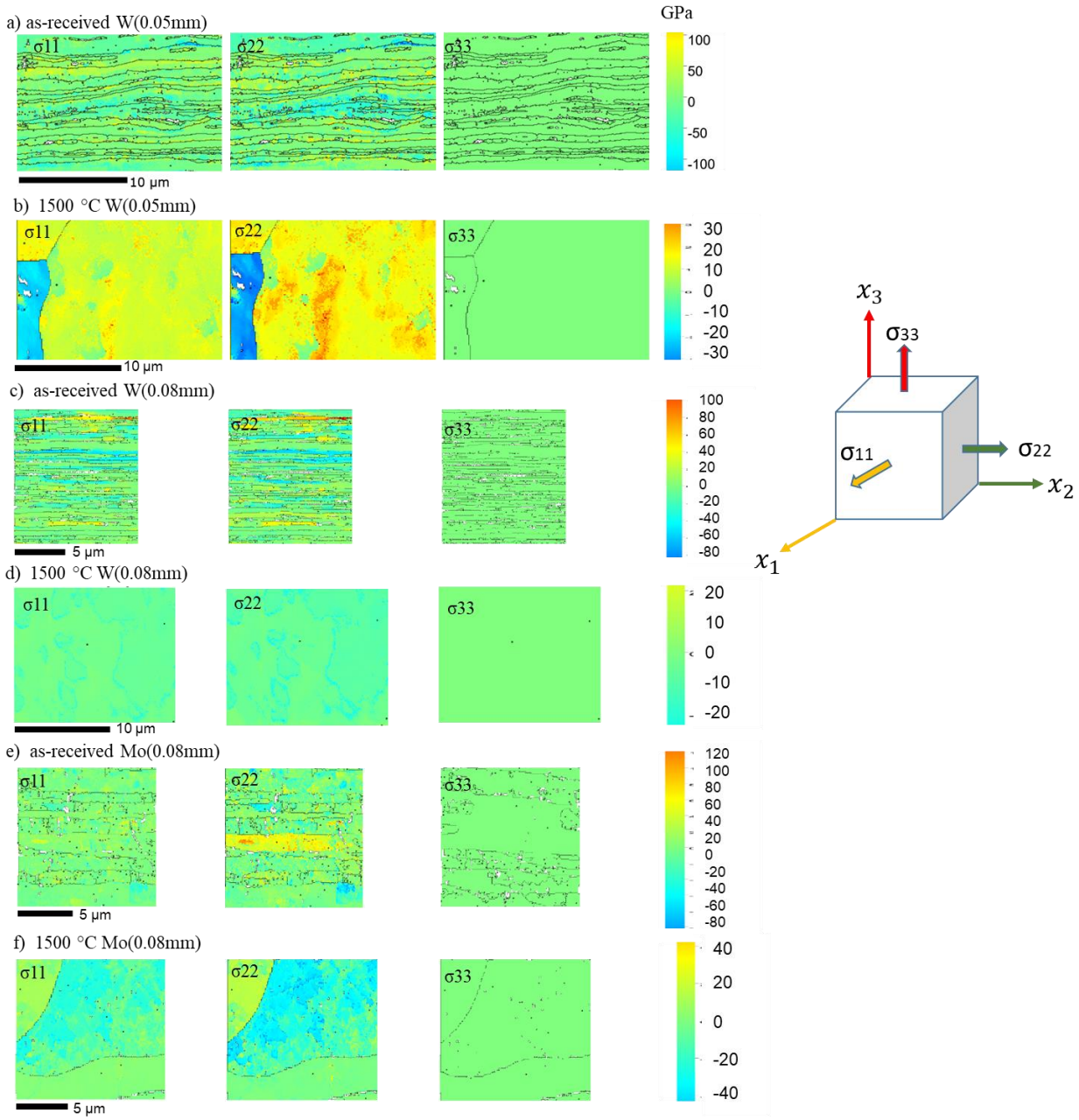

Figure 4.4 The residual stress from three directions of as-received and annealed foils at 1500 °C by crosscourt4. a) and b) are the stress of as-received and annealed 0.05 mm W foils; c) and d) are the stress of as-received and annealed 0.08 mm W foils; e) and f) are the stress of as-received and annealed 0.08 mm Mo foils.

4.3 Effect of W foil thickness on the microstructure and mechanical property of composites

4.3.1 Microstructure

Table 4.1 Density and porosity of sintered composites with W foils

composites	Vf/%	ρ_s / g/cm^3	ρr / g/cm^3	Po / %	Pc / %	R.D / %
composite0.05	46.68	10.49	11.68	10.15	2.92	86.93
composite0.08	43.39	11.06	12.44	11.09	1.09	87.81

Note: V_f is fiber volume ratio; ρ_s is density calculated by geometric method; ρr is density measured by Shimadzu AccuPyc II 1340; Po and Pc is open and closed porosity of composites; R.D is relative density of composite

Table 4.1 displays the density and porosity as well as other information of composites. Herein, 1500 °C 0.08 means the composite with 0.08 mm foil sintered at 1500 °C. The relative density is 86.93 % and 87.81 % for composite with 0.05 mm foils and 0.08 mm foils respectively, in which the low density is from high open porosity of approximately 10 % for both composites because the slurry do not disperse uniformly in the fiber bundle. Besides, the fiber volume fraction is about 43.4 % in 0.08 mm foils fabricated composites, lower than that of composites with 0.05 mm W foil of 46.7 %.

The XRD pattern of the fabricated composites is shown in Fig. 4.5, displaying the phases in the composites. Herein, it is clear to identify the W's peaks in both composites with two kinds of foils sintered at 1700 °C, although the stable reaction products of silicides (W_5Si_3 and WSi_2) and carbides (WC and W_2C) can be found. However, no W remained after sintering at 1700 °C for composite with powders as matrix, illustrating that dense foil can lessen the reaction rate between SiC and W. Besides, the intensity of W peaks in 0.08 mm foil fabricated composite is stronger than that of composites with 0.05 mm foil W and without foils fabricated at 1700 °C, indicating that more W remained in composite with 0.08 mm foil.

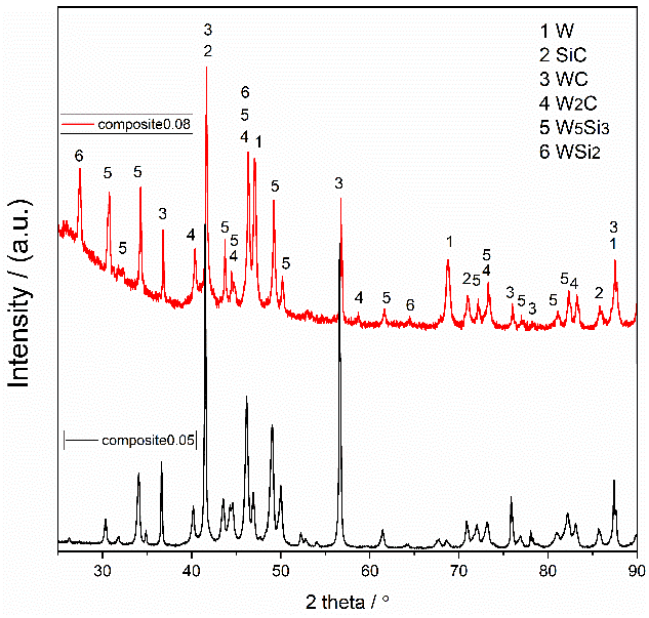

Figure 4.5. The XRD pattern of sintered composites with W foils of different thickness.

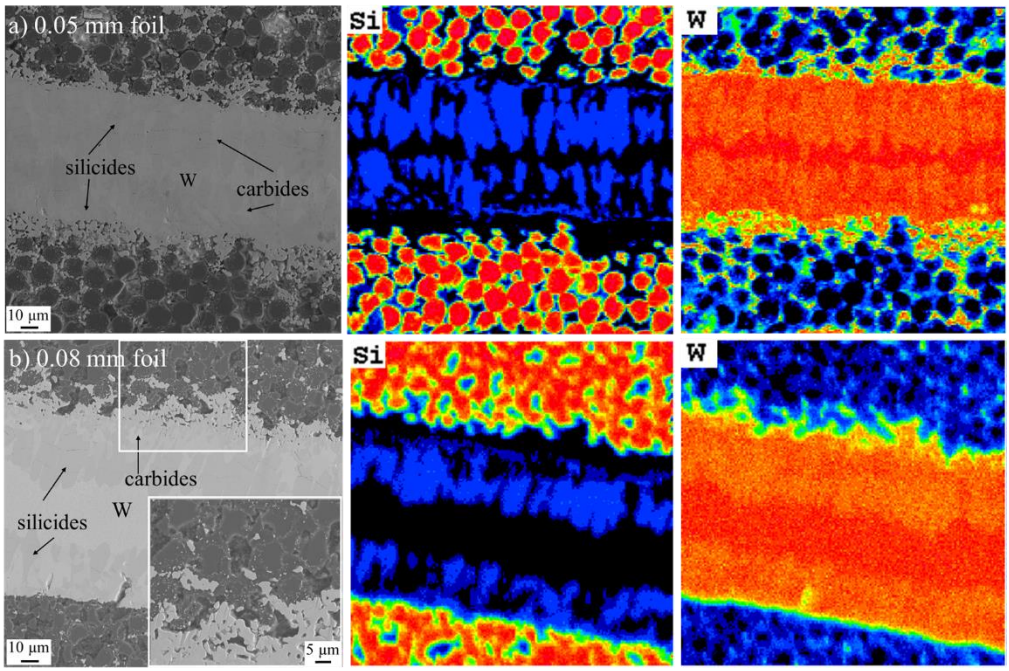

Figure 4.6 The cross-sectional SEM image and element analysis by EMPA of composite fabricated with different thicknesses of W foils. a) 0.05 mm foil; b) 0.08 mm foil.

The SEM images of the cross-section and element analysis by EPMA mapping of 1700 °C sintered composites with foils are exhibited in Fig. 4.6. It is easy to recognize the remained W and the damaged SiC fibers. In addition, the content of non-reacted W in composites with thicker foil

is more than that in composite with 0.05 mm foil, and approximately 10 μm W matrix remained in 0.05 mm foil, illustrating that dense matrix can decline the reaction rate. Besides, it is easy to observe columnar grains tungsten silicides in composites. Moreover, the diffusion path of Si and C atoms to W were much larger than the one of W into SiC caused by the difference of atoms' size. According to the reported results [9], the possible reactions between W and SiC during the sintering process up to 1700 °C are shown as follows, and such reactions leading to the degradation of fiber.

$SiC + 5/3\ W \rightarrow 1/3\ W_5Si_3 + C$

$SiC + 5/2\ W \rightarrow 1/2\ WSi_2 + W_2C$

$SiC + 3/2\ W \rightarrow 1/2\ WSi_2 + WC$

$SiC + 8/3\ W \rightarrow 1/3\ W_5Si_3 + WC$

$SiC + 8/3\ W_2C \rightarrow 1/3\ W_5Si_3 + 11/3WCSiC + 3/7\ W_5Si_3 \rightarrow 8/7\ WSi_2 + WC$

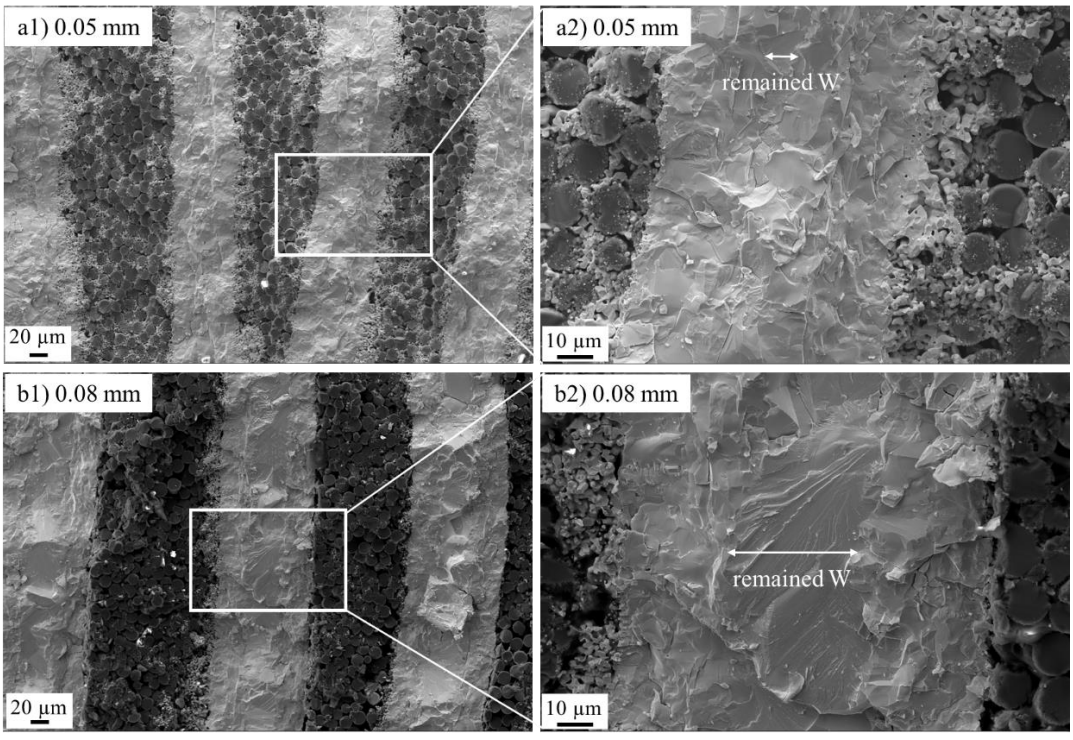

Figure 4.7 The cross-sectional SEM images of composites sintered at 1700 °C after tensile test measured at RT. a1) and a2) are composite fabricated with 0.05 mm-thick foils in various magnifications; b) composite with 0.08 mm-thick foils.

Fig. 4.7 reveals the SEM images in SE mode of the cross-section of fabricated composites containing W foils after tensile test at RT with different magnification. Very short pull-out fiber can be observed from these images in both composites. In addition, most grains in fracture surface show transgranular fracture at RT. Besides, it was also found that the SiC fibers were damaged after sintering at 1700 °C. Moreover, for both composites, small pores in matrix in W powders area near fiber tow can be observed, and these unsintered regions should be carbides because of the high melting point of tungsten carbides combined with the EPMA results.

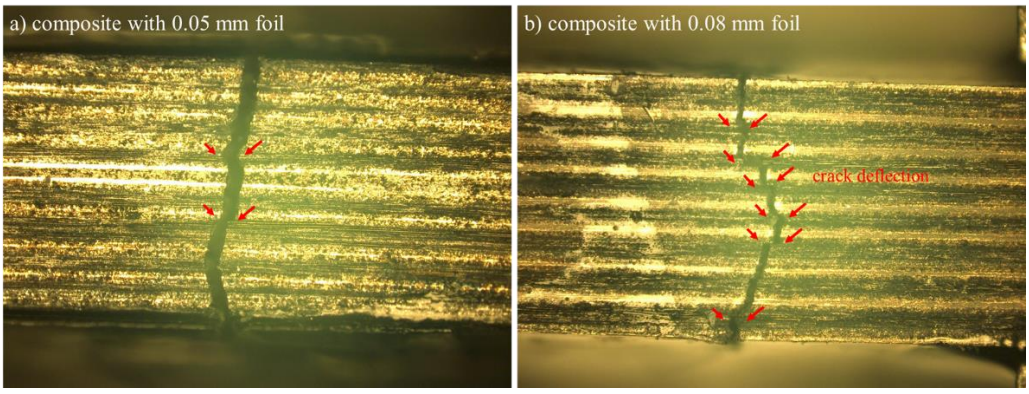

Figure 4.8 Optical image of the fracture surface side of composite with foils. a) 0.05 mm; b) 0.08 mm.

The optical photographs of the side of fracture surface of composite with foils are revealed in Fig. 4.8. It is easy to identify the short foil pull-out behavior from image b) due to weak bonding between SiC fiber and W matrix caused by the relatively open porosity, leading to crack deflection. In contrast, only limited crack deflection can be found in composite with 0.05 mm foils. Therefore, we think the pull-out effect from foil contributes to the pseudo ductility in this work.

4.3.2 Mechanical property at room temperature and 1000 °C

The tensile test results of SiCf/W composites with different thick foils tested at RT sintered at 1700 °C are illustrated in Fig. 4.9. The loading direction is parallel to the fiber direction and rolling direction of foil. It can be found that both composites with foils exhibited pseudo ductility tested at RT, although the temperature of tensile tests was room temperature, which is lower than the DBTT of W and the fabrication temperatures are higher than recrystallization temperature. However, the composite with thicker foils displayed a better mechanical property with the more

evident pseudo ductile behavior. The result is consistent with the optical images, in which more pull-out short can be found in composites with 0.08 mm. Furthermore, it maintains a high strength of 197 MPa, although it has a comparatively low fiber volume fraction. Besides, the strength is much higher than that of composite fabricated with 0.05 mm foil of 129 MPa. Thus, it can be assumed that the composite with 0.08 mm foils without reactions between fiber and foils should exhibit better UTS and pseudo ductility, in which fiber is responsible for ductility and the W matrix is for strength. However, the UTS of both composites are lower than that of pure W of 478 MPa at RT shown in Fig. 5.1, while no ductility can be found. In addition, we think both foils have no contribution to ductility because they have recrystallized after 1700 °C sintering (see Fig. 4.1 and 4.2), and it is reported that the recrystallized W has no ductility below 200 °C even though the as-received W displayed ductile behavior at RT [7]. Therefore, the pseudo ductility in this work is from the SiC fiber and pull-out foil (see Fig. 4.8), and considering that the lower volume fiber fraction in composites with thicker foil exhibit higher ductility, the contribution for the pseudo ductility from the pull-out effect is higher than SiC fiber itself.

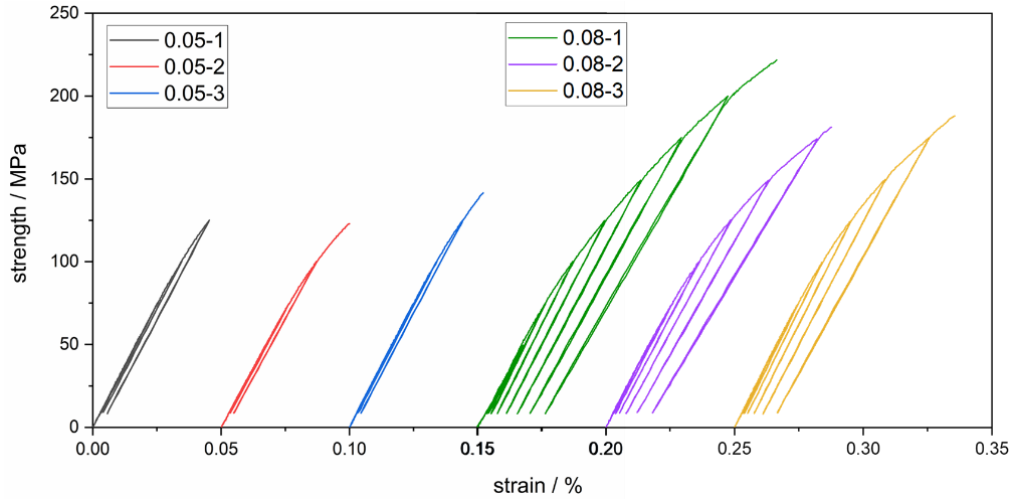

Figure 4.9 Tensile test results of fabricated composites with different thick foils measured at RT.

The composites were also fabricated at 1500 °C and 1600 °C with the same pressure and holding time with about 41.71 vol% and 44. 23 vol% SiC fiber respectively. The tensile test results measured at room temperature are revealed in Fig. 4.10. The composites delaminated easily according to the results marked by the arrows because composites don't sinter well. Therefore, 1500 °C and 1600 °C are low to sinter composites with 0.08 mm foil, consistent with the results

in Chapter 3 that 1700 °C is a recommendation temperature to sinter SiC/W composite by hot press.

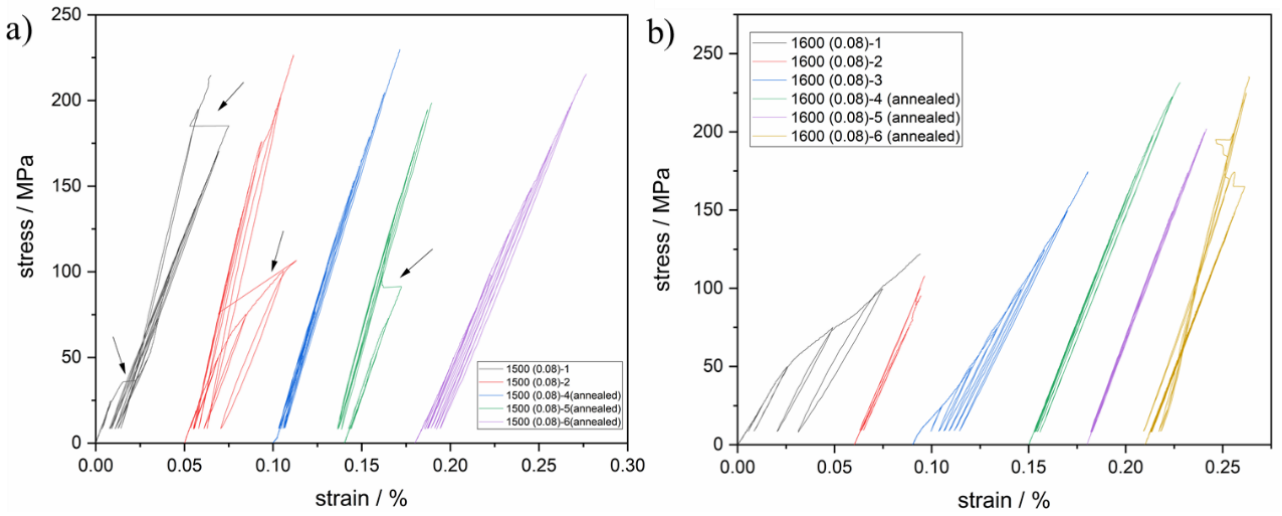

Figure 4.10 The tensile test results of SiCf/W composites sintered at 1500 °C and 1600 °C with 0.08 mm foil. a) 1500 °C; b) 1600 °C.

The pseudo ductility has already verified in the SiC fiber reinforced W composites with or without foils at room temperature. While, temperature also has a great influence on mechanical property, and whether the composites show better property than that of pure W at high temperature. Therefore, it is necessary to carry out the tensile test at higher temperature, and the main purpose is to understand the fracture behavior of the new material in a high temperature environment. The load position and stress strain curve of composites with 0.08 mm foil prepared at 1700 °C tested at 1000 °C are shown in Fig. 4.11. The loading speed for high temperature tensile test is 0.5 mm/s. The highest stress is 92.1 MPa lower than it measured at room temperature. The fracture of composites can be divided 4 steps based on the tensile test result. 1st step, the pseudo-ductile behavior can be noticed due to the composite effect, namely the weak interface between fiber and matrix. At high load region, there is still part delamination occurred. Then the SiC fiber fractured firstly due to brittleness, and the stress reduced to 20 MPa. However, the position was still moving to the downside. Subsequently, the remained W starts plastic deformation. Finally, the deformed W fractured.

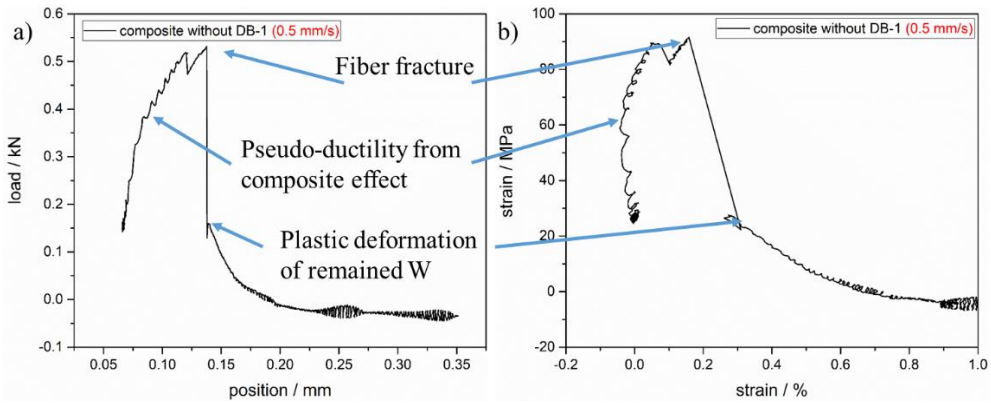

Figure 4.11 The tensile test result of SiCf/W composite with 0.08 mm foil sintered at 1700 °C without diffusion barrier. a) position load curve; b) stress strain curve.

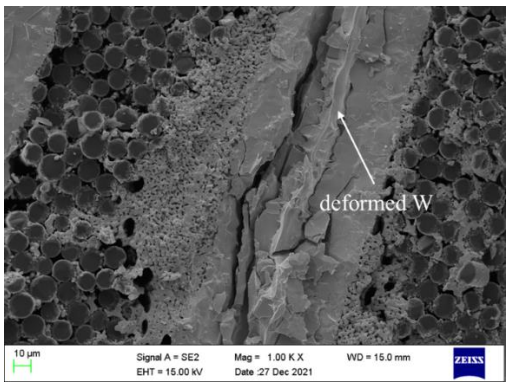

Figure 4.12 The cross-sectional SEM image of SiCf/W composites after 1000 °C tensile test.

The cross sectional SEM image of composite after high temperature tensile test was revealed in Fig. 4.12. The plastic deformed W region can be observed easily. In addition, the height in fiber area is lower compared with the W part. Therefore, SiC fiber fractured firstly and W broke at last from the SEM image matched with load position and stress strain curve.

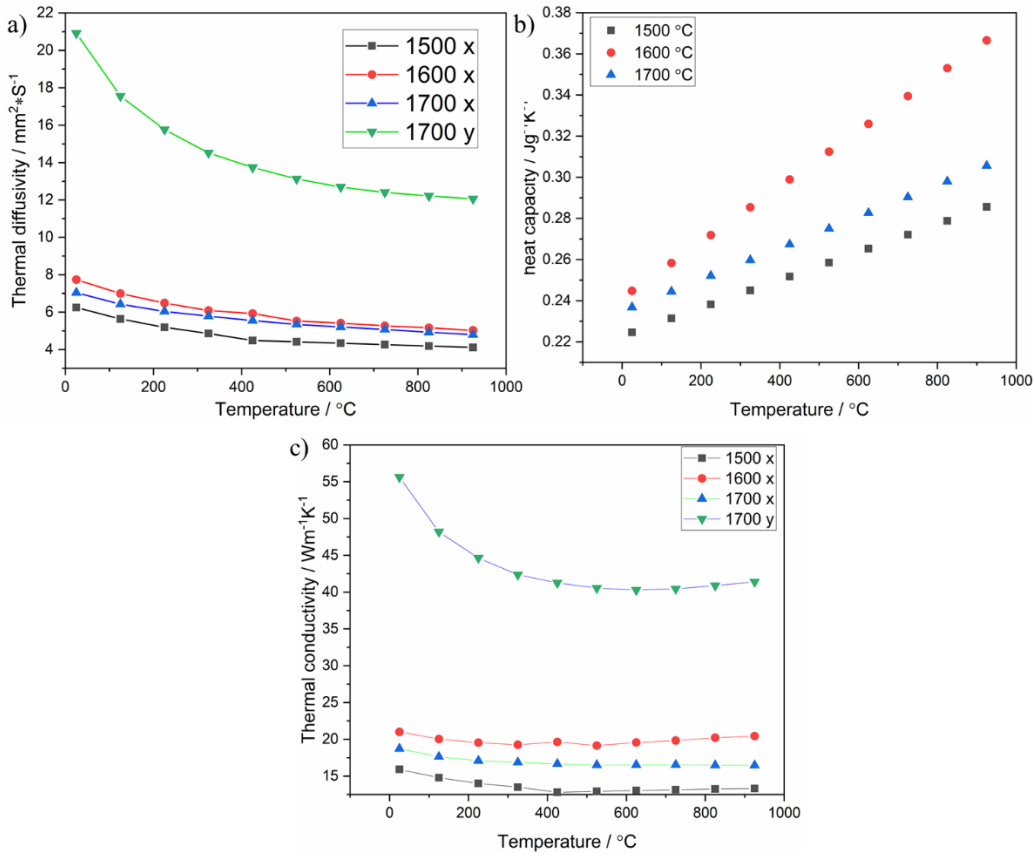

Figure 4.13 The thermal properties of SiCf/W composite with 0.08 mm foil. a) thermal diffusivity; b) heat capacity; c) thermal conductivity.

The thermal properties of SiCf/W composites with 0.08 mm foils are shown in Fig. 4.13, and the details about thermal conductivity of composites without foils can be found in Fig. 3.6. Here, the x and y means the through-plane and in-plane respectively. There is still higher conductivity in in-plane direction than that of through-plane direction, in addition the conductivity reduces with the improve of temperature due to more severe phonon scattering. Moreover, the thermal conductivity of composite with 0.08 mm foil is 55.6 W/(m·K) at room temperature higher than composite without foils of 51.5 W/(m·K). However, for composites with 0.05 mm foil, thermal conductivity should reduce larger in higher temperature due to lacking of the contribution from electrons in remained W.

4.4 The property and microstructure of SiCf/Mo composites

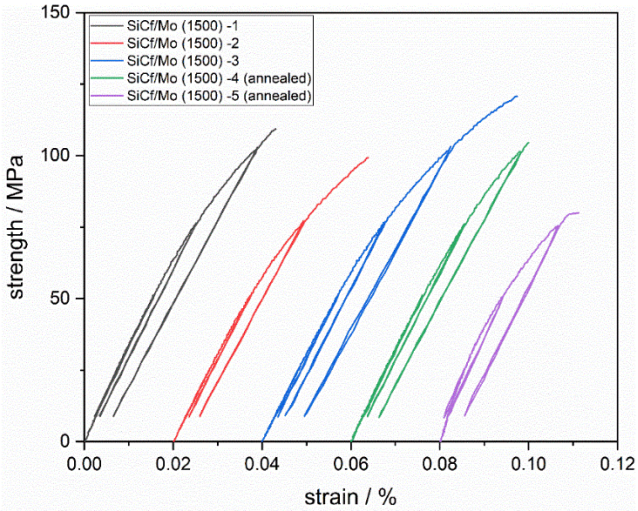

Figure 4.14 The mechanical property of SiCf/Mo composite with or without heat treatment measured at room temperature.

The Mo based composites were fabricated at 1500 °C for 1h with 20 MPa pressure reinforced by SiC fiber with 48.8 vol%, and the density of composite is 7.09 g/cm^3 calculated by size. The size of tensile bar is the same as bar for W-based materials. 3 of 6 bars were annealed at 1000 °C before tensile tets. In addition, the tensile test results of SiCf/Mo composite with or without heat treatment were shown in Fig. 4.14, in which one annealed bar failed to test. The UTS is 109.8 ± 10.7 MPa for unannealed composite bars, and for the annealed bars, the UTS is 92.2± 17.8 MPa, lower than the UTS of SiCf/W composite with 0.08 mm foil. In addition, the pseudo ductility can be noticed easily, suggesting that SiC fiber can act as an effective reinforcement to ameliorate the brittleness of Mo material. The recrystallization temperature of Mo foil is between 1000 °C and 1200 °C. Therefore, Mo foils have no contribution on the ductility for composite sintered 1500 °C.

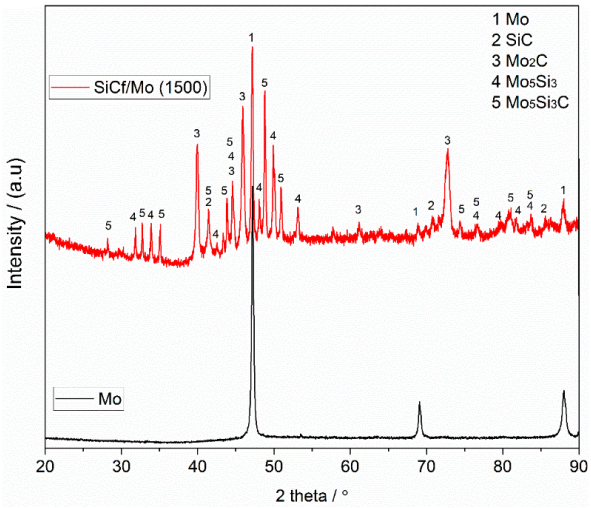

Figure 4.15 The XRD pattern of 1500 °C fabricated SiCf/Mo composites and pure Mo.

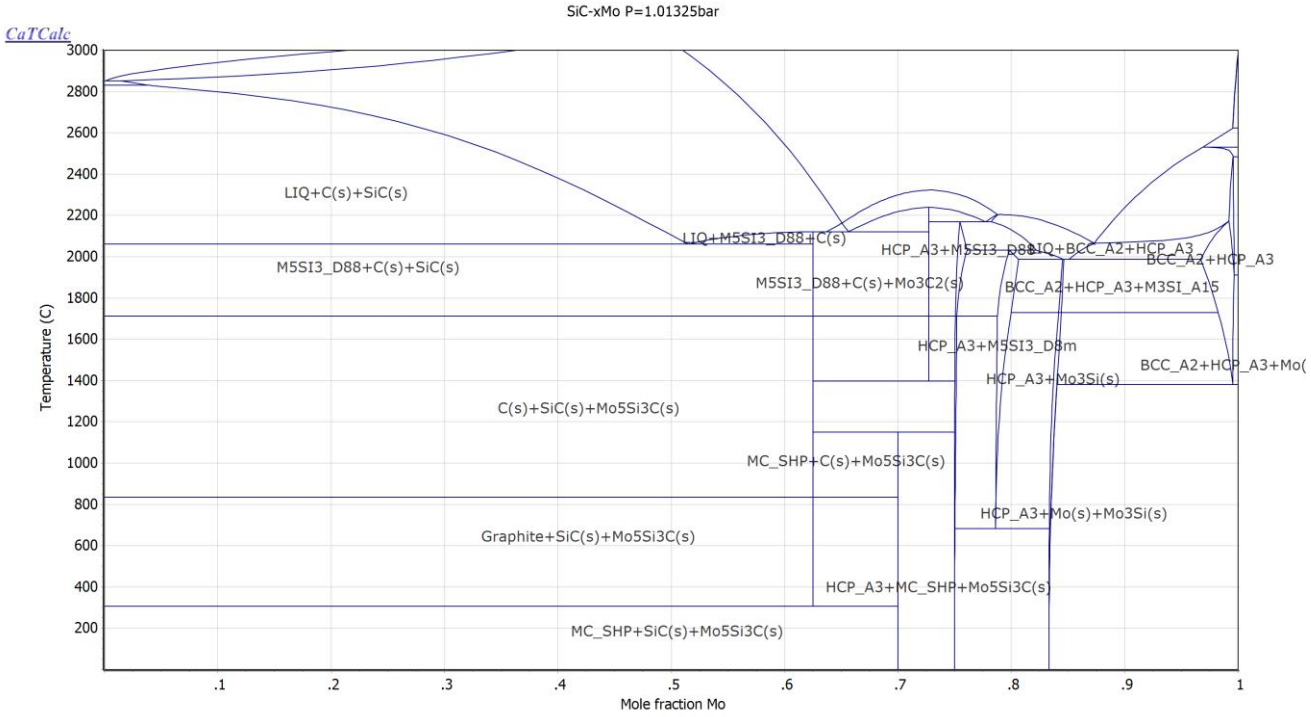

Figure 4.16 The phase diagram of SiC and Mo until 3000 °C

Like W and SiC system, Mo also reacted with SiC. In addition, the XRD patterns of 1500 °C sintered composite and pure Mo are displayed in Fig. 4.15. Ceramic phases of molybdenum silisides (Mo_5Si_3C and Mo_5Si_3) and carbide (Mo_2C) were generated and their peaks can be identified. While, SiC and Mo can be detected, indicating that there is still unreacted Mo

after high temperature sintering. Moreover, such results in accordance with the phase diagram of SiC and Mo system shown in Fig. 4.16. Mo only remained when temperature is lower than 1700 °C, and all Mo reacted with SiC at higher temperature.

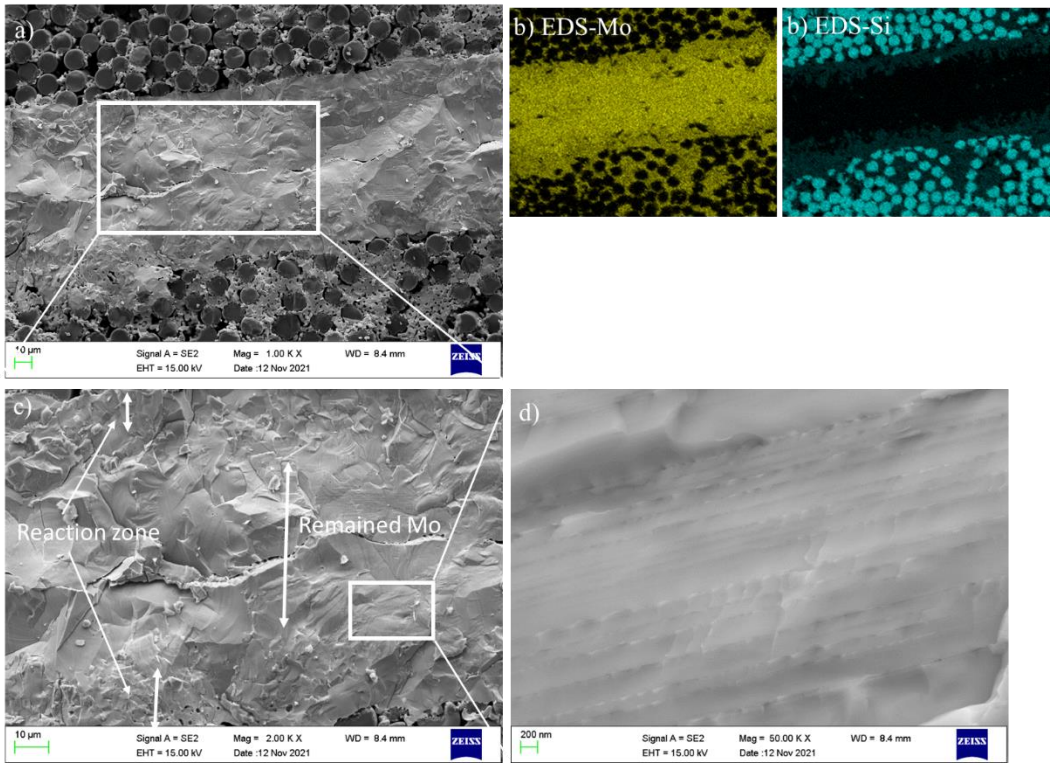

Figure 4.17 The SEM and EDS of SiCf/Mo composites after tensile test. a) The cross-section SEM image of SiCf/Mo; b) The EDS result of image a); c) and d) are the larger magnification images in a).

In order to know about the reaction in SiC and Mo clearly, the SEM images and EDS of tested SiCf/Mo composite after tensile test were also measured, and the images are revealed in Fig. 4.17. It is easy to notice that 3 layers, SiC fiber/reaction zone/Mo, from cross-section image can be observed similar with SiCf/W composite. Remained Mo can be found based on the EDS result. In addition, the depth of light atoms (Si and C) diffuses deeper than the depth of Mo atoms due to smaller grain size. Besides, twinned crystals can be found in remained Mo.

The thermal properties, including thermal diffusivity and conductivity as well as heat capacity, were measured or calculated from 25 °C to 925 °C for every 100 °C exhibited in Fig.

4.18. For composite, it was tested from 2 directions (x direction, through-plane direction; y direction, in-plane direction, see Fig. 3.6). The Cp data is measured by DSC, and both pure Mo

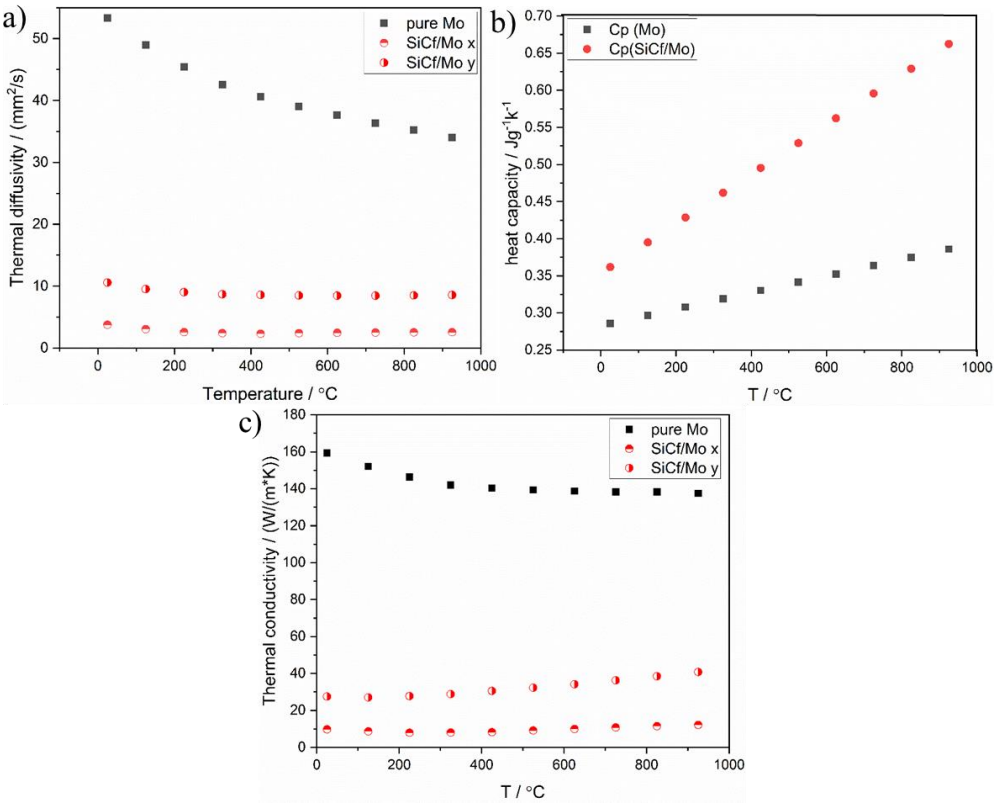

Figure 4.18 The thermal property of SiCf/Mo and pure Mo. a) thermal diffusivity; b) heat capacity; c) thermal conductivity.

and composite match the linear law and increase with increasing temperature. The density to calculate conductivity is used the data from its geometry. The diffusivity and conductivity of pure Mo reduced with the improve of temperature, and the data of pure Mo is higher compared with composite. The conductivity is 160 W/(m·K) at 25 °C and reduces to 145 W/(m·K), suggesting that Mo displays high thermal conductivity even at high temperature. In addition, the thermal property in y direction is larger than x direction for composite due to the location of open porosity like SiCf/W composites, and more detailed discussion can be found in Chapter 3.4. It need to be notice that the thermal conductivity of composite in both directions enhance with the temperature. This phenomenon might cause from the incorrect heat capacity data at high temperature, and the measured Cp data should be larger than the real data. Because the reactions between W and SiC occur in composites at high temperature, and such reactions caused the phases changes during heat

capacity measurement, thereby the heat capacity is different with the real value. For the thermal diffusivity, it can be considersed the pores in composites influences more than phases because both SiC and W have high diffusivity while composites show low diffusivity due to pores. However, the tested data at lower temperature are correct. The thermal conductivity of composite is about 30 W/(m·K) in in-plane direction and 10 W/(m·K) in through-plane direction lower than that of W based composite in both directions.

4.5 Conclusion

Continuous (long) SiC fiber reinforced W composites with 0.05 mm or 0.08 mm foil as matrix were fabricated at 1700 °C, and Mo based composites with 0.08 mm foil was sintered at 1500 °C successfully. The recrystallization temperature of W foil and Mo foil is from 1200 °C to 1400 °C and from 1000 °C to 1200 °C, respectively. Therefore, there is no contribution for ductility of composites from foil because all foils have recrystallized after sintering in this work. For W composites, the tensile test measured at RT implies that the W based composites obtained with 0.08 mm foil showed better apparent pseudo-ductile behavior due to the short pull-out foil and higher UTS of 197 MPa owing to high relative density and more remained W, suggesting that using dense foil as matrix is an efficient way to reduce the reaction rate. For Mo based composite, pseudo-ductility can also be found from the tensile test at RT, while both UTS and thermal conductivity are lower than those of W composites, Thus SiC fiber as reinforcement is one of the successful methods to ameliorate the embrittlement of metals, and such pseudo ductility is independent to consider the DBTT and recrystallization temperature. Moreover, it is expected that pseudo-ductile behavior will be obtained even if W and Mo are brittle caused by neutron irradiation or radiation hardening.

References

[1] V.S. Neshpor, The thermal conductivity of the silicides of transition metals, J. Eng. Phys. 15 (1968) 750–752. https://doi.org/10.1007/BF00829703.

[2] H.O. Pierson, Carbides of Group VI, Handb. Refract. Carbides Nitrides. (1996) 100–117. https://doi.org/10.1016/b978-081551392-6.50007-6.

[3] S. Nogami, W. Guan, A. Hasegawa, M. Fukuda, Feasibility of utilizing tungsten rod for fusion reactor divertor, Fusion Sci. Technol. 72 (2017) 673–679. https://doi.org/10.1080/15361055.2017.1347463.

[4] A. Hasegawa, M. Fukuda, T. Tanno, S. Nogami, K. Yabuuchi, E. Agency, Neutron Irradiation Effects on Grain-refined W and W-alloys MPT02, Talk. (2014) 1–8.

[5] S.J. Zinkle, N.M. Ghoniem, Operating temperature windows for fusion reactor structural materials, Fusion Eng. Des. 51–52 (2000) 55–71. https://doi.org/10.1016/S0920-3796(00)00320-3.

[6] C.C. Tang, D.W. Hess, Tungsten Etching in CF 4 and SF 6 Discharges, J. Electrochem. Soc. 131 (1984) 115–120. https://doi.org/10.1149/1.2115489.

[7] K. Tsuchida, T. Miyazawa, A. Hasegawa, S. Nogami, M. Fukuda, Recrystallization behavior of hot-rolled pure tungsten and its alloy plates during high-temperature annealing, Nucl. Mater. Energy. 15 (2018) 158–163. https://doi.org/10.1016/j.nme.2018.04.004.

[8] C. Ren, Z.Z. Fang, L. Xu, J.P. Ligda, J.D. Paramore, B.G. Butler, An investigation of the microstructure and ductility of annealed cold-rolled tungsten, Acta Mater. 162 (2019) 202–213. https://doi.org/10.1016/j.actamat.2018.10.002.

[9] W.F. Seng, P.A. Barnes, Calculations of cobalt suicide and carbide formation on SiC using the Gibbs free energy, Mater. Sci. Eng. B Solid-State Mater. Adv. Technol. 76 (2000) 225–231. https://doi.org/10.1016/S0921-5107(00)00457-8.

Chapter 5. Effect of fiber on properties of SiC fiber reinforced W composite

5.1 Introduction

The property of fiber is also a parameter to affect composites' properties. The ultimate tensile strength σ_{UTS} of composites can be estimated by the equations [1,2] of $\sigma_{UTS} = V_f\sigma_C(\frac{2}{m+2})^{1/(m+1)}\frac{m+1}{m+2}$ and $\sigma_C = (\frac{\sigma^0\tau L_0}{\gamma})^{1/(m+1)}$, in which where σ_C is the relevant strength of the fibers, m is the Weibull modulus of the fibers, σ^0 is the Weibull reference strength of the fibers, L_0 is the gauge length, τ is the sliding resistance, V_f is fiber volume fraction, and γ is the radius of the fiber. Effect of fiber volume fraction [2–5], fiber arrangement [3,5], and fiber treatment [6] on the property of composites were studied. In this work, unidirectional SiC fiber and 2 dimension (woven SiC fiber) as reinforcement was used to fabricate W composites by hot-press, then the mechanical property was examined by tensile test to evaluate which kinds of fiber show better property. In addition, SiC/W woven fiber was used as reinforcement in this work to ameliorate the mechanical property and to improve the high temperature thermal property especially in through-plane direction. because W shows higher thermal conductivity than SiC at high temperature due to high contribution from electrons. Moreover, the relationship between microstructure and properties was discussed.

5.2 The property and microstructure of composites with woven SiC fibers

Two different methods with or without W powder sheet were taken advantage of 2D SiC fibers to fabricate composite (see Fig. 2.1). In addition, pure W by powders or foils were also sintered. The properties are shown as follows.

5.2.1 Basic information of prepared composites with woven fibers

Table 5.1 Densification of SiC fiber reinforced W composites fabricated by 2 methods and pure W.

	1500				1700				1900			
	Vf%	ρ/(g▪cm^3)	P/%	R.D.	Vf%	ρ/(g▪cm^3)	P/%	R.D.	Vf%	ρ/(g▪cm^3)	P/%	R.D.
Wp	--	17.30	9.66	90.34	--	16.61	13.66	86.34	--	17.32	9.93	90.07
Wf	Debonding in cutting for tensile test bar								--	18.87	1.95	98.05
MANF	Debonding in cutting for tensile test bar				49.73	9.12	19.14	80.86	50.73	9.73	12.06	87.94
MAF	Debonding in cutting for tensile test bar								36.80	11.62	12.67	87.33
MBNF	47.57	7.86	32.05	67.95	51.84	8.98	17.51	82.49	50.65	10.67	3.65	96.35
MBF	46.41	8.44	28.17	71.83	41.93	10.57	15.32	84.68	39.19	11.35	12.15	87.85

Note: Vf (fiber volume fraction), ρ (density), R.D. (relative density), P (porosity), Wp (pure W sintered by W powder), Wf (pure W prepared by W foil)

The fiber volume fraction, density and porosity of composites are shown in Table 5.1, in which density is calculated by its size. All materials densified with the temperature, especially for MBNF composite. Pure W only by W foils and composite by MA with foils delaminated in both 1500 °C and 1700 °C. In addition, MANF composite fabricated at 1500 °C was also debonding in the cutting period to prepare the tensile test bar, indicating that the W powder might be not go insides the fiber bundle after 20 MPa pressure with 30 min at 200 °C. While for composites by MB, there is no debonding even if the porosity higher than 30 vol%. Therefore, MB should be more appropriate compared with MA from W powder sheet.

An interesting phenomenon needs to be noticed that the porosity of 1500 °C prepared pure W by powder of 10.66 % is lower than that of 1700 °C sintered W of 13.66% (see Table 5.1), which may be caused by the existence of tungsten oxide (WO_3). As we all know, W is oxidized easily, especially for small grain size powders with specific surface area. The grain size in this work is 0.6 μm, so the WO_3 has existed before sintering. In addition, the melting point of WO_3 is 1470 °C, lower than the sintering temperature of 1500 °C. Therefore, such oxides act as sintering additive to generate the liquid phase. However, the WO_3 boiled when temperature reached to 1700 °C, and such boiled oxides gas can not pass whole material due to the pressure with 20 MPa during sintering, which is responsible for the high porosity.

5.2.2 Mechanical property and microstructure of prepared composites with woven fibers

The tensile test results of pure W fabricated by foils and powders were exhibited in Fig. 5.1. The annealing condition is 1000 °C for 1 h in Ar. No results of pure W by foils sintered lower than 1900 °C due to the delamination of foils during cutting period for the tensile test specimen. No ductile behavior can be found in all specimens whether by powders or foils. The inaccuracy in the results caused by the wrong paste of strain gauge.

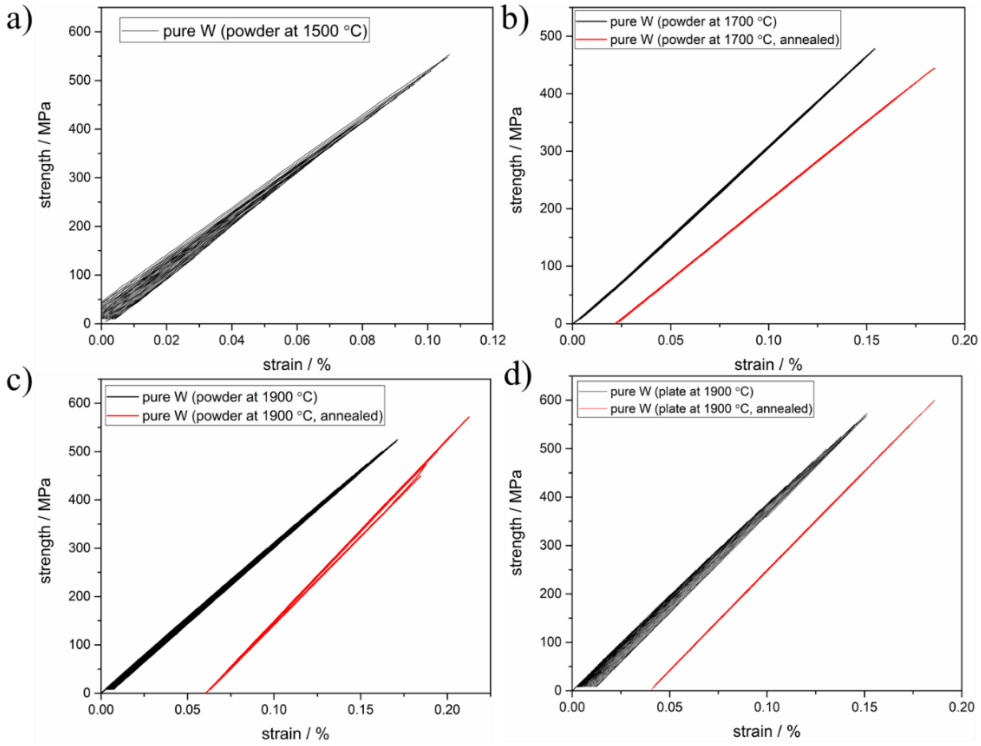

Figure 5.1 The tensile test results of pure W by powders fabricated from 1500 °C to 1900 °C a), b) c) and d) by foils sintered at 1900 °C d) with or without annealing.

In addition, the tensile test results of composites by woven fibers fabricated from 1500 °C, 1700 °C, and 1900 °C respectively by 2 methods (MA and MB) with or without foils are displayed in Fig. 5.2. The pseudo ductility reduced with sintering temperature for all composites, indicating that densification cause the strong interface between fiber and matrix. The tensile test bar of MANF1500, MAF1500, and MAF1700 delaminated, therefore the results are not shown here like pure W prepared by foils, indicating that the method A is not suitable to fabricate SiC fiber reinforced W composites. For composites by MA with or without foils at 1700 °C and 1900 °C,

only little pseudo ductility can be identified, compared with the pure W. While apparent pseudo ductile behavior can be noticed in composites by MB with or without foils at 1500 °C and 1700 °C, and the strength of MBF1500 and MBF1700 is higher than composite without foils. It can be assumed that foils are responsible for the higher strength at 1500 °C and 1700 °C. It is worth noting that composite with or without foils at 1900 °C by MB, no ductile behavior was recognized. Moreover, 1900 °C is a little high for woven fiber reinforced composites. In addition, the strength between MBF and MBNF at 1900 °C are almost identical with 120 MPa, which is the highest strength for composite by MB with woven fiber but still lower than the pure W of higher than 500 MPa.

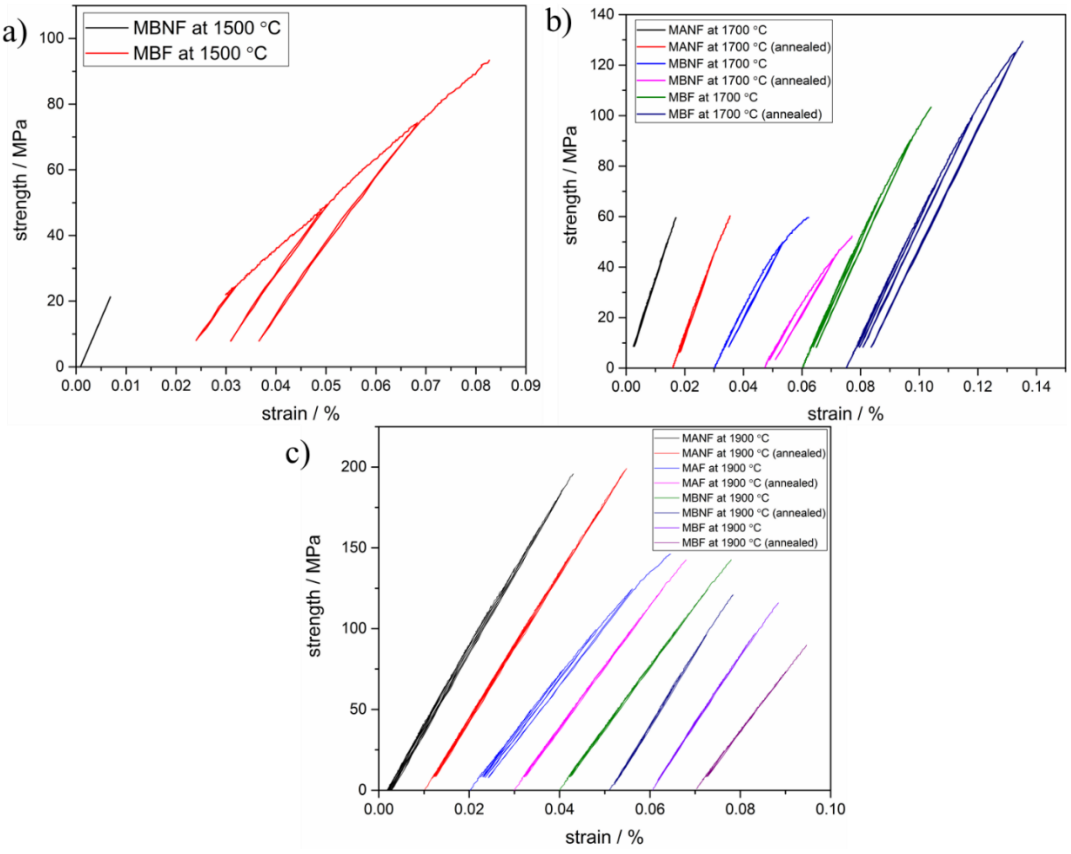

Figure 5.2 The tensile test results of fabricated composites with or without annealing. a), b) and c) are the results of composites fabricated from 1500 °C, 1700 °C, and 1900 °C respectively.

The summary of the relationship between temperature and strength for every tensile test bar is revealed in Fig. 5.3. The strength of all composites by woven fiber for both methods is lower than that of pure W irrelevant to the sintering temperature and W sources (by powder or foil), and

the strength increased with temperature due to the decrease of porosity, which also caused the strong interface between fiber and W at higher sintering temperature. In addition, such strong interface leads to the reduction of pseudo ductility (see Fig. 5.2). While for the pure W fabricated by powder, the lowest UTS is sintered at 1700 °C rather than 1500 °C in this work, matched with the density and porosity, namely W sintered at 1700 °C indicates lower density and higher porosity, caused by the low melting and boiling point of WO_3. In addition, the annealing at 1000 °C almost has no effect on tensile test results, no matter UTS or ductile behavior, for all specimens.

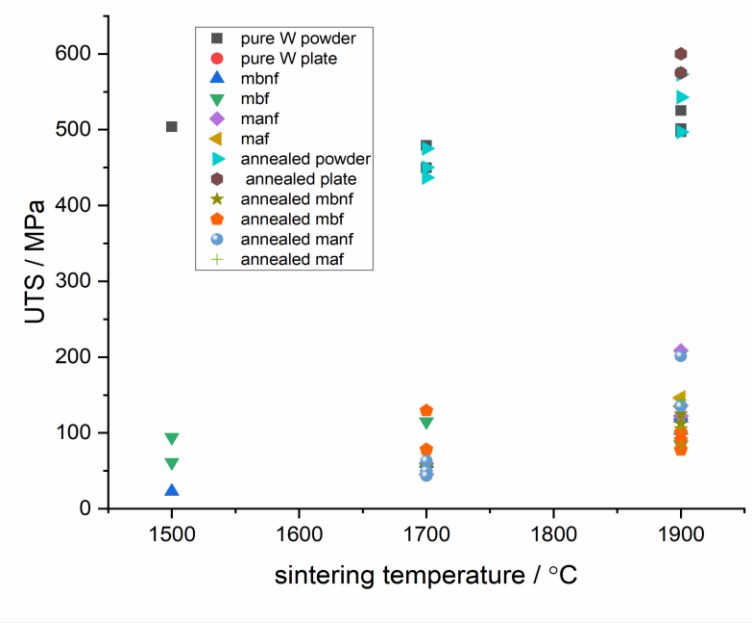

Figure 5.3 The relationship between sintering temperature and ultimate tensile strength (UTS) by every tensile test bar.

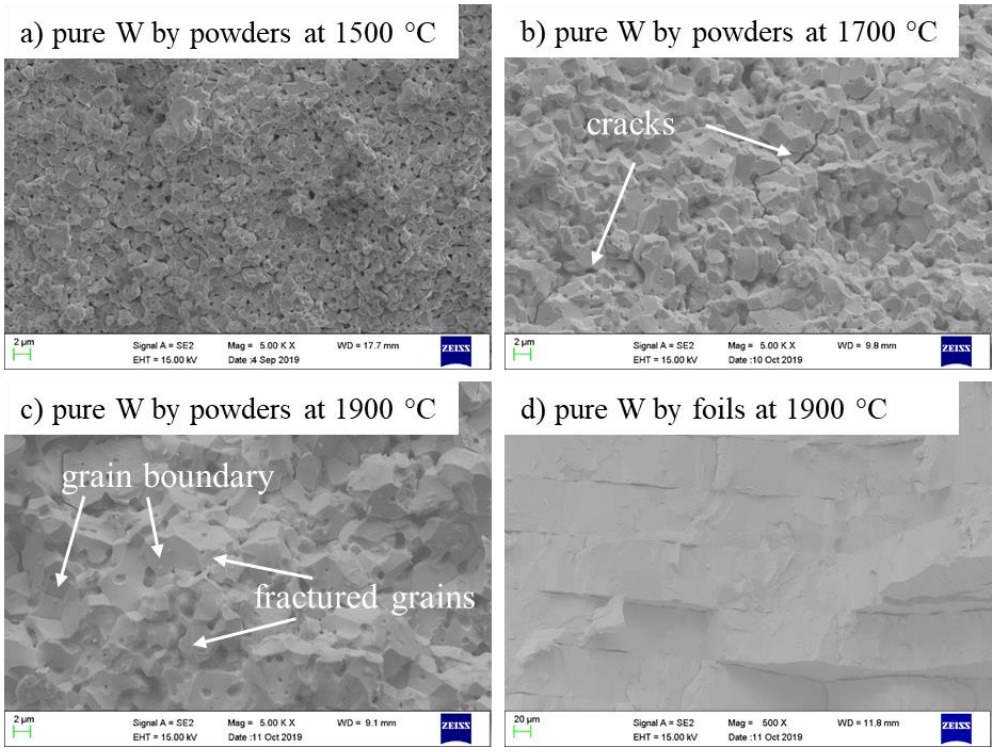

Figure 5.4 The cross sectional SEM images of pure W after tensile test at room temperature. a) pure W by powders at 1500 °C, b) pure W by powders at 1700 °C, c) pure W by powders at 1900 °C, d) pure W by foils at 1900 °C.

The cross sectional microstructure of tested specimens was observed to understand the connections between microstructure and property, and the microstructure of pure W sintered by powders or foils at different temperature after tensile test were revealed at Fig. 5.4. It is easy to notice the grain growth with the improvement of sintering temperature from 1500 °C to 1900 °C in pure W by powders. Moreover, sintering pores are identified in all powder sintered specimens. At 1500 °C, the size is lower than 1 μm, irregular pores are in the grain boundary, revealing that 1500 °C is low to sinter W powder together. While the size reached to 10 μm sintered at 1900 °C. Therefore, small grain size in 1500 °C sintered W may be also responsible for the higher strength compared with W sintered at 1700 °C. In addition, the materials at lower sintering temperature (1500 °C and 1700 °C) display intergranular fracture, and the cracks at grain boundary can be easily found in 1700 °C fabricated specimen (see Fig. 5.4 b)) due to the presence of oxide. In addition, both intergranular and transgranular fracture can be recognized in pure W by powders at 1900 °C. For the material by foils, the gaps between each foils were still observed, indicating that 1900 °C is still low to join without adding sintering additives.

The SEM images of microstructure of SiC fiber reinforced W composites with or without foils by both methods after tensile test are displayed in Fig. 5.5. For MA, it seems only little W powders moved into the fiber bundle for composite without foil sintered at 1700 °C even although pressure with 20 MPa was applied at 200 °C for 30 min, which is the reason why the composites fabricated by MA delaminated when sintering temperature lower than 1700 °C. For composites by MB, they were fabricated successfully even if the sintering temperature is 1500 °C, and the powders can be recognized easily in the fiber bundle. The element analysis and the detailed discussion can be found in Chapter 3.2.

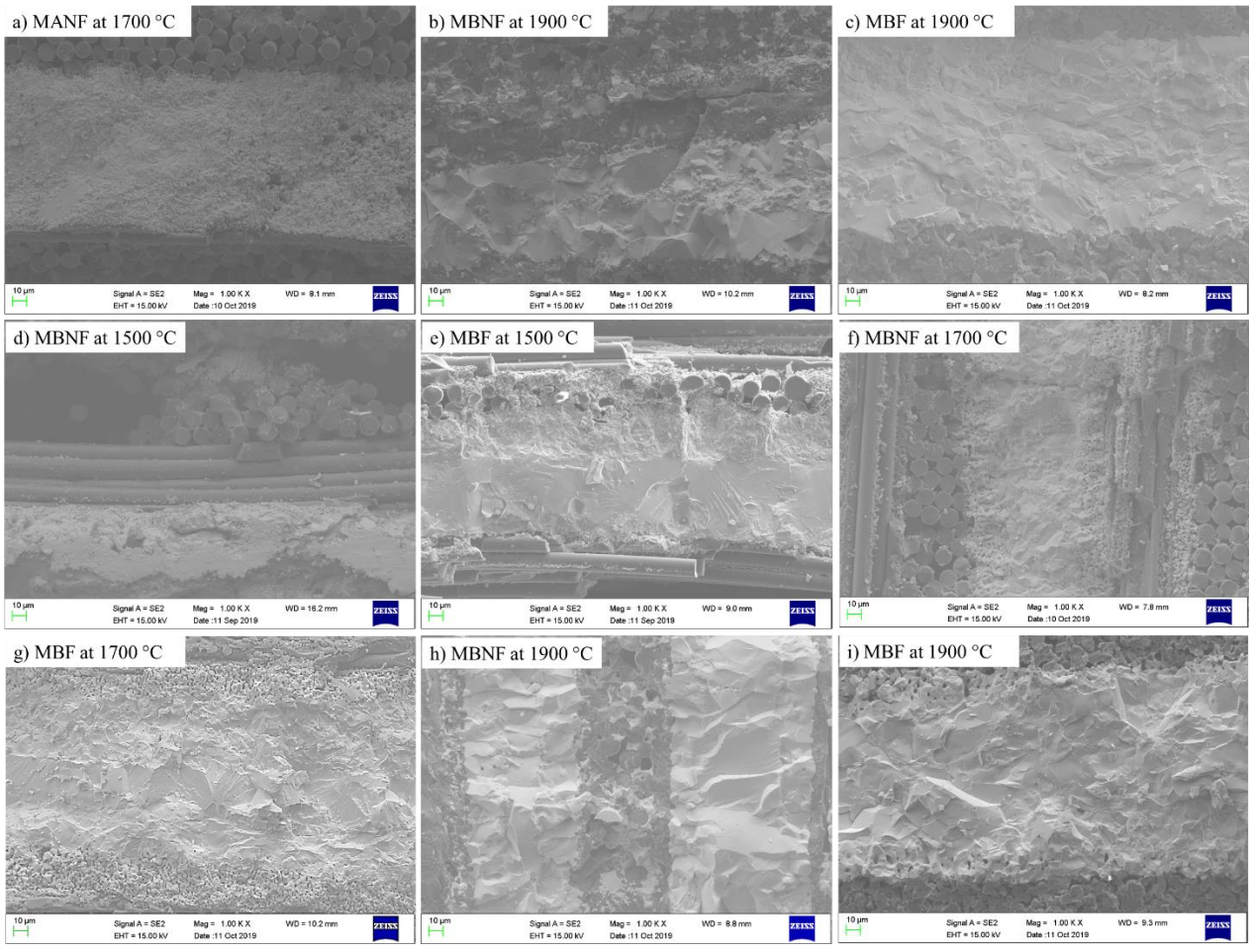

Figure 5.5 The cross-section SEM images of SiC fiber reinforced W composites with both methods fabricated at different temperature after tensile test at RT

5.3 The property and microstructure of fabricated composites with unidirectional SiC fiber

Detailed properties about unidirectional SiC fiber reinforced W composites can be found in Chapter 3 and Chapter 4.3.

5.4 The property and microstructure of fabricated composites with woven SiC and W fibers

W wire with 0.1 mm diameter woven with Hi-Nicalon type S SiC fiber was fabricated successfully by twill way with 4/4 by different pitches (0.3 mm, 0.5 mm, and 0.7 mm). The photo of SiC/W fabric with 0.7 mm pitch was displayed in Fig. 5.6.

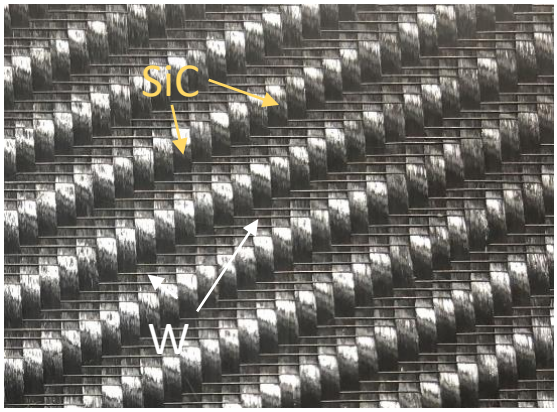

Figure 5.6 The photo of fabricated SiC/W fabric by twill way with 4/4 by 0.7 mm pitch.

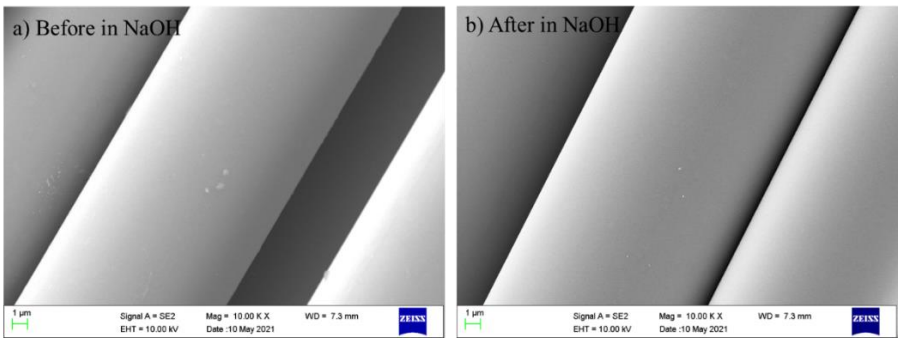

Figure 5.7 The SEM image of SiC fiber before and after in NaOH (aq, 0.98wt%) for 50 h at room temperature.

The SiC/W fabric was washed by NaOH solution before using. Besides, in order to evaluate whether SiC fiber is stable in NaOH aq, the same SiC fiber was in 0.98 wt% NaOH solution for 50 h at room temperature firstly, and the SEM images of SiC fiber before and after in solution are exhibited in Fig. 5.7. It can be found that SiC fiber is stable in NaOH solution even for 50 h.

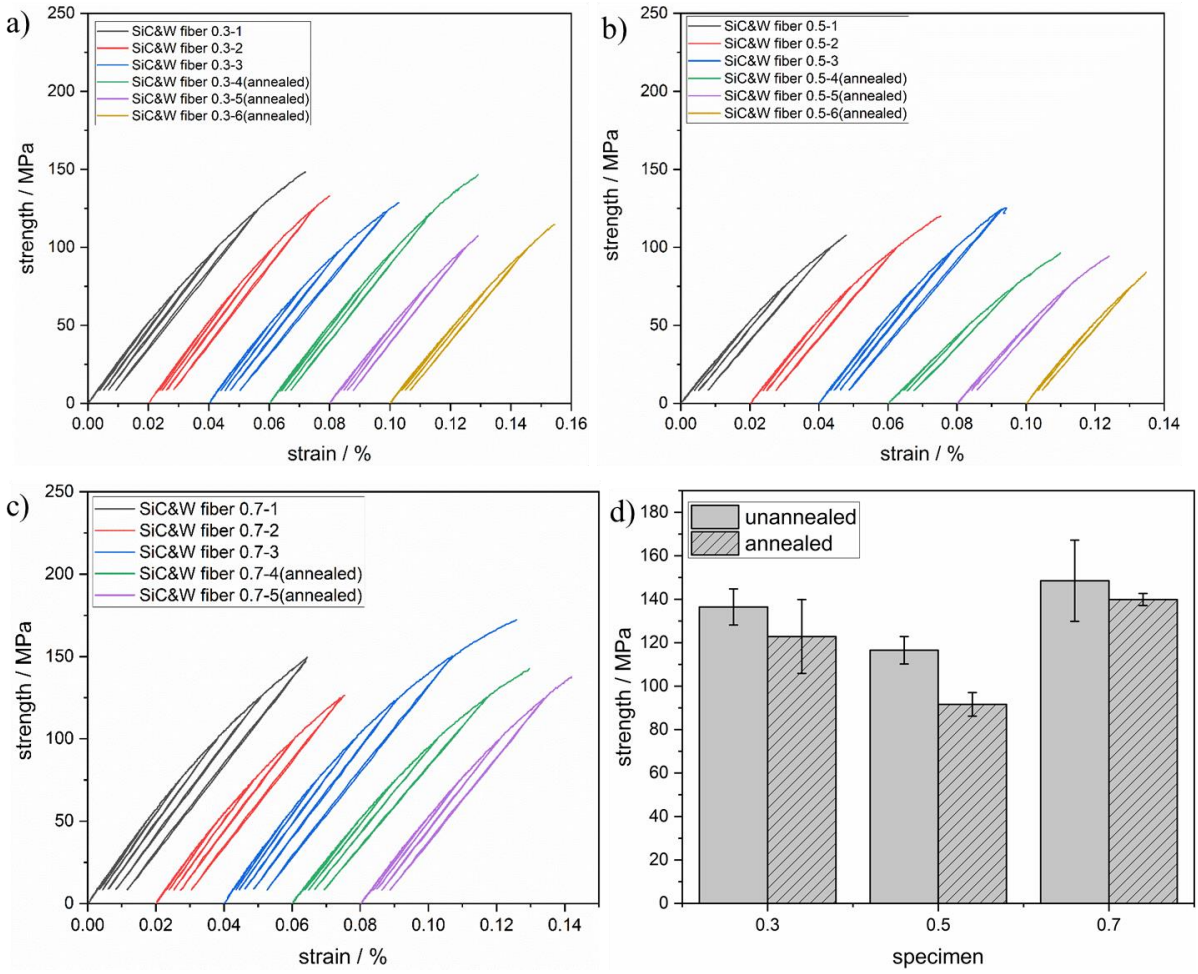

Figure 5.8 The tensile test results of SiC/W fabric reinforced W composites with 0.08 mm foil sintered at 1700 °C with or without annealing. a) 0.3 mm pitch composite; b) 0.5 mm pitch composite; c) 0.7 mm pitch; d) summary of mechanical property of SiC/W fabric reinforced composites.

The mechanical property of 1700 °C fabricated SiC weaved with W fiber reinforced W composites with 0.08 mm foils measured at room temperature is revealed in Fig. 5.8. The UTS of composites with 0.3 mm, 0.5 mm, and 0.7 mm pitch without annealing are 136.5 $\pm$ 8.3 MPa, 116.5 $\pm$ 6.3 MPa, and 148.5 $\pm$ 18.7 MPa respectively. In addition, the strength of all composites reduced

slightly after 1000 °C annealing for 1 h, and the values are 122.9 ± 17.0 MPa for 0.3 mm pitch fabric sintered composite, 91.6 ± 4.4 MPa for 0.5 mm pitch fabric prepared composite, and 139.9 ± 2.8 MPa for 0.7 mm pitch fabricated composite respectively. In addition, the values caused by different pitches have not changed much, which may cause from the deviation during measurement. Moreover, it was easy to find the more obvious pseudo-ductility in SiC/W fabric reinforced W composite compared with woven SiC fiber reinforced composite, while weaker than pseudo-ductility in composite reinforced by unidirectional SiC fiber. In addition, the UTS of composite by woven SiC fiber with 0.05 mm foils is 103.33 MPa, and strength of composite by unidirectional SiC fiber with 0.05 mm and 0.08 mm foils is 125.97 MPa and 197.12 MPa respectively. The UTS of composites by UD fiber is higher than both 2D fibers. Because for 2D fiber, when the direction of fiber is parallel to the load direction during tensile test fibers can work, only half of fibers have contribution to the mechanical property, shown in Fig. 5.9. Therefore, the UTS of composite by 2D fiber is theoretically about 50% of UTS of UD composite. Both the strength of composites by both 2D fibers was higher than 1/2 σ(UD composite). Therefore, 2D fibers are better than UD fiber. But for these two kinds of 2D fibers, it needs to be studied further to find which one is better.

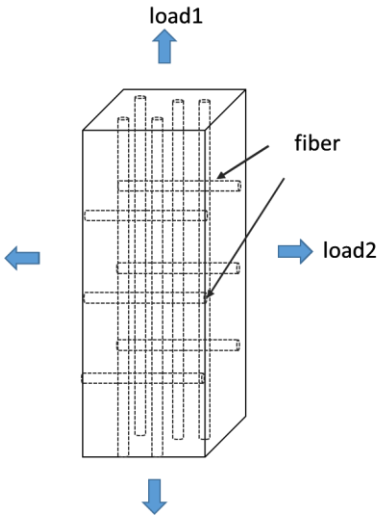

Figure 5.9 The schematic diagram of composite by 2D fiber under load.

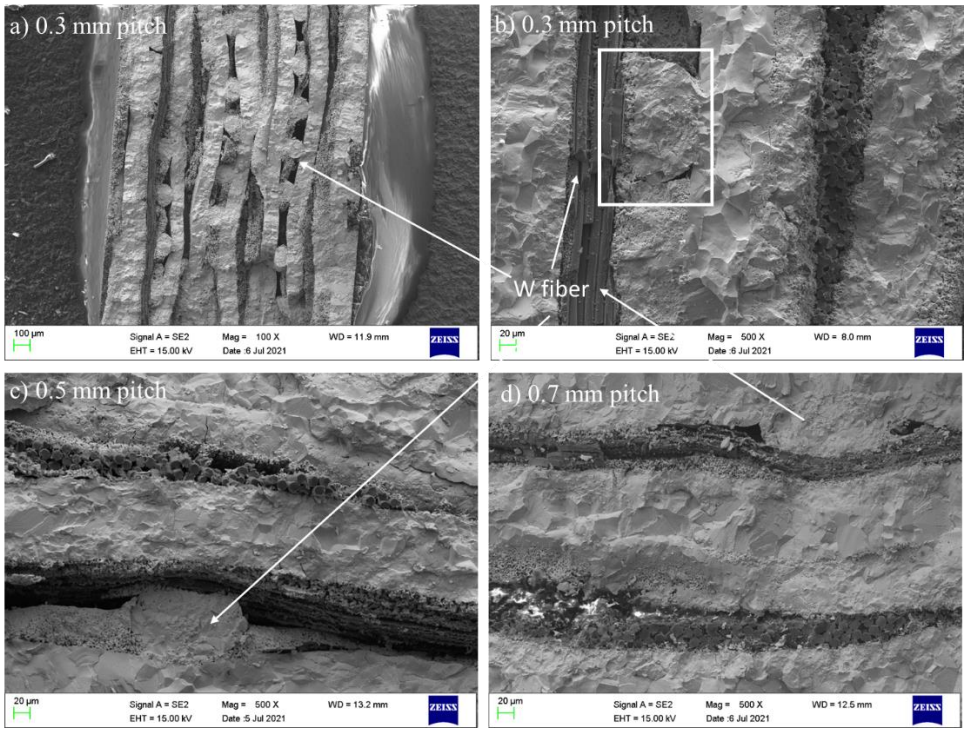

Figure 5.10 The cross-sectional SEM images of SiC weaved W fiber reinforced W composite after tensile test at room temperature. a) composite with 0.3 mm pitch SiC/W woven fiber; b) large magnification of image a); c) composite with 0.5 mm pitch SiC/W woven fiber; d) composite with 0.7 mm pitch SiC/W woven fiber.

The SEM images after measuring the mechanical property are shown in Fig. 5.10. Very short fiber pull-out effect can be observed from the cross-sectional images. In addition, larger pores can be viewed from image a). Besides, the damage of the W wire can be found, and only half diameter remained after sintering, such damages destructive to its mechanical property and thermal property.

The reason why SiC/W fabric is introduced is to improve the heat transfer in the direction perpendicular to the surface of the fabric, because SiC has a lower thermal conductivity than tungsten at high temperature. The layer of SiC fibers has lower thermal conductivity than W matrix layer. The thermal properties of SiC/W woven fiber reinforcement W composites are shown in Fig. 5.11. The thermal conductivity is also higher in in-plane direction than that of through-plane direction. The highest thermal conductivity is composite by 0.3 mm pitch fiber of 57.2 W/(m·K) in in-plane direction, slightly higher than UD composite with 0.08 mm foils 55.6 W/(m·K), which

caused from the high porosity in composites with SiC/W woven fiber. For the through-plane direction, similar with in-plane direction, the thermal conductivity of composites with W wire is lower at room temperature than that of UD composites with foils due to high porosity. However, composites by SiC/W fabric show higher conductivity at high temperature owing to the introduced W wire when composites were sintered at 1700 °C. In addition, the thermal diffusivity of composites with W wire in through-plane direction reduced just slightly compared to that of composites without W wire (see Fig. 4.13) because of the contribution from W wire. Therefore, introducing W wire is perspective method to improve thermal conductivity.

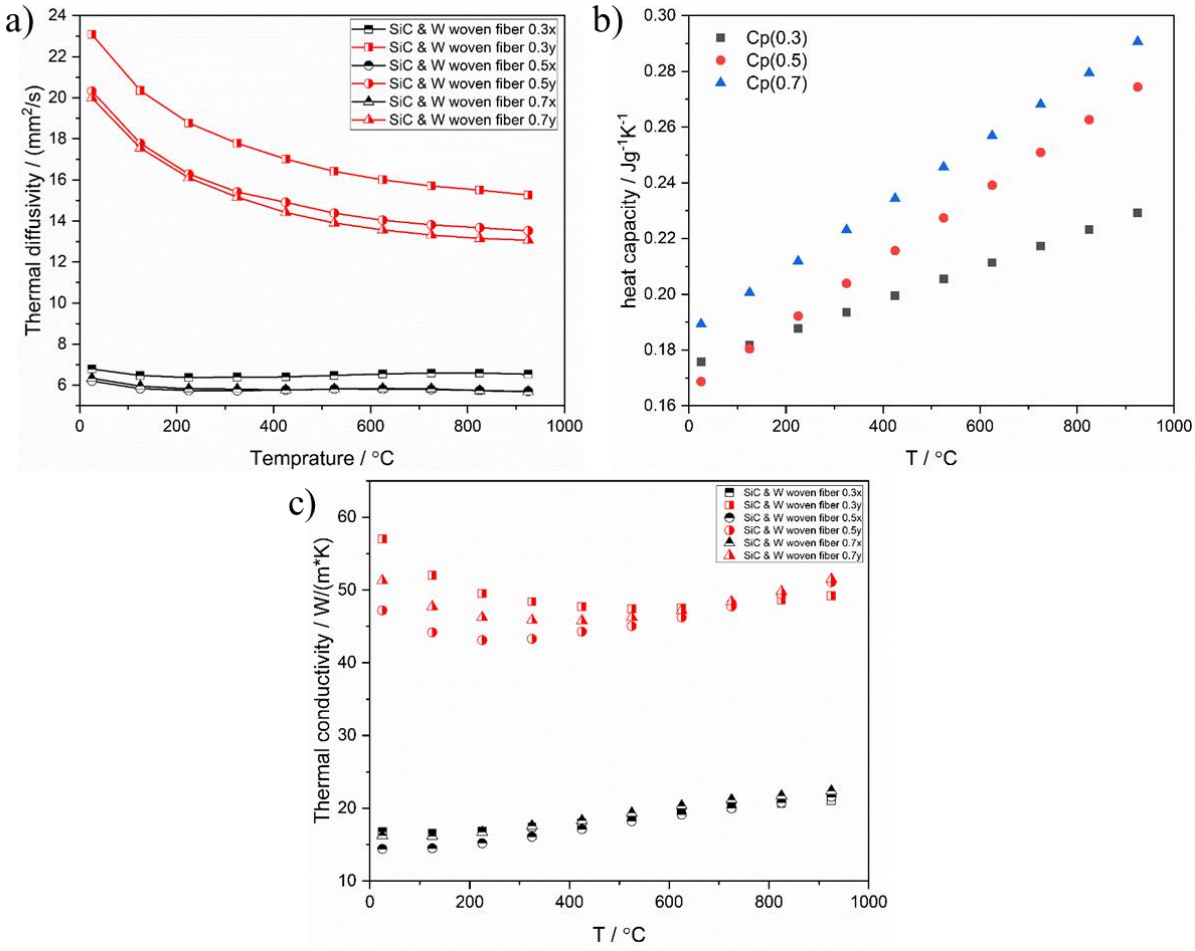

Figure 5.11 The thermal property of 2D SiC/W fiber reinforced W composites. a) thermal diffusivity; b) heat capacity; c) thermal conductivity.

5.5 Conclusion

The effect of fiber on the property of composite was investigated in this Chapter. Three kinds of fiber, woven SiC fiber, unidirectional SiC fiber, and SiC and W woven fiber, were utilized to reinforce W. For SiC woven fiber, 2 methods were used to fabricate composites with woven fiber. In addition, the results show all composites fabricated by method with powder sheet at 1500 °C deboned during processing to achieve tensile test bar. Therefore, method B is more appropriate than method A. Moreover, in these three kinds of fibers reinforced composite, all three kinds of composites displayed pseudo-ductile behavior at room temperature. In addition, composites with unidirectional fiber show the highest strength, because only 50% fiber works during tensile test in composites by the other two kinds of woven fibers, and the strength of both composites by both 2D fibers were higher than the 50 % strength of composite by unidirectional fiber. Therefore, 2D fibers are better than UD fiber. But for these two kinds of 2D fibers, it needs to be studied further to find which one is better. For thermal property, the composite by 2D W/SiC fabric shows higher conductivity at high temperature due to the introducing W wire with high conductivity from electrons especially in through-plane direction compare with composites without W wire. Therefore, SiC/W woven fiber might be more suitable combined the thermal property and mechanical property.

References

[1] W.A. Curtin, Theory of Mechanical Properties of Ceramic-Matrix Composites, J. Am. Ceram. Soc. 74 (1991) 2837–2845. https://doi.org/10.1111/J.1151-2916.1991.TB06852.X.

[2] K. Shimoda, T. Hinoki, Effects of fiber volume fraction on the densification and mechanical properties of unidirectional SiCf/SiC-matrix composites, J. Eur. Ceram. Soc. 41 (2021) 1163–1170. https://doi.org/10.1016/J.JEURCERAMSOC.2020.09.024.

[3] E. Elkazaz, W.A. Crosby, A.M. Ollick, M. Elhadary, Effect of fiber volume fraction on the mechanical properties of randomly oriented glass fiber reinforced polyurethane elastomer with crosshead speeds, Alexandria Eng. J. 59 (2020) 209–216. https://doi.org/10.1016/J.AEJ.2019.12.024.

[4] C. Qin, N. Soykeabkaew, N. Xiuyuan, T. Peijs, The effect of fibre volume fraction and mercerization on the properties of all-cellulose composites, (2007). https://doi.org/10.1016/j.carbpol.2007.06.019.

[5] H. Bouafif, A. Koubaa, P. Perré, A. Cloutier, Effects of fiber characteristics on the physical and mechanical properties of wood plastic composites, Compos. Part A Appl. Sci. Manuf. 40 (2009) 1975–1981. https://doi.org/10.1016/J.COMPOSITESA.2009.06.003.

[6] M.Z. Rong, M.Q. Zhang, Y. Liu, G.C. Yang, H.M. Zeng, The effect of fiber treatment on the mechanical properties of unidirectional sisal-reinforced epoxy composites, Compos. Sci. Technol. 61 (2001) 1437–1447. https://doi.org/10.1016/S0266-3538(01)00046-X.

Chapter 6 Assessment of the potential diffusion barriers between metals and SiC

6.1 Introduction

Tungsten (W), as a metal with the highest melting point, is expected as the plasm facing material, and silicon carbide (SiC) composites are expected as the structural materials for the nuclear fusion power plant [1]. In addition, the coefficient of thermal expansion (CTE) of W and SiC is 4.6 and 4.7 × 10^{-6} /°C, respectively. Therefore, the development of the W and SiC composites joint technology [2–4] or the usage of SiC to reinforce W [5–7] are the critical issues for the larger and more complex components in a fusion reactor. However, severe interfacial solid-state reactions occur between SiC and W after annealing at high temperature generating various carbides (WC and W_2C) and silicides (W_5Si_3 and WSi_2) [3,7–9]. Such produced ceramics phases damage the strength and thermal conductivity of W and SiC. Moreover, the reaction zone still exists even joined by a rapid joining method (spark plasma sintering, SPS) [2,10]. Therefore, an effective diffusion barrier is very essential for SiC and W systems to suspend the reaction.

Nevertheless, only a few works focus on diffusion barriers in SiC and W systems. It is reported that 70 nm thick TaC [11] or 100 nm thick TiN [12] can act as an effective diffusion barrier at 1000 °C, in which no reactions can be found and just grain growth after 24 h annealing. However, the evaluating temperature is much lower than the sintering temperature to fabricate the SiC fiber reinforced W composites. Umber et al. [5] fabricated the TiN-coated SiC particles reinforced W materials by SPS at 1700 °C for 3 min, and the intensity of tungsten carbides and silicides' peaks reduced a lot compared with the composite without TiN coating. However, three min is too short to evaluate whether it works. Roger et al. examined the TiC [13] and TiN [14] layers, and both of them can noticeably lessen the depth of the reaction zone after 1500 °C for 16 h annealing. But the thickness used in this work is thicker than 10 μm, which is too thick for interface material in a composite. Nonetheless, it's worth investigating TiC and TiN as diffusion barriers further. ZrN and ZrC as other typical transition metal nitrides and carbides with both Ti and Zr belonging to group IV elements, show similar properties to TiN and TiC, such as high melting point and good corrosion resistance, etc. Moreover, ZrC [15,16] or TiC [17,18] as well as ZrN [19,20] powders were added to W to remove the oxygen impurities in the grain boundary to improve the mechanical property of W, so there is evidence of good stability between carbides, nitrides and W. In addition, the thermal conductivity of these transition metal nitrides and carbides display positive trend with temperature because of high contribution of electrons [21–23]. Thus, ZrN and ZrC were also chosen in this work. In addition, oxides (ZrO_2, TiO_2 and Er_2O_3) with high

thermal stability and low activation to irradiation [24] were selected as interface materials as well in order to suppress the movement of Si and C atom. ZrO_2 powder was also used to ameliorate W's brittleness sintered higher than 2000 °C [25]. In addition, Er_2O_3 acted as the interface layer in W fiber-reinforced W composites [26,27]. Thus, it's stable between these oxides and W. Therefore, in this work, these candidate materials were chosen to assess the possibility of an effective diffusion barrier for SiC and W systems, and evaluations were carried out by SiC and W joints.

6.2 Diffusion couple about uncoated CVD-SiC joined with metal foils

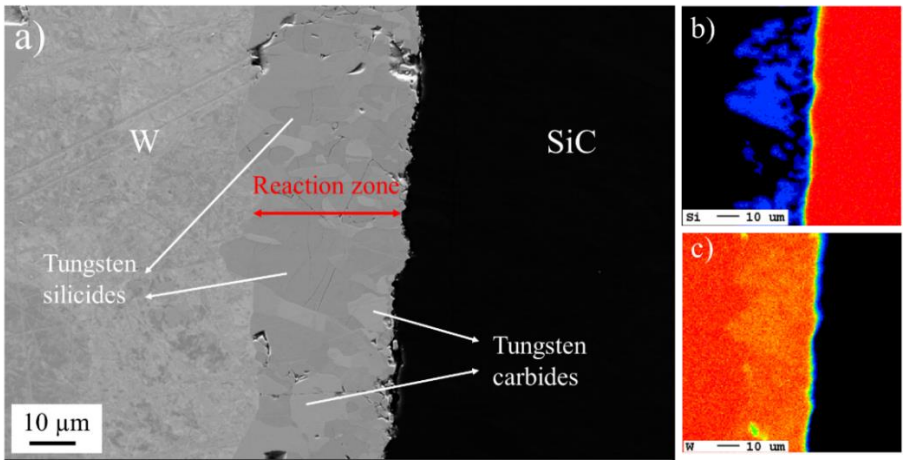

Figure 6.1 The cross-sectional SEM image with secondary electron mode (a)) and element distribution by EPMA (b) for Si; c) for W) of joined CVD-SiC and W foil without diffusion barrier at 1700 °C, 20 MPa for 1h.

The cross-sectional SEM image and EPMA results of the sample without diffusion barrier were shown in Fig.6.1. Approximately 34.5 μm average thick (measured at 5 different regions, so are the later average values) reaction layer can be observed just after 1h heat treatment according to the image, which is almost 3 times thicker than the diameter of SiC fiber (Hi-Nicalon Type S) with 12.2 μm [28]used in SiCf/W composite. It is well-known that variety of silicides (W_5Si_3 and WSi_2) and carbides (WC and W_2C) were generated after high temperature annealing in W and SiC system, and the generated ceramic phases will aggravate the embrittlement of W based material. And for SiCf/W composite, the interfacial reaction damaged the fiber and only few W remained

after sintering, which is detrimental to the mechanical property and thermal conductivity of the composite. So, an effective diffusion barrier is vitally important.

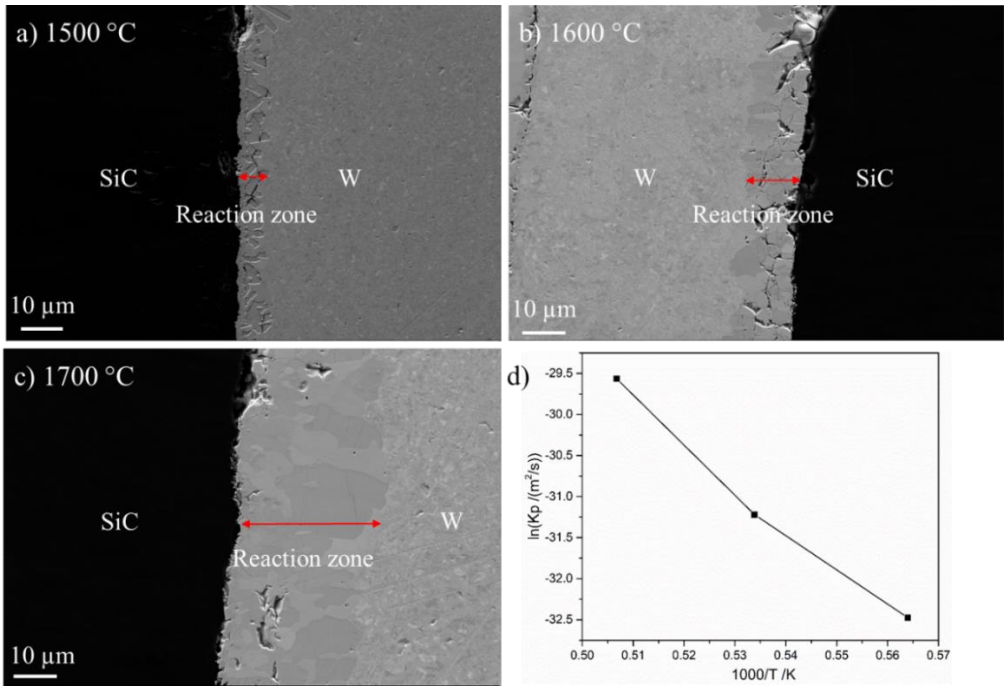

Figure 6.2 The cross-sectional SEM images of the W/SiC diffusion couple joined at different temperatures for 1h. a) 1500 °C; b) 1600 °C; c) 1700 °C; and d) is for Arrhenius plots of the parabolic rate constants of the reaction zones by the W/SiC joints as a function of the reciprocal of temperature(K).

Besides, to understand the kinetics of reactions between SiC and W, the W foil and CVD-SiC diffusion couples were joined at the same pressure and holding time with sintering composites from 1500 °C to 1700 °C, because it is easy to measure the correct thickness of reaction zone compared with the composites. Fig. 6.2 reveals the cross-sectional SEM images of W/SiC joints. The average thickness of the reaction zone measured from these images from different regions was 7.09 μm for 1500 °C, 13.31 μm for 1600 °C, and 34.5 μm for 1700 °C, respectively. To understand the reaction kinetics better, the following equations were used to calculate the growth rate constant and apparent activation energy.

$$x^2 = 2\,k_p t \tag{6.1}$$

$$k_p = k_0 \exp(-Q/RT) \tag{6.2}$$

in which x is the thickness of reaction zone, k_p is the parabolic growth rate constant, t is time equal to 3600 s for every joint, k_0 is pre-exponential factor, Q is apparent activation energy, R is gas constant 8.314 J/(mol·K), T is absolute temperature with the unit of Kelvin. The parabolic growth rate for W/SiC diffusion couples from 1773 K to 1973 K based by Eq. 6.1 are 4.19×10^{-13} m^2/s, 1.48×10^{-12} m^2/s, and 7.70×10^{-12} m^2/s, respectively. Therefore, the reaction rate increases approximately 3.5 times when the temperature was improved from 1500 °C to 1600 °C, while it is about 5 times at 1700 °C than that of 1600 °C, matching the XRD results (see Fig. 3.2), implying that the reaction rate increases with temperature. Thus the generated phases (tungsten silicides and tungsten carbides) are not appropriate as diffusion barriers in the SiC/W system. In addition, the apparent activation energy was found to be equal to 421.57 KJ/mol, and k_0 is 0.0189 m^2/s according to Fig. 6.2 d) from the Arrhenius equation of Eq. 6.2. Moreover, the calculated Q and k_0 are similar to the values reported in [13].

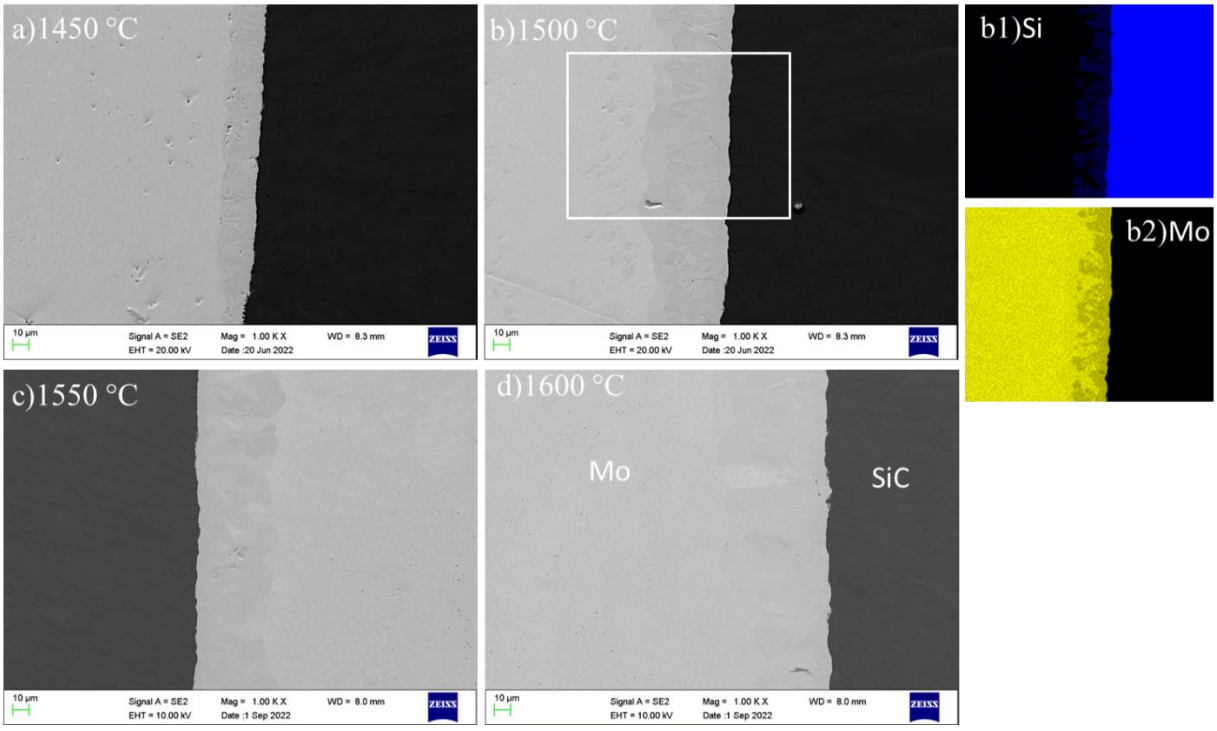

Figure 6.3 The cross-sectional images and EDS analysis of SiC and Mo joints prepared at different temperature without diffusion barrier. a) Joined at 1450 °C; b) 1500 °C; c) 1550 °C; d) 1600 °C.

The cross-sectional images of SiC/Mo joints were also displayed in Fig. 6.3 which were fabricated at different temperature from 1450 °C to 1600 °C to know about kinetics, and the EDS

mappings of diffusion couple joined at 1500 °C are shown in Fig. 6.3 b1) and b2). The equations to calculate the apparent activation energy and pre-exponential factor are the same as to that of SiC and W. The average thickness of reaction zone is 20.19 μm for 1450 °C, 49.38 μm for 1500 °C, 46.77 μm for 1550 °C, and 58.67 μm for 1600 °C, respectively. Therefore, the parabolic growth rate constant, Kp are 6.37×10^{-14} m^2/s, 3.81×10^{-13} m^2/s, 3.42×10^{-13} m^2/s, and 5.38×10^{-13} m^2/s from equation 6.1. Then the pre-exponential factor is 0.586 m^2/s and the apparent activation energy is 394.37 kJ/mol in the reaction between SiC and Mo by drawing the graph with lnKp and 1/T in Fig. 6.4. Please note here, the data from joint prepared at 1500 °C didn't be used in Fig. 6.4. Therefore, the Mo/SiC system easier reacted with each other compared with W/SiC system.

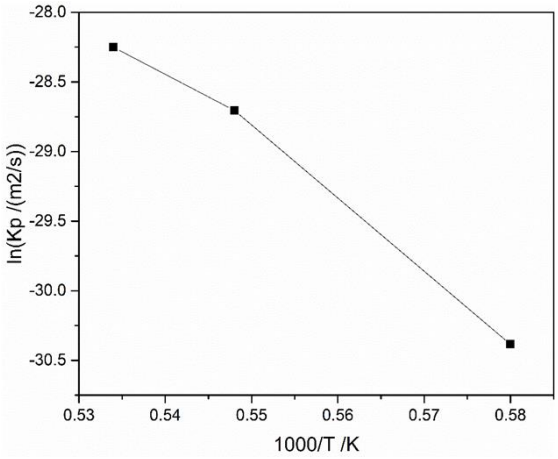

Figure 6.4 The reaction kinetic between SiC and Mo.

6.3 CVD-SiC and W foil joined with diffusion barrier

6.3.1 Oxide coatings by dipping method

XRD patterns of oxides films by dipping method are revealed in Fig. 6.5, and the results indicate that 3 kinds of oxides were indeed produced after heat treatment at 500 °C. Besides, the other unmarked peaks in Fig. 6.5 belong to CVD-SiC. And the obtained TiO_2 showed anatase structure based on XRD data. The SEM images of oxide coatings' surface and cross-section coated on SiC were shown as Fig. 6.6. It is easy to observe the cracks on the surface of ZrO_2 coating and TiO_2 coating due to the large CTE mismatch with SiC (4.7×10^{-6} /K), and the CTE of ZrO_2 and A-TiO_2 (anatase TiO_2) were 9.6×10^{-6} /K and 17.35×10^{-6} /K (c-axis) [29] at room temperature

respectively. While almost no cracks can be found in the surface of Er_2O_3 coating caused from suitable CTE value of 7.25×10^{-6} /K [30], lower than the other oxides. From images d), e) and f) in Fig. 6.6, it can be found that the thickness of oxides coating by dipping method is about 100-200 nm for 1 time.

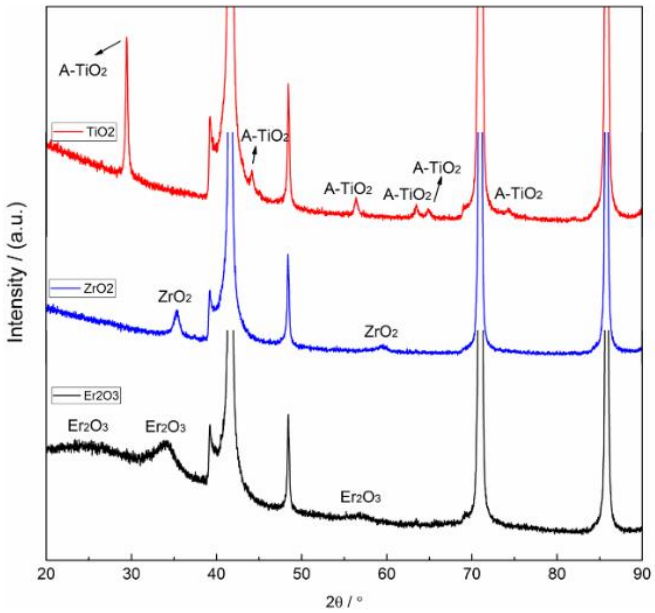

Figure 6.5 XRD patterns of oxides coating on CVD-SiC substrate after 1time dipping.

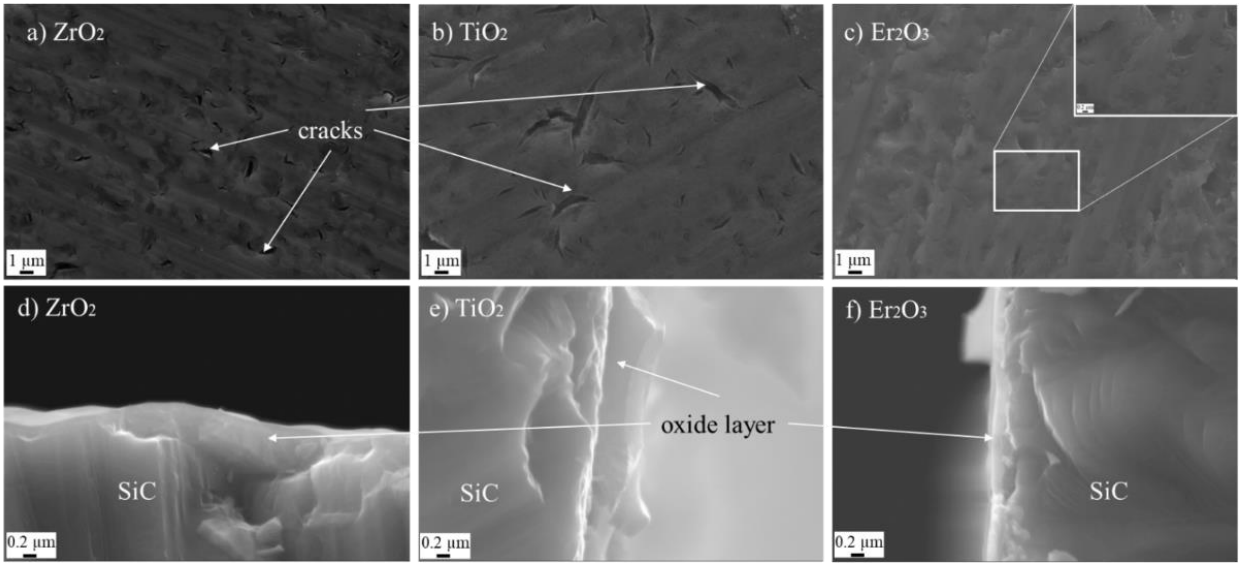

Figure 6.6 Surface and cross-sectional SEM images of oxides coating on CVD-SiC substrate after 1time dipping before joining with SE2 mode. a) and d) are the images of surface and cross-section of ZrO_2 coating by 1 time dipping respectively; b) and e) are the images of surface and cross-

section of TiO_2 coating by 1 time dipping respectively; c) and f) are the images of surface and cross-section of TiO_2 coating by 1 time dipping respectively.

Fig. 6.7 exhibits the cross-sectional images of oxides by dipping method coated CVD-SiC and W after joining. The reactions zone (RZ) between W and SiC still can be observed in specimens with oxides coating. And the depth of RZ in ZrO_2 and TiO_2 coated specimens were approximately 33 μm and 40 μm respectively, which is almost same thickness of RZ compared with joined sample without diffusion barrier (see Fig. 6.1), indicating that ZrO_2 and TiO_2 coating by dipping method were not contributed to the diffusion barrier in W and SiC system. While regarding the joined specimen with Er_2O_3 coating by dipping method, the thickness of RZ is about 28 μm, thinner than the RZ of non-interface sample and the other oxides film cases, revealing that Er_2O_3 might be suitable material for W/SiC system. Thus, the influence of Er_2O_3 coatings' thickness on whether diffusion barrier works was examined further, and the thickness was modified by the times of dipping.

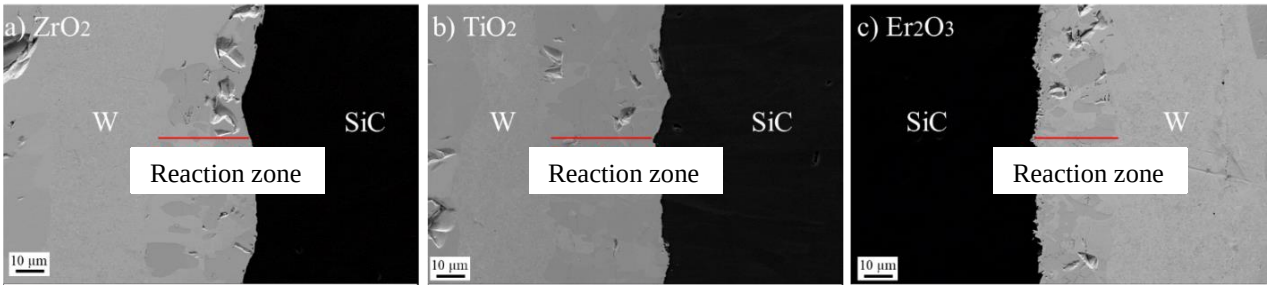

Figure 6.7 SEM images of cross-section of W joined with oxide coated SiC by 1 time dipping after 1700 °C, 20 MPa for 1 h heat treatment. a) Cross-sectional image of ZrO_2 coated SiC by dipping method joined with W; b) Cross-sectional image of A-TiO_2 coated SiC by dipping method joined with W; c) Cross-sectional image of Er_2O_3 coated SiC by dipping method joined with W.

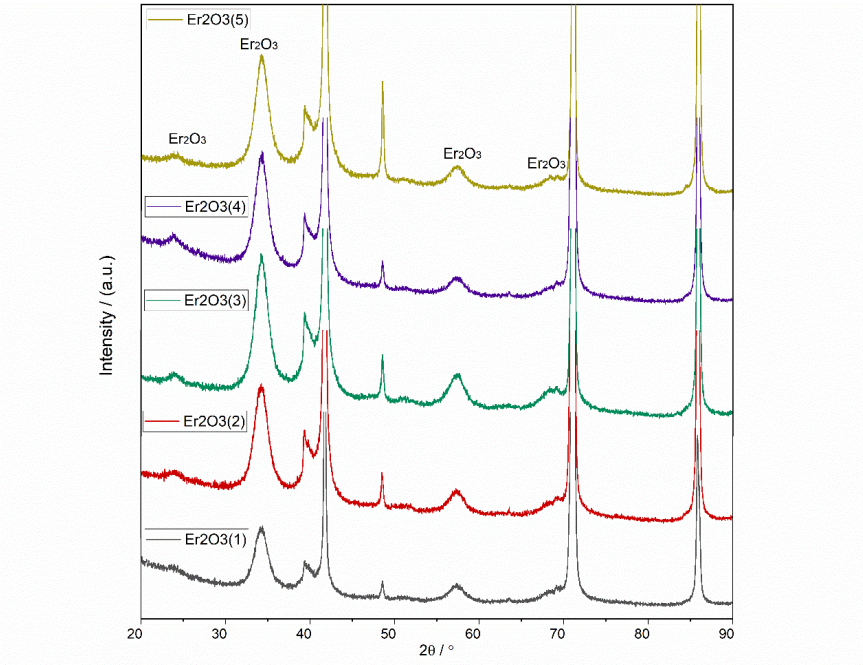

Figure 6.8 The XRD pattern of Er_2O_3 coating after 5 times dipping by precursor on CVD-SiC.

The XRD pattern of Er_2O_3 coating after 5 times dipping by precursor on CVD-SiC is displayed on Fig. 6.8. The peaks became stronger and stronger with the dipping times, indicating that the crystallinity improved after multi-dipping and heat treatment. The images of surface and cross-section of Er_2O_3 coating by multi-dipping (from 2 times to 5 times) before and after joining were shown in Fig. 6.9, manifesting the impact of thickness of diffusion barrier. The thickness of Er_2O_3 film increased from 115 nm (see Fig. 6.6 f)) by 1 time dipping to approximately 550 nm (see Fig. 6.9 d) & f)) by 5 times dipping. After 3 times dipping with about 300 nm thick Er_2O_3 layer, the depth of RZ reduced 72% for the specimen without diffusion barrier and 67% for the specimen with Er_2O_3 coating by 1 time dipping respectively. Meanwhile, only about 1.1 µm thick (thickest part) reaction layer can be found in the joined specimen with about 500 nm thick Er_2O_3 film, although there are still some cracks with about 1µm length, generating in the last time dipping period, can be observed on the surface film (see Fig. 6.9 e)).

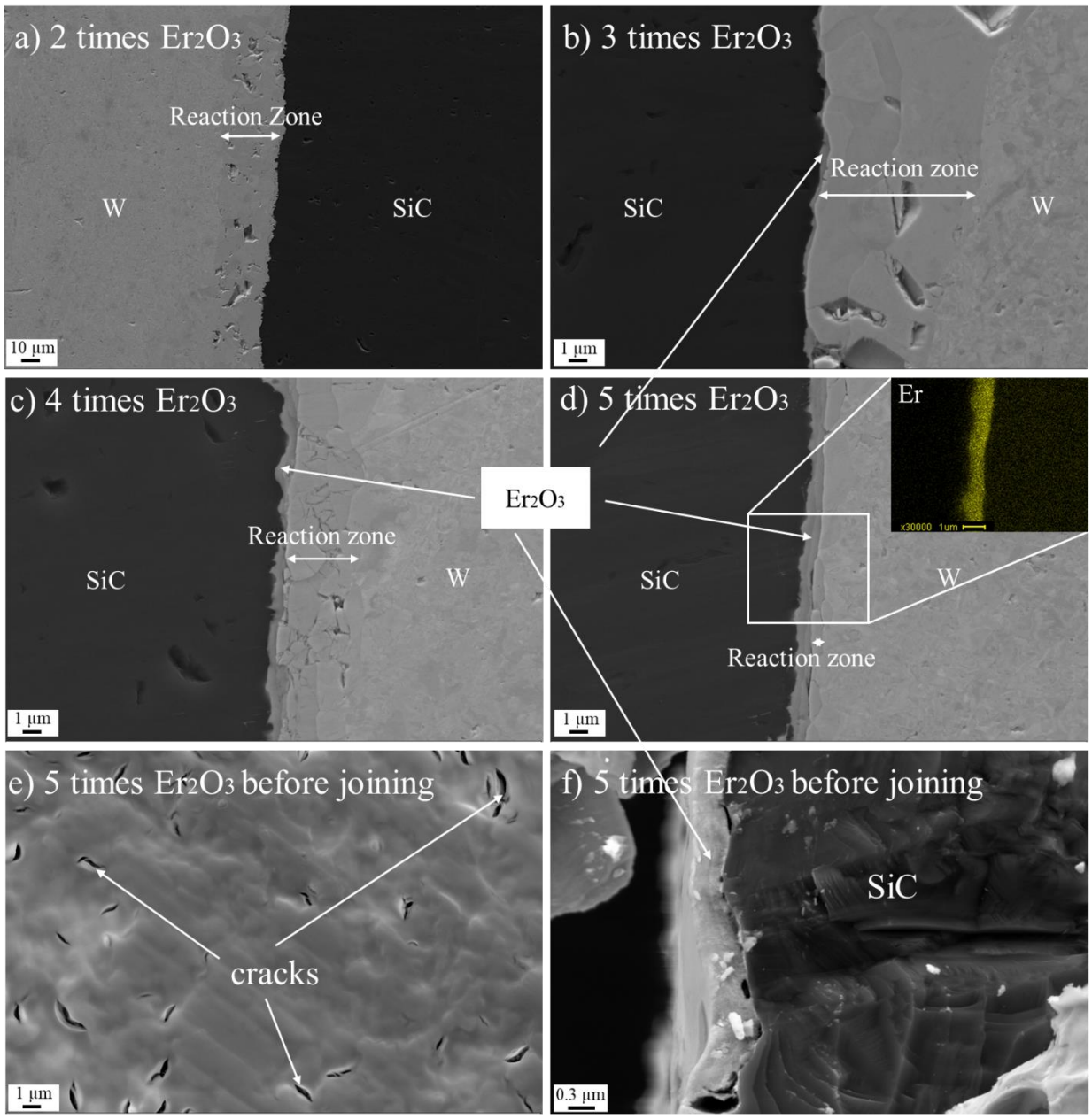

Figure 6.9 SEM images of surface and cross-section of coated CVD-SiC before and after joining with W foils. Images a) to d) are the cross-section of 2 times to Er_2O_3 coated SiC by 5 times dipping joined with W respectively; e) is surface of Er_2O_3 coating by 5 times dipping before joining; f) is cross-section of Er_2O_3 coating by 5 times dipping before joining.

6.3.2 Carbides coating by dipping method

Carbides in this work were produced by carbothermal reduction reactions between oxides and carbon black as follows.

$ZrO_2 + 3C \rightarrow ZrC + 2CO$

$TiO_2 + 3C \rightarrow TiC + 2CO$

XRD data of carbides film coated on CVD-SiC, fabricated by dipping method after annealed at 1600 °C for 2h in flowing Ar atmosphere, displayed in Fig. 6.10. The XRD results show that carbides were generated, and the peaks of carbides became strong with number of dipping, revealing that the thickness and crystallinity of carbides increased with the number of dipping, because the total heat treatment time for coating by 5 times dipping was 10 h. And longer annealing time also caused the grain growth (see Fig. 6.11).

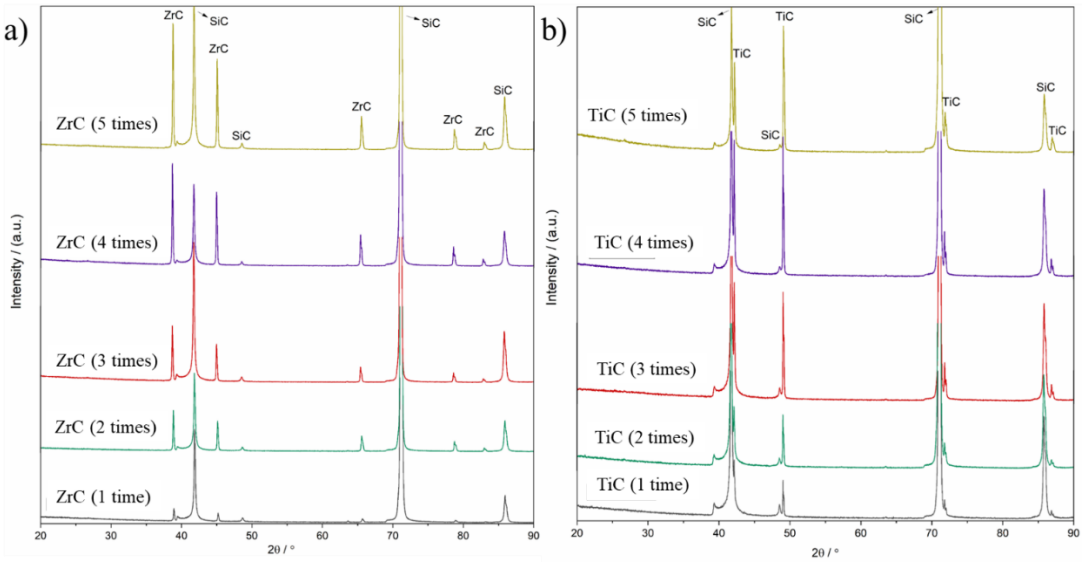

Figure 6.10 XRD patterns of carbides by dipping method before joining. a) ZrC; b) TiC.

Fig. 6.11 shows the SEM images of surface of carbide film by dipping method and cross-sectional interface of diffusion barrier coated CVD-SiC and W foil after high temperature annealing with 20 MPa pressure. The carbides films by 5 times dipping were prepared by dipping then annealed at 1600 °C for 5 times. It can be observed the thickness of ZrC was just about 323 nm, thinner than the other films by 5 times dipping, indicating that part of ZrC film peeled off. Because volume change with about 18.49 % for ZrC and 16.55 % for TiC respectively generated

during the reaction process caused by higher density of carbides ZrC (6.73 g/cm^3) and TiC (4.93 g/cm^3), than oxides (ZrO_2 (5.68 g/cm^3) and TiO_2 (4.23 g/cm^3)). Then volume variation caused thermal stress generating cracks on the surface in the procedure from oxides to carbides. Thus the larger volume changes in ZrC coating leading to the phenomenon of stripping (see Fig. 6.11 b)). However, the CTE of ZrC of 7.5 $\times 10^{-6}$ / K is less than TiC of 8.5 $\times 10^{-6}$ / K [22], implying that the volume changes caused by the difference in density dominates the procedure. And the similar phenomenon can be observed in nitrides coating by multiple dipping. However, the width of RZ in TiC coated case was almost same as the RZ in ZrC coated sample although the thickness of TiC film with around 808 nm in the relatively thicker part is more than twice of ZrC coating, implying the ZrC might be more effective than TiC as diffusion barrier in W/SiC. But ZrC produced by dipping method using carbothermic reduction is not appropriate due to film peeling off for the reason of the big difference in density. Thus it is better to minimize the steps of producing carbide film as possible, or coat the diffusion barrier on fiber directly.

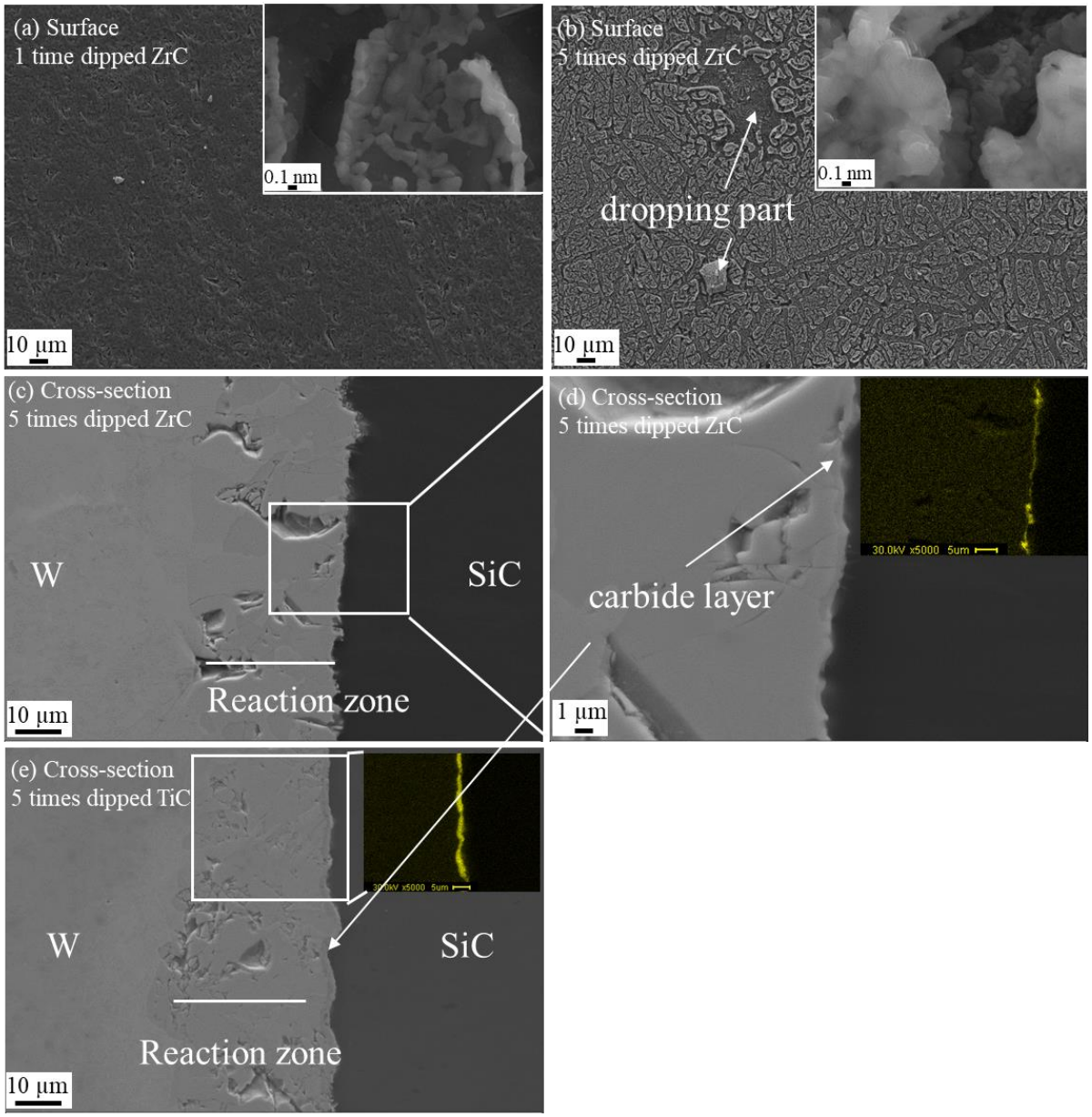

Figure 6.11 The surface and cross-sectional SEM images of carbides film by dipping method coated SiC before and after joining. a) and b) are the surface of ZrC by 1 time and 5 times dipping coated SiC before joining, c) ZrC by 5 times dipping coated SiC joined with W; d) ZrC by 5 times dipping coated SiC joined with W with larger magnification; e) TiC coated SiC by 5 times dipping method joined with W.

6.3.3 Nitrides coating by dipping method

XRD patterns of nitrides coating produced by dipping several times and annealing at 1400 °C for 2h in flowing N_2 atmosphere are shown in Fig. 6.12. The results show nitrides can be produced by annealing in N_2. Moreover, no other reaction products were identified after heat treatment. And similar to carbides coating by multi-dipping, the intensity of nitrides' peaks became stronger with the dipping times, suggesting that nitrides coating by 5 times dipping have better crystallinity, similar with the carbide cases.

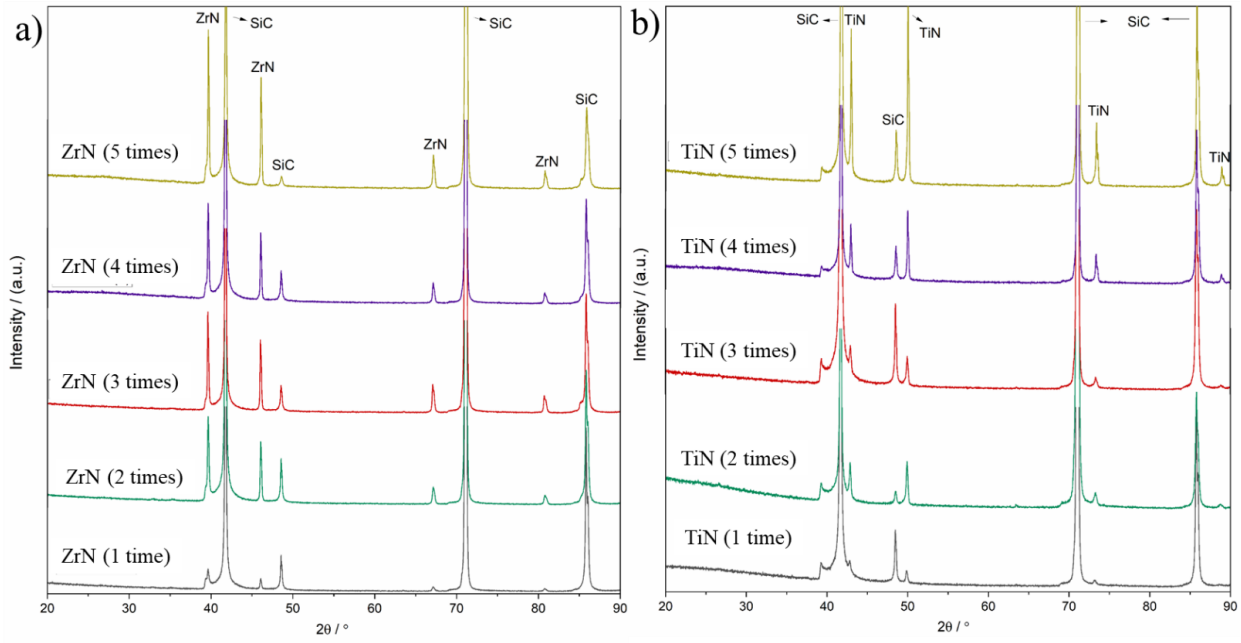

Figure 6.12 XRD patterns of nitrides by dipping method before joining. a) ZrN; b) TiN.

Fig. 6.13 displays the surface of nitrides film by dipping method before joining and the cross-sectional images of nitrides coated SiC by 5 times dipping joined with W foil. It is easy to recognize the grain growth after several times dipping, and the grain size in the 5 times TiN film is about 250 nm, which is approximately 3 times compared with the 1 time dipping case with the grain size lower than 100 nm, matching with the XRD results and similar with the carbide case. And after joined with W at high temperature, the thickness of RZ in TiN coating prepared by 5 times dipping case is about 13.6 μm, much lower than the specimen without diffusion barrier with 33 μm RZ and ZrN coating specimen by 5 times dipping method, although the higher CTE (9.9 $\times 10^{-6}$ / K) and larger volume change (about 27.6 %) for TiN compared to the ZrN for CTE of 7.8

$\times 10^{-6}$ / K [22] and volume change of 24.8 % when oxides changed to nitrides. However, the width of RZ in TiN diffusion barrier by dipping method is almost 10 times thick compared with Er_2O_3 coated specimen (see Fig. 6.9 d) & Fig. 6.13 c)), which suggests that Er_2O_3 exhibits the most efficient diffusion barrier for coatings prepared by dipping method.

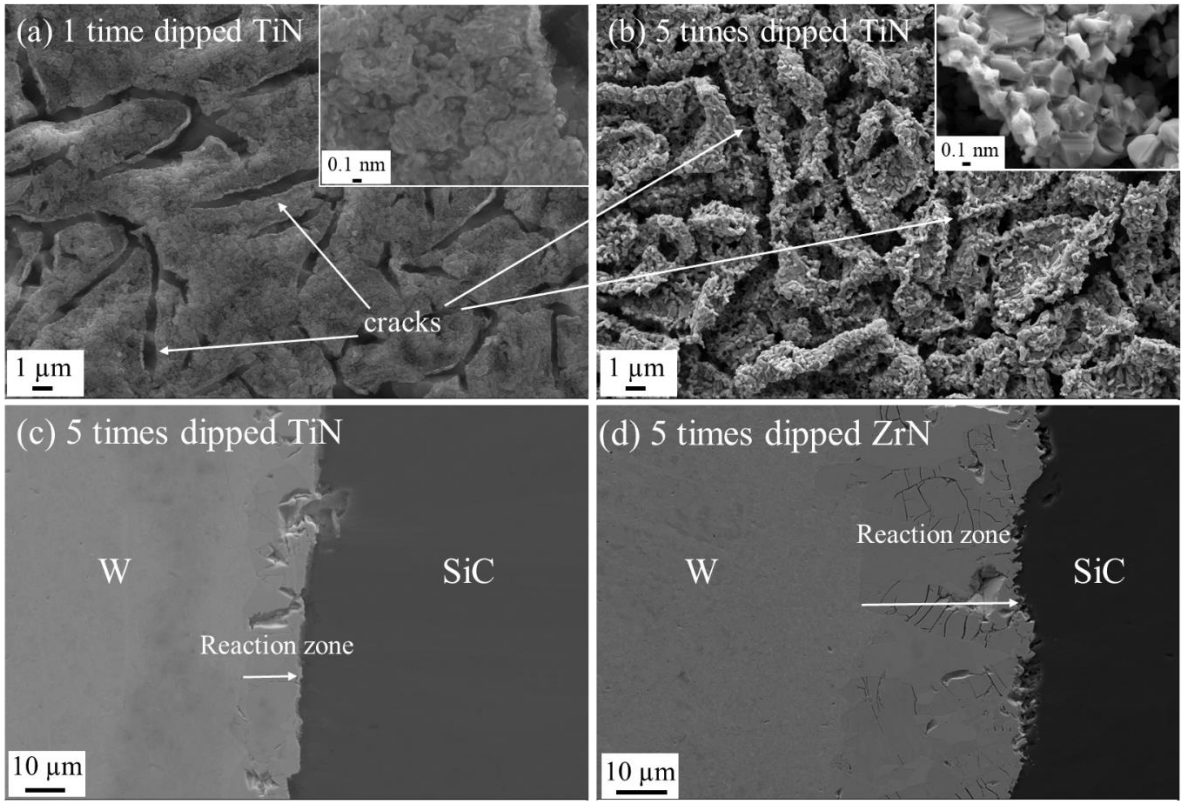

Figure 6.13 The surface and cross-sectional SEM images of nitride coated SiC by dipping method before and after joined with W foil at 1700 °C with 20 MPa pressure. a) the surface of TiN on CVD-SiC by 1 time dipping with different magnifications; b) the surface of TiN film by 5 times dipping; c) the cross-sectional of TiN coated SiC by 5 times dipping joined with W; d) the cross-sectional of ZrN coated SiC by 5 times dipping joined with W.

6.3.4 Coating by sputtering method

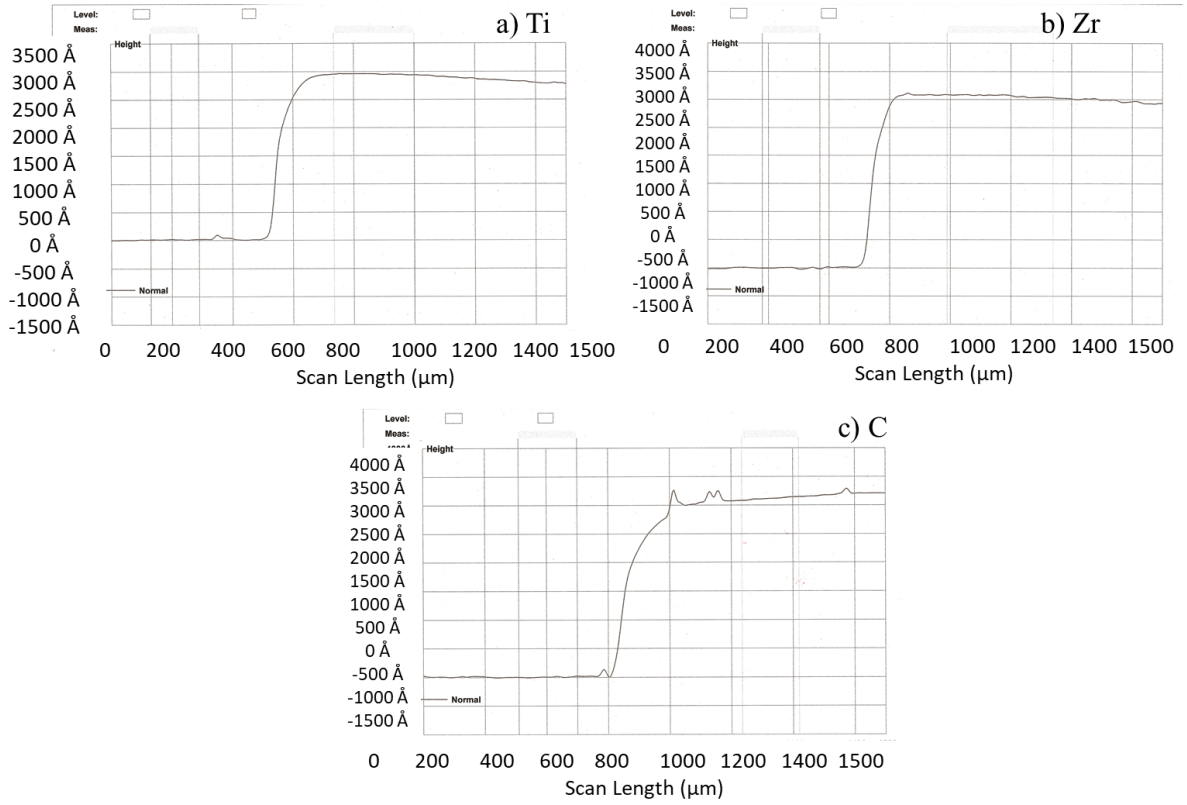

Figure 6.14 The thickness of sputtered films by KLA tencor profiler (by Osaka Research Institute of Industrial Science and Technology). a) Ti; b) Zr; c) C.

The ZrN and TiN produced by sputtering method, acting as diffusion barrier in SiC and W system, were also studied. The sputtered nitrides coating in this work were from the metal Zr or Ti film annealed at the same condition with the nitride coating by dipping method, namely 1400 °C in N_2 atmosphere for 2 h. And carbon here is to protect SiC from Ti and Zr metal during the nitrides producing process. The thickness for all sputtered films were about 300 nm, measured by KLA tencor profiler (Osaka Research Institute of Industrial Science and Technology), shown in Fig. 6.14. In addition, Fig. 6.15 illustrates the SEM image of surface and cross-section of the sputtered metal films before annealing. The thickness of C and metal layer are about 300 nm respectively. And the dense metal coatings were fabricated by sputtering method according to the SEM images of surface and cross-section.

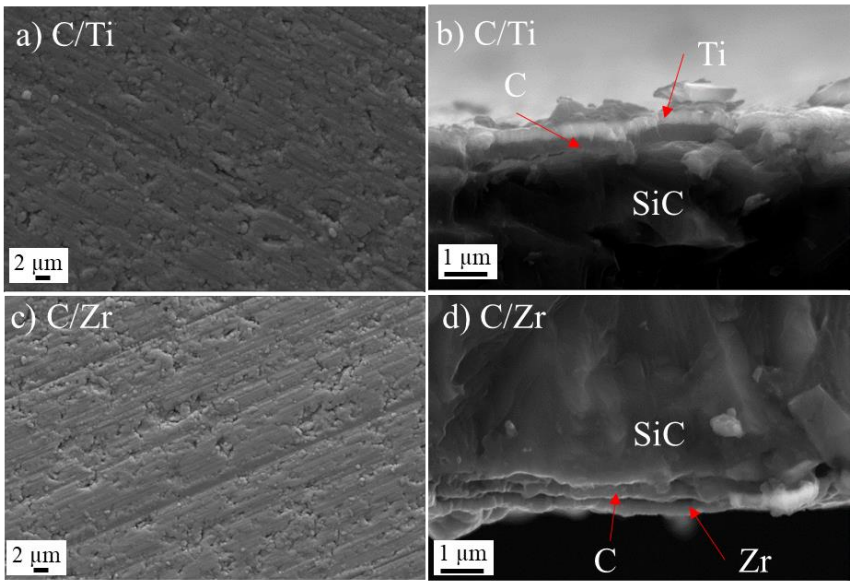

Figure 6.15 SEM images of surface and cross-section of sputtered coating with SE2 mode before heat treatment. a) and b) are the surface and cross-sectional image of sputtered C/Ti coating respectively; c) and d) are the surface and cross-sectional image of sputtered C/Zr coating respectively.

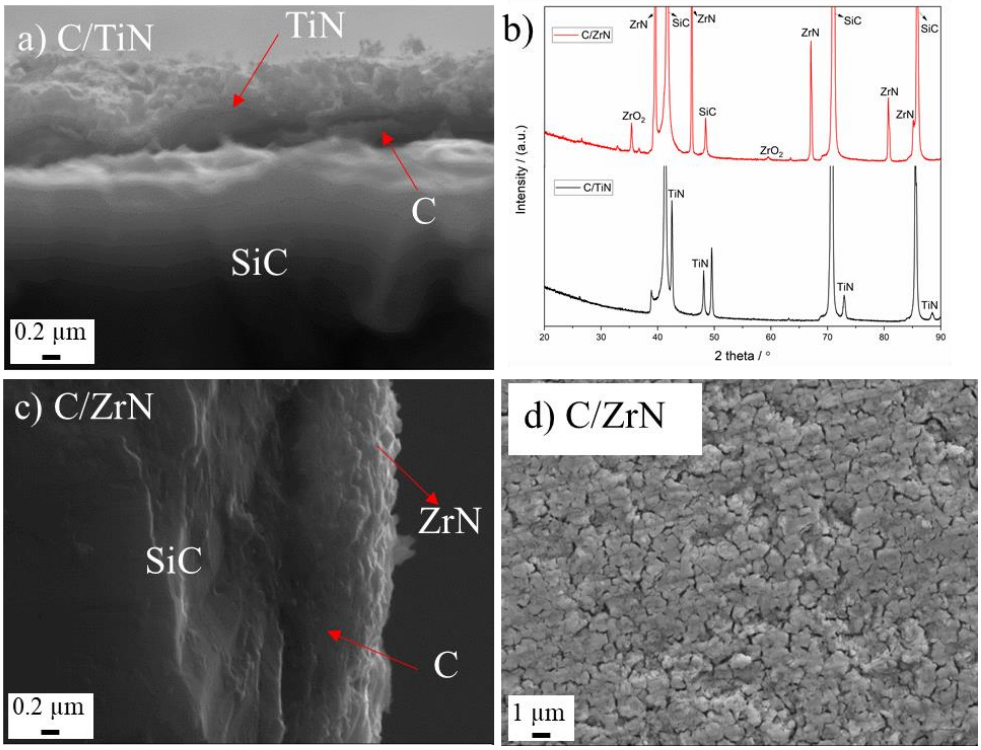

Figure 6.16 SEM images with SE2 mode of surface and cross-section of sputtered coating and XRD patterns after 1400 °C heat treatment at N_2 atmosphere. a) the cross-sectional image of C/TiN coating; b) XRD patterns of sputtered coating after 1400 °C heat treatment; c) the cross-sectional image of C/ZrN coating; d) the surface of C/ZrN coating.

The surface and cross-sectional SEM images of sputtered metal films after 1400 °C heat treatment are displayed in Fig. 6.16. The nitrides were indeed generated by annealing in N_2 in terms of the XRD results (see Fig. 6.16 b)). And some microcracks, causing by the volume change in the annealing period and CTE mismatch between C and nitrides, can be observed on the surface, but the length and width of created cracks on the sputtered coating is much smaller than the film by dipping method (see Fig. 6.13 a), b) and Fig. 6.16 d)). And TiN coating's surface, were not shown here, has the similar microstructure with ZrN coating.

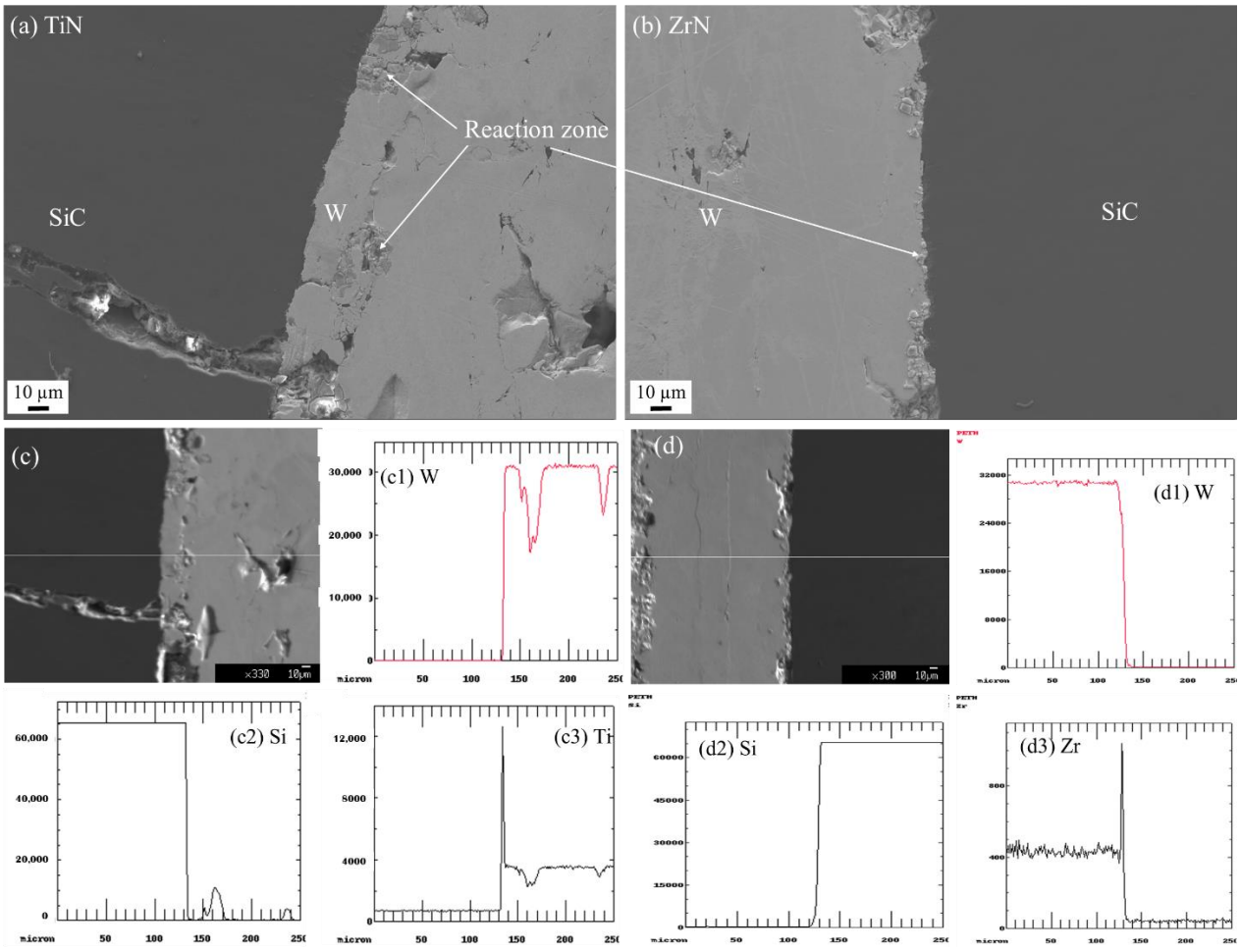

Figure 6.17 SEM images and EPMA results of cross-section of sputtered coated SiC joined with W foils. a) cross-sectional SEM images of TiN coated SiC and W; b) cross-sectional SEM images of ZrN coated SiC and W; c) line scan results of TiN coated SiC joined with W by EPMA; d) line scan results of ZrN coated SiC joined with W by EPMA.

The joining condition is the same as the specimens by dipping method, and the evaluated results of sputtered nitrides as diffusion barrier are shown in Fig. 6.17. The thickness of RZ for both nitrides coating was much thinner for the comparison with the specimen without interface coating and films by dipping method coated specimen (except Er_2O_3 coating by dipping method), although some cracks can be noticed on the surface of sputtered nitrides coating, implying the nitrides fabricated by sputtering method were good candidates for diffusion barrier application for SiC/W system, while the nitrides by dipping method did not work well. A phenomenon need to be noticed here is that the reaction zone in TiN coated specimen identified by SEM and EPMA was located in the inner part of W, rather than the junction area (see Fig 6.17 a) & c)). Because cracks existed in the W foil, and the Si and C atom diffuse easily through these cracks. Then the stress generated after reaction, which caused the cracks propagation further, damaging the mechanical property and thermal conductivity of SiCf/W composites.

6.3.5 Discussion about possible diffusion barrier in SiC/W system

Table 6.1. The results of SiC/W joints with different diffusion barrier coatings joined at 1700 °C for 1 h.

Coating	**Er_2O_3**	**ZrO_2**	**TiO_2**	**ZrC**	**TiC**	**ZrN**	**TiN**
dipping	√	×	×	×	×	×	×
sputtering	----	----	----	----	----	√	√

Here, √ means a good result. × means that coatings cannot work. ---- means that coatings don't be evaluated in this work.

The summary results were described in Table 6.1. The carbides and nitrides coating fabricated by dipping method from the oxides film by dipping method annealed at high temperature (1600 °C for carbides, and 1400 °C for nitrides) induced larger thermal stress leading to more and larger cracks due to the high-temperature processing compared with the temperature

producing oxides film (500 °C). Additionally, large volume shrinkage caused by phase transition creates the further occurrence of larger cracks, revealing the nitrides and carbides by dipping method were not appropriate as diffusion barriers. Thus, the carbides and nitrides film by dipping eventually failed. On the other hand, the sputtered nitrides filmed by annealing metals in N_2 atmosphere can successfully impede the reaction. The different methods (dipping and sputtering) also caused the varying results. In addition, the joining process (SPS [5] and hot-press) has an effect on whether diffusion barriers work even at the same temperature resulting from the holding time of 3 min for SPS in [5] and 1 h for the hot press in this work. Shorter holding times can reduce the thickness of the reaction zone. Thus, whether the carbides are suitable needs to be further studied, although the films by dipping method cannot work well.

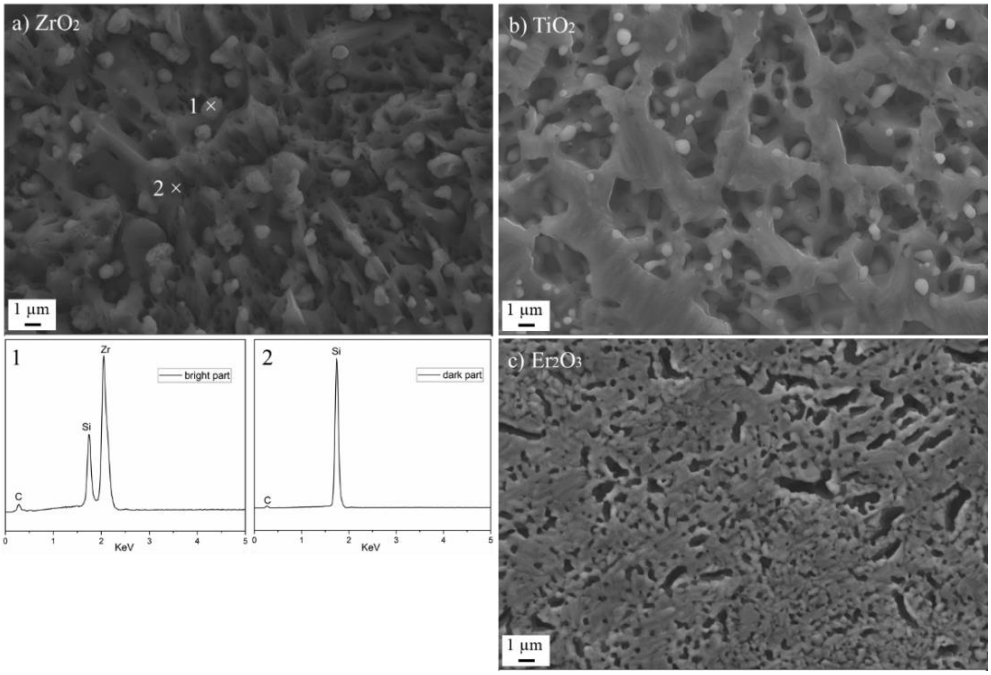

Figure 6.18 SEM images and spot scan of oxides coating by dipping method after 1600 °C, 2h annealing. a) ZrO_2; b) TiO_2; and c) Er_2O_3.

The Er_2O_3 show the best results among oxides coatings. In addition, to understand the reaction between SiC and the oxide coating directly, the oxide coatings by dipping were annealed at 1600 °C without the W foils, and the results are revealed in Fig. 6.18. The significant reactions were observed in ZrO_2 and TiO_2, and the surface of the ZrO_2 coating and TiO_2 coating became very rough and uneven, even parts of the zone were directly exposed to W. From the results of the spot scan in the ZrO_2-coated SiC in Fig. 6.18, the peak of Zr was identified just in the bright part,

namely area 1. Thus, ZrC was formed in this zone after high-temperature annealing. The dark zone is SiC rich region. Although for the Er_2O_3 coating by dipping, only grain growth can be noticed, and the Er_2O_3 film by dipping still exhibited relatively uniform in contrast with the others. Thus, the Er_2O_3 layer as diffusion barriers in the composites merits further study. However, ZrO_2 and TiO_2 cannot be used as the interface in the SiC_f/W composites for the damage of fiber due to the reaction between oxides and SiC.

Therefore, the material of Er_2O_3 is the most potential diffusion barrier in SiC and W system according to these results. While considering as the diffusion barrier in a composite, the film to produced using the liquid precursor by dipping method is easy to coat on the fiber in fiber tow compared with the sputtering method. Moreover, for a composite, the space in fiber bundle is around 1 μm, thus, the thickness of interface with 500 nm should be appropriate. The Er_2O_3 by multi-dipping might be the better candidate to fabricate the diffusion barrier based on the results, because the used liquid precursor can fill in the cracks formed in previous coating (see Fig. 6.19), so the observed cracks on the coating by multi-dipping should generate at the last time dipping. And the thickness of diffusion barrier can also be controlled by the times of dipping. Besides, high crystalline coating can be identified on multi-dipping specimen.

Figure 6.19 The schematic diagram of coating by multi-dipping on the substrate (Colors indicate different dipping times).

6.4 CVD-SiC/Er_2O_3/Mo joint

From the results between SiC/W diffusion couple, we found the most possible diffusion barrier is Er_2O_3 for dipping method. Therefore, Er_2O_3 was also used in CVD-SiC and Mo joint from the candidate diffusion barriers to lower the reaction rate like W/SiC.

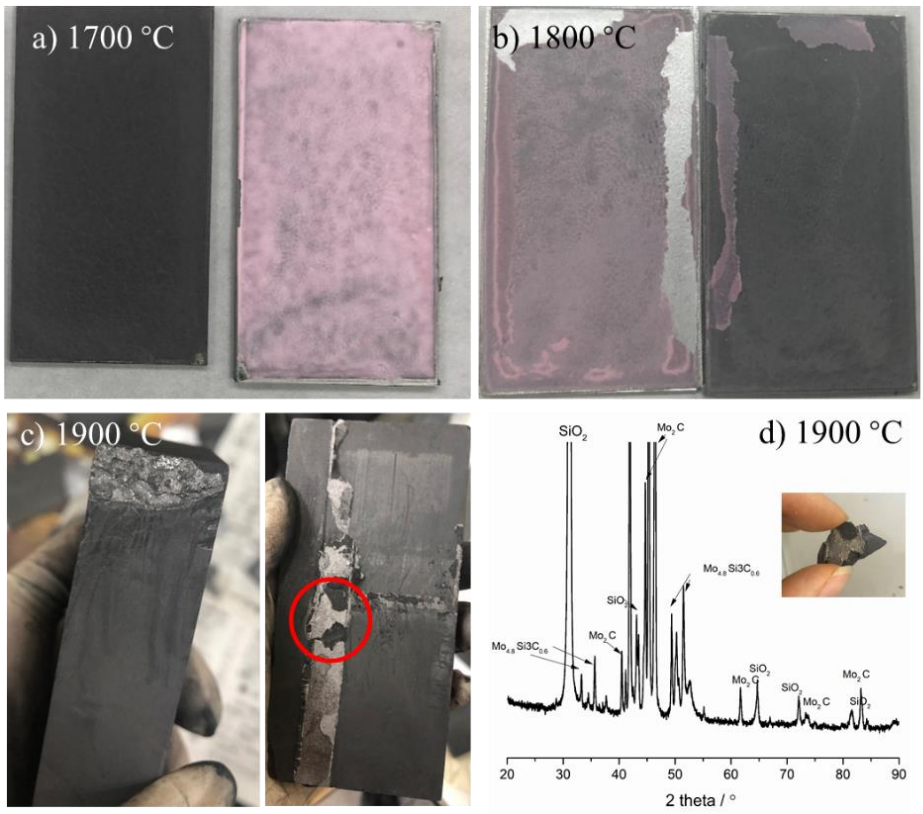

Figure 6.20 The results of SiC and Mo joints prepared at different temperature. a) 1700 °C; b) 1800 °C; c) The graphite die after joining SiC and Mo at 1900 °C; d) The XRD pattern of SiC/Mo joined at 1900 °C and the tested area.

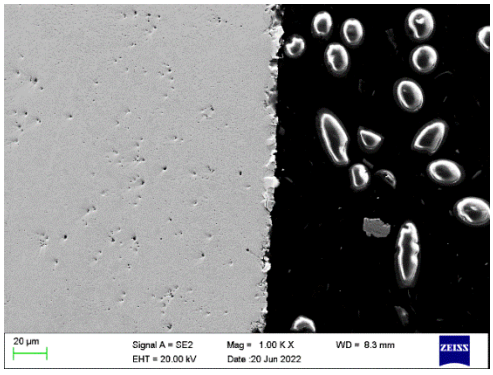

Figure 6.21 The SEM images of deboned Mo plate at 1700 °C.

The Er_2O_3 coated from the slurry, which same as slurry for method without power sheet changed W powders to Er_2O_3 powders with 30 wt%. Then, the SiC plate was dipped in slurry. Subsequently, the coated SiC plates were treated at 1700 °C for 1h without pressure to remove PVB and sinter Er_2O_3 powders. Afterwards, the SiC with sintered Er_2O_3 joined with Mo plate at

different temperature from 1700 °C to 1900 °C with 20 MPa pressure for 1h revealed in Fig. 6.20. The SiC and Mo deboned in the Er_2O_3 coating after 1700 °C and 1800 °C heat treatment. However, severe reaction even liquid phase can be found when temperature was improved to 1900 °C (see Fig. 6.20 c)). The XRD of such liquid phase was examined and the result is shown in Fig. 6.20 d). In addition, the investigated area was marked by the red circle. The result shows the liquid phase is SiO_2. In addition, other molybdenum silisides and carbides are also identified. The deboned Mo plate heat treated at 1700 °C is shown in Fig. 6.21. No reaction zone can be recognized, so Er_2O_3 can work until 1800 °C.

a) Er_2O_3-SiC

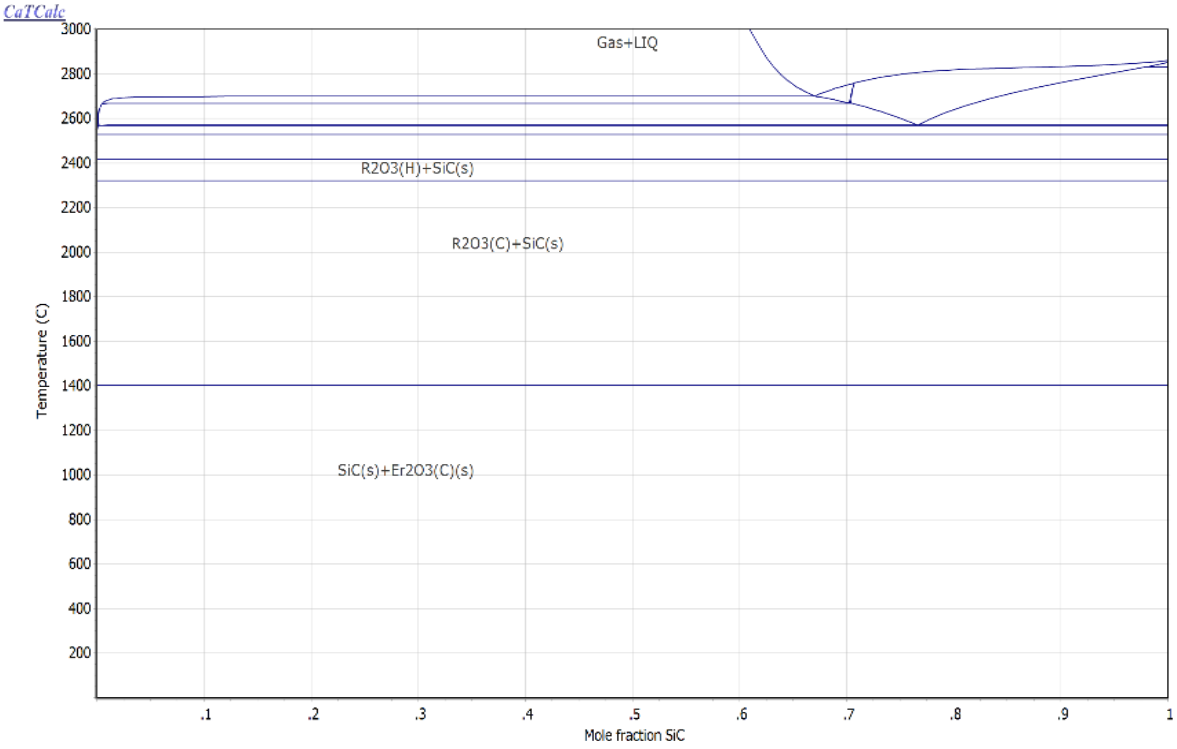

b) Er_2O_3-Mo

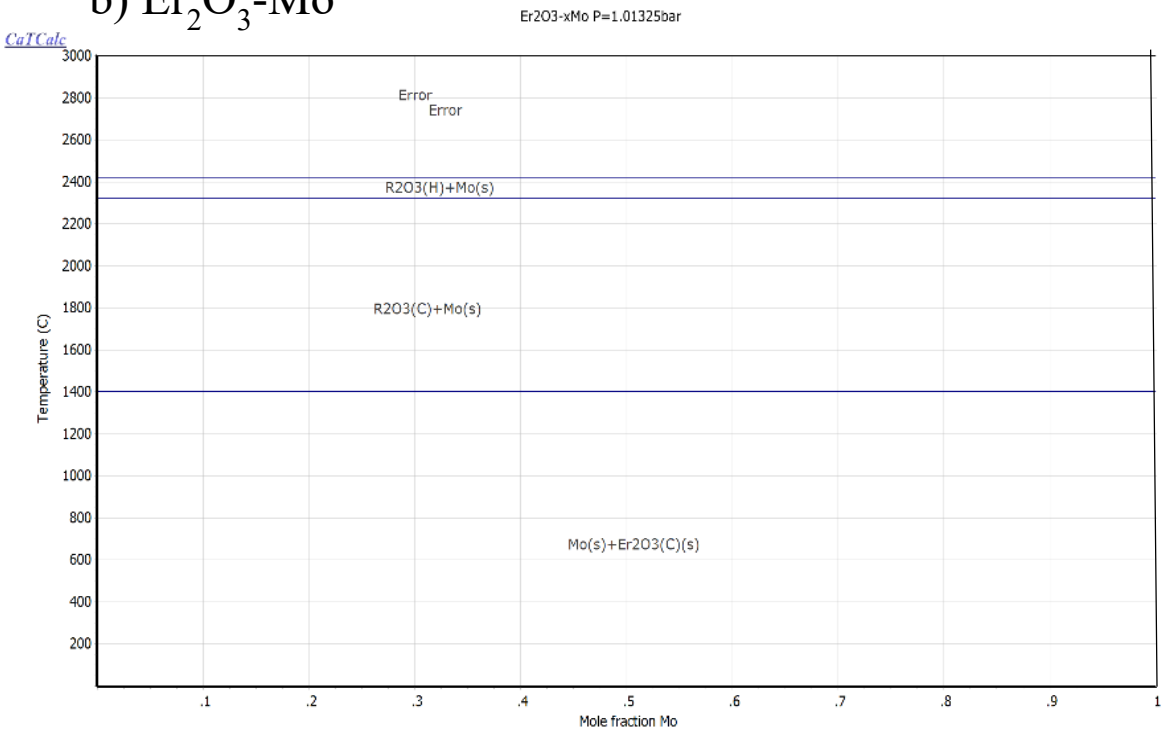

c) SiC-Mo

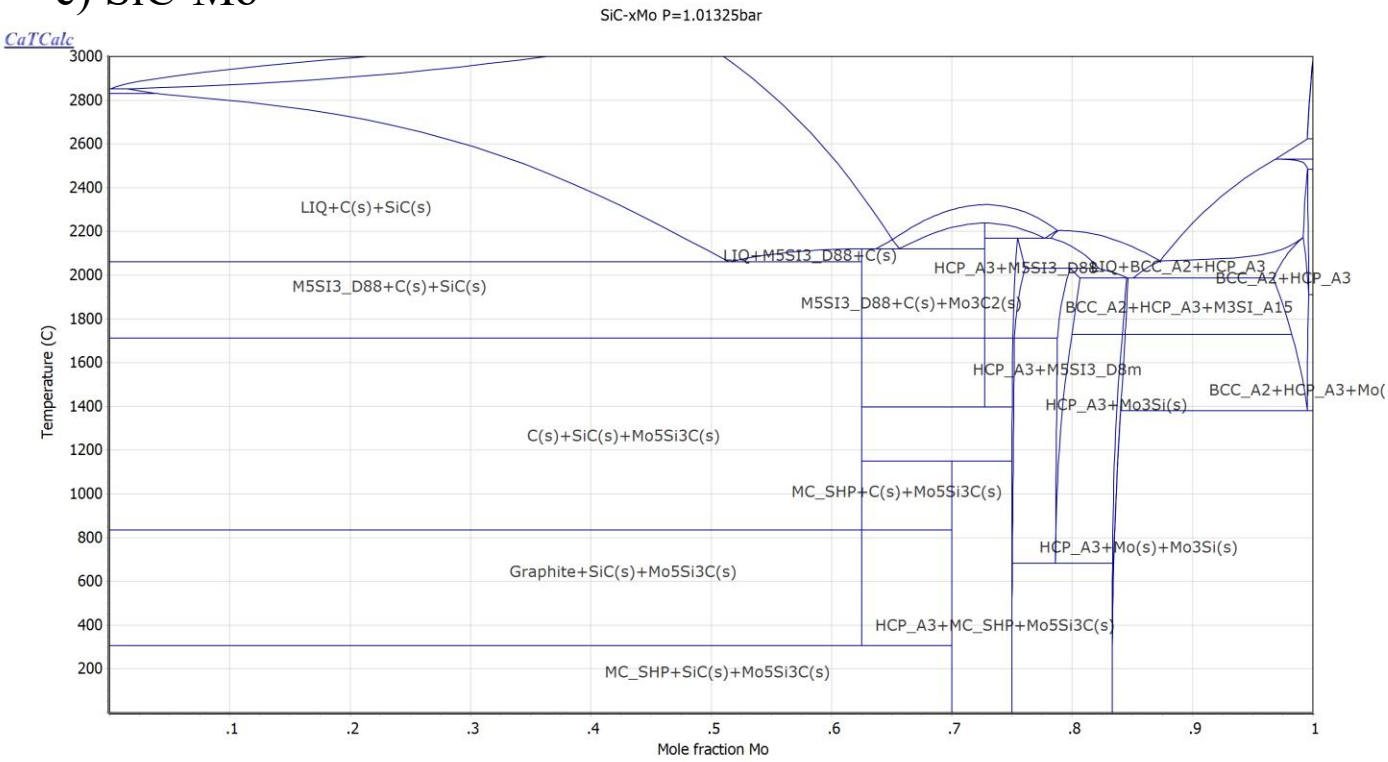

Figure 6.22 The binary phase diagram of a) Er_2O_3-SiC, b) Er_2O_3-Mo, and c) SiC-Mo until 3000 °C.

To understand the liquid phase caused by the reaction, the binary phase diagrams of Er_2O_3, Mo and SiC with each other by CatCalSE are displayed in Fig. 6.22. While no SiO_2 generate at 1900 °C based on the Er_2O_3-SiC and SiC-Mo binary phase diagram. Therefore, we need to refer to the ternary phase diagram, which is exhibited in Fig. 6.23. According to the ternary phase diagram at 2000 °C, liquid SiO_2 will be generated. In this work, the SiO_2 was found when the joining temperature is 1900 °C. Moreover, the melting point of SiO_2 is 1710 °C lower than the heat treatment temperature of 1900 °C. Therefore, Er_2O_3 diffusion barrier in SiC/Mo system must be perfect coating without cracks to hinder the existence of liquid phase of SiO_2.

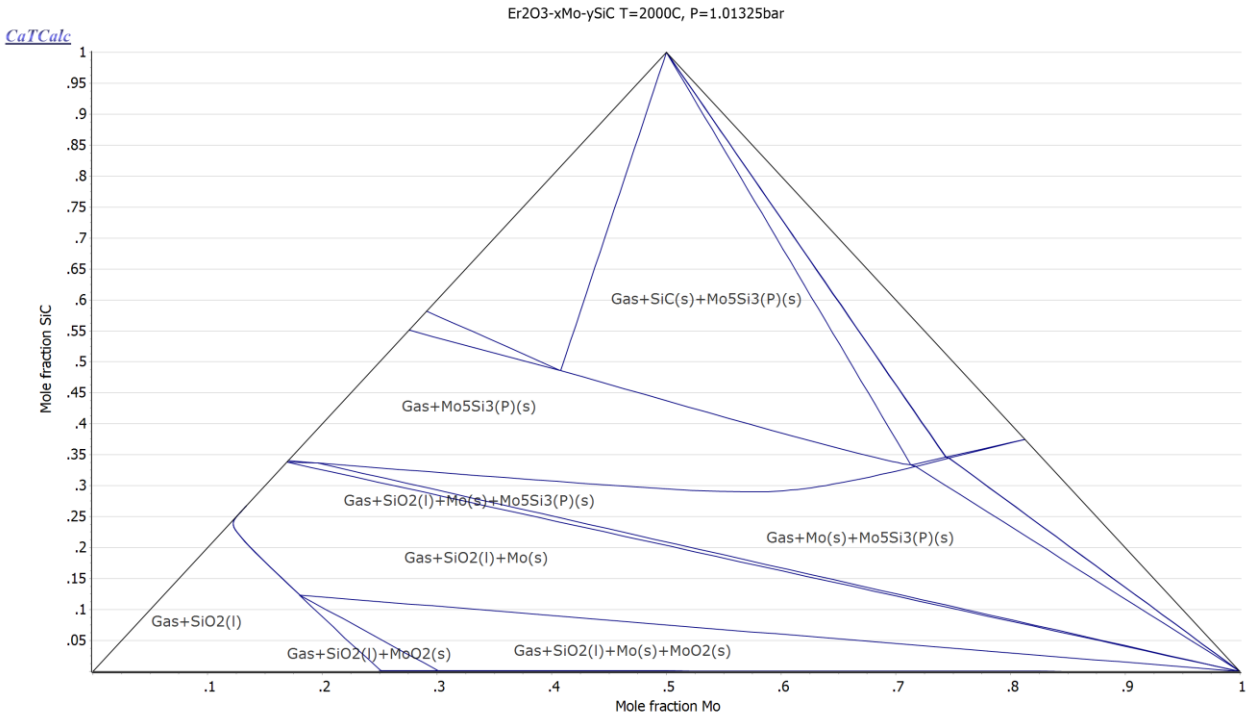

Figure 6.23 The ternary phase diagram of Er_2O_3-Mo-SiC at 2000 °C.

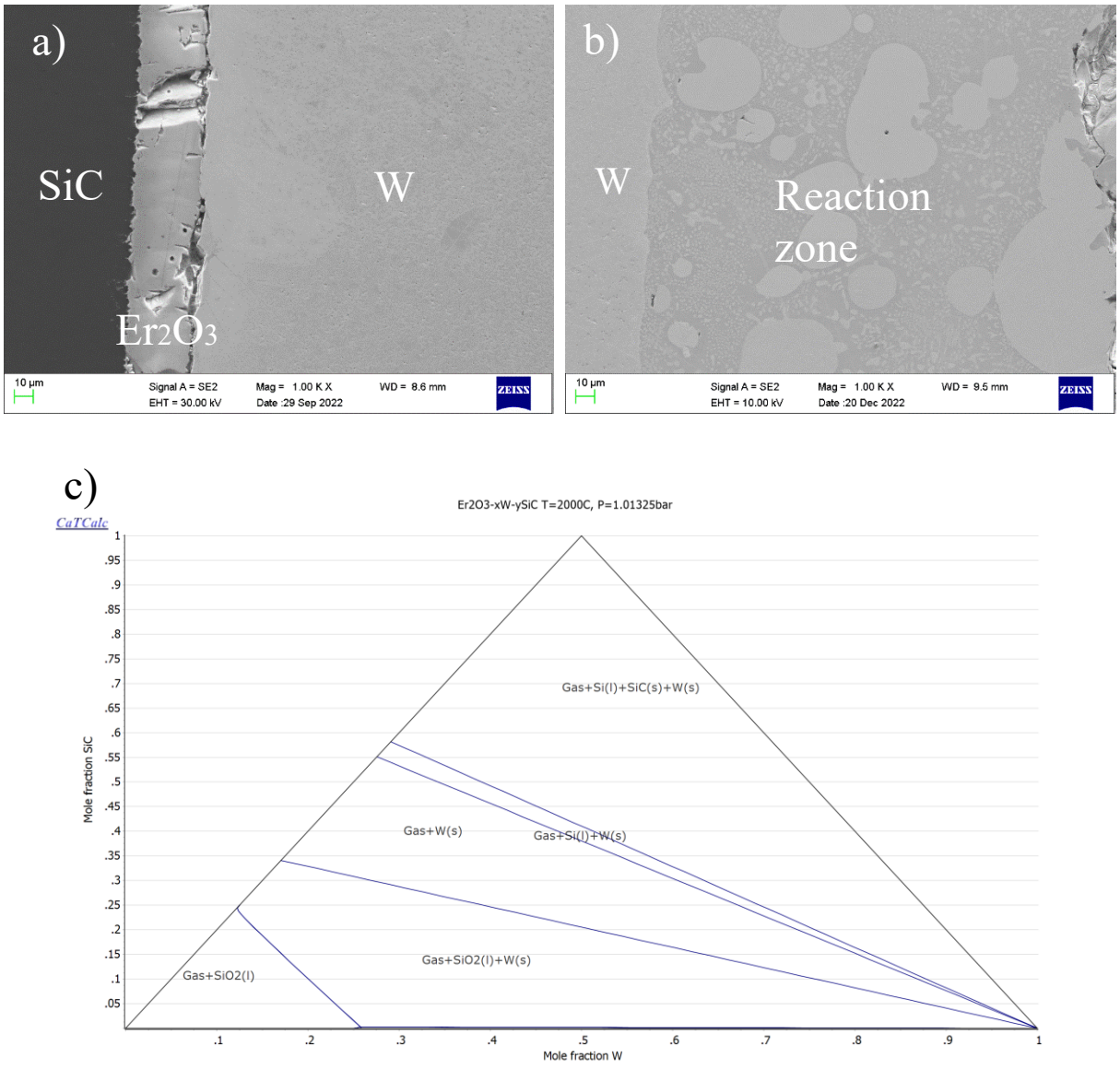

Figure 6.24 The SEM images of SiC/ Er_2O_3/SiC joined at 1950 °C and the ternary phase diagram of Er_2O_3-W-SiC at 2000 °C.

Liquid phase was also found in W/ Er_2O_3/SiC system joined at 1950 °C (see Fig. 6.24 b)), matched with the ternary phase diagram of Er_2O_3-W-SiC system, which caused from the cracks on the Er_2O_3 coating. While, Er_2O_3 without cracks area can protect SiC and W well, and the joined area without reaction can be observed after heat treatment at 1950 °C when the thickness of Er_2O_3 is 29.4 µm. Therefore, it is necessary to fabricate the integral coating without defects.

6.5 SiC fiber reinforced metals with diffusion barrier sintered at 1700 °C

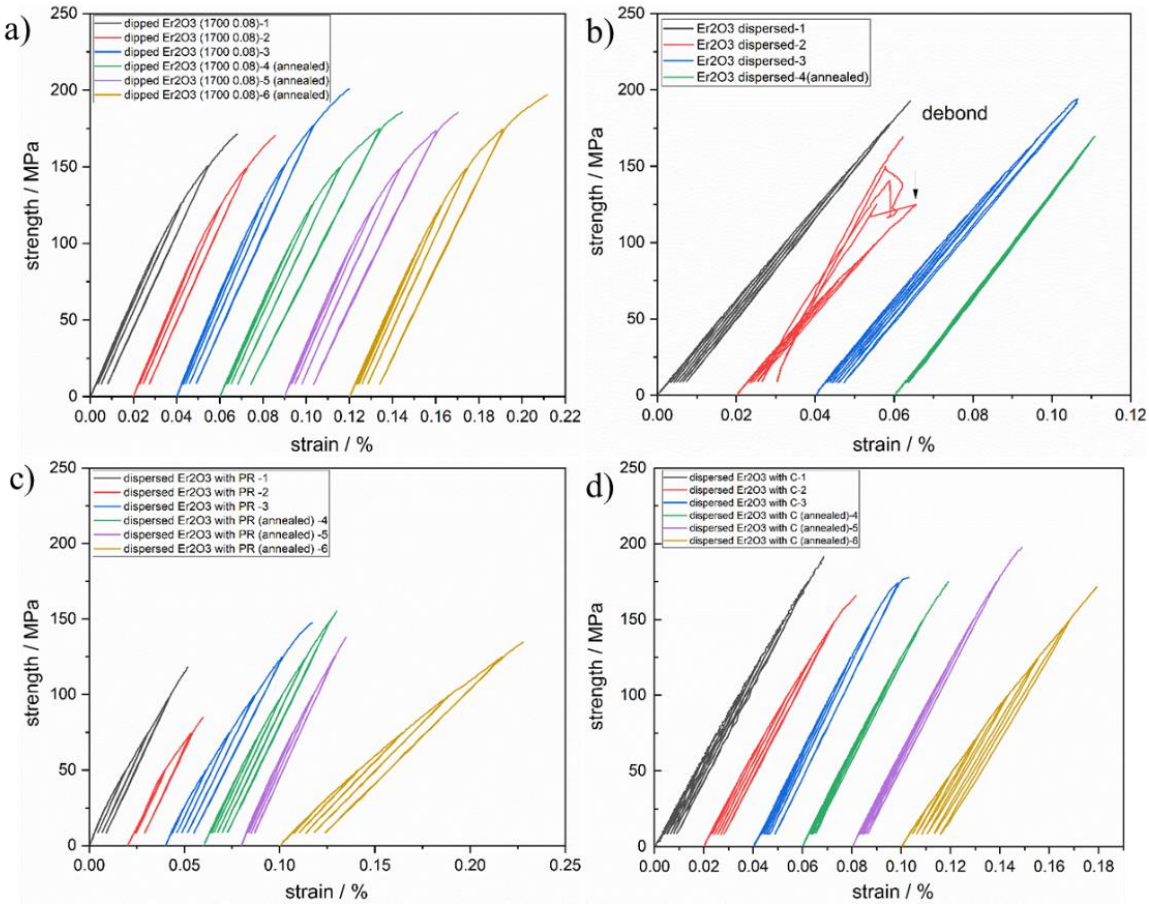

Figure 6.25 The mechanical property of unidirectional SiC fiber reinforced W composite with Er_2O_3. a) Er_2O_3 by dipping method; b) Er_2O_3 from slurry; c) C from phenolic resin/ then Er_2O_3 slurry; d) Er_2O_3 slurry with C powder.

The composites with Er_2O_3 ad diffusion barrier were fabricated at 1700 °C with foils, and the tensile test results are revealed in Fig. 6.25. The composites with Er_2O_3 prepared by dipping method shows the good mechanical property, and the ultimate tensile strength (UTS) is 180.3 ± 15.6 MPa and 190.0 ± 6.3 MPa before and after annealing. The specimen with Er_2O_3 by dispersed from slurry with Er_2O_3 powder display high strength of 186.3 ± 15.2 MPa without annealing while lack of pseudo ductility. Materials with C was prepared from phenolic resin (PR) firstly by cured at 200 °C, then Er_2O_3 slurry was poured on the PR coated fiber. Composites with two layer diffusion barriers exhibits better pseudo ductile behavior compared with others. However, the strength is 116.6 ± 32.0 MPa and 143.2 ± 19.6 MPa with or without heat treatment lower than

other composites with diffusion barrier. In addition, error of tensile test strength in the composites with PR/Er_2O_3 is largest due to the nonuniform PR/ Er_2O_3 layers. To solve this problem, another easier way was used to prepare the diffusion barrier, which is the C and Er_2O_3 powder were dispersed in slurry together. The strength was improved of 179.4 ± 12.1 MPa and 181.9 ± 14.2 MPa before and after annealing compared with specimen with 2 layer coatings, while the ductility reduced.

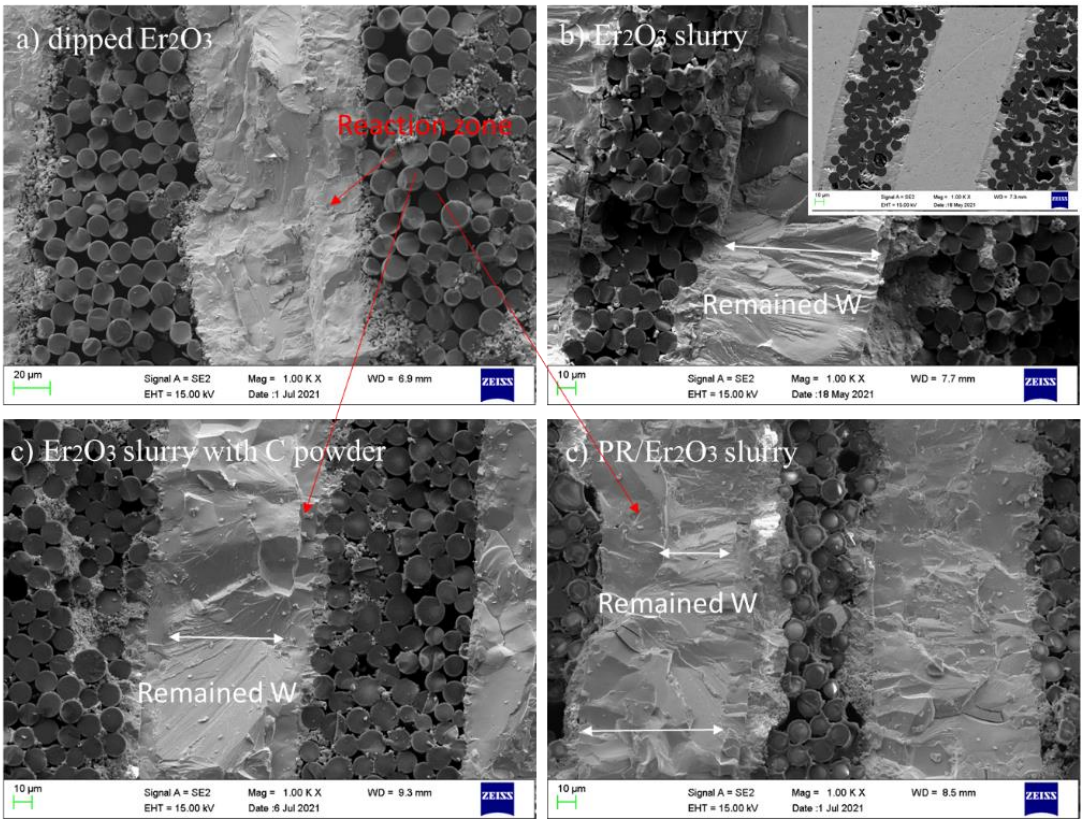

Figure 6.26 The cross-sectional SEM images of unidirectional SiC fiber reinforced W composite with Er_2O_3. a) Er_2O_3 by dipping method; b) Er_2O_3 from slurry; c) Er_2O_3 slurry with C powder; d) C from phenolic resin/ then Er_2O_3 slurry.

To understand the relationship between mechanical property and their structure, the microstructure was observed by SEM with secondary electron mode after tensile test, and the images are revealed in Fig. 6.26. For the composite with Er_2O_3 by dipping method, pull-out fiber and strong reactions can be observed, in which the fiber pull-out effect is responsible for the good pseudo ductility. In addition, almost no Er_2O_3 can be found, indicating that it is difficult to coat Er_2O_3 by dipping method on a circle fiber. Therefore, preparing Er_2O_3 by dipping method is not

appropriate. For the composite with the dispersed Er_2O_3, reactions were hindered successfully. However, strong interface between SiC and Er_2O_3 caused little ductility. With adding C powder, the thickness of reaction zone was 11.2 μm larger than composite just by dispersed Er_2O_3, but lower than composite without diffusion barrier of 34.5 μm. But it is not so efficient to improve the ductility. Pull-out fiber can also be observed in composite PR/Er_2O_3 due to the weak interface between SiC and C, which is the reason why composite displayed the better ductility. Uneven diffusion barrier caused the different thickness of reaction layer.

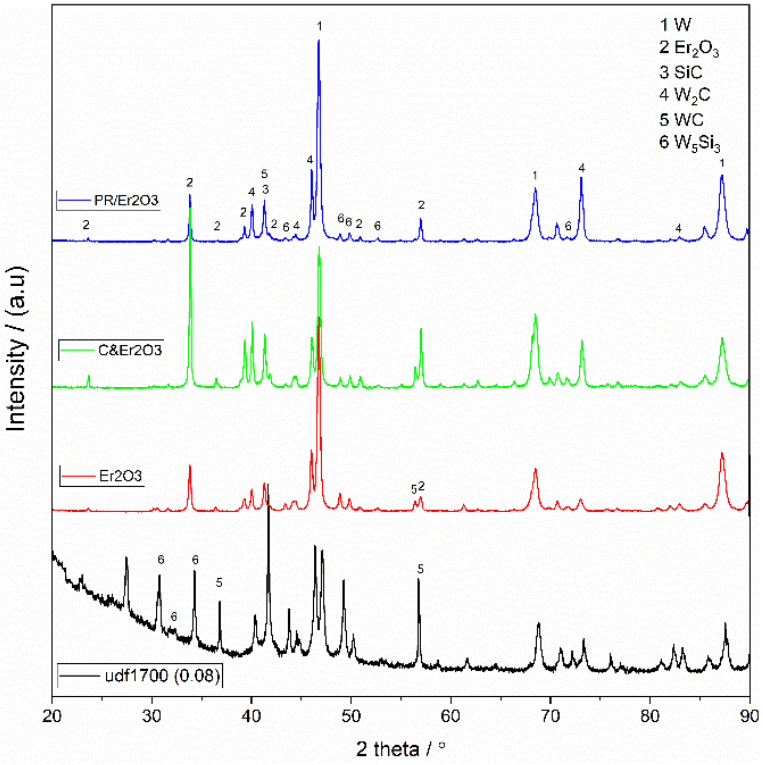

Figure 6.27 The XRD pattern of unidirectional SiC fiber reinforced W composite with Er_2O_3.

The XRD pattern of SiCf/W composites with Er_2O_3 with or without C was identified by Fig. 6.27. The Er_2O_3 in the figure means dispersed Er_2O_3. The generated ceramics can be identified, and the intensity of their peaks reduced a lot compared with composites without Er_2O_3. In addition, the silicides can be prevent successfully, while carbides were measured easily due to smaller size of C atoms.

The mechanical property of Er_2O_3 dispersed SiCf/W composite at 1000 °C was evaluated, and the result is shown in Fig. 6.28. Similar with composite without diffusion barrier (see Fig.

4.11), the fiber and ceramic Er_2O_3 fracture firstly, then the remained W deformed. Finally, the whole composite fracture. For composite with Er_2O_3, the plastic deformation occurred at about 0.5 kN compared with composite without Er_2O_3 deformed at 0.15 kN, indicating that the high ratio of remained W by using Er_2O_3 as diffusion barrier. Before fiber fracture, only very slight composite effect can be measured due to the strong interface between SiC fiber and Er_2O_3.

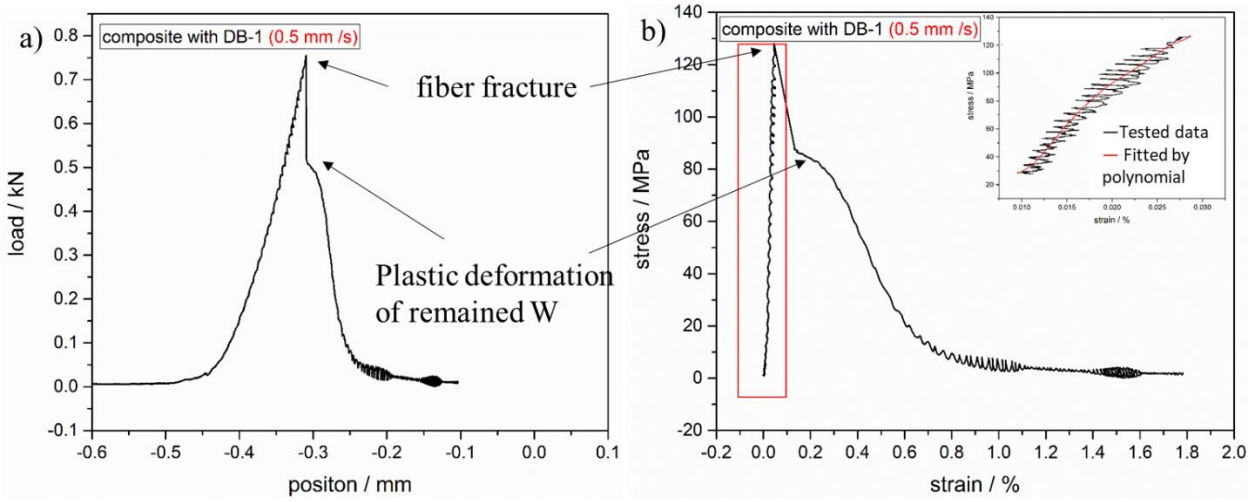

Figure 6.28 The mechanical property of unidirectional SiC fiber reinforced W composite with 0.08 mm foil with Er_2O_3 diffusion barrier measured at 1000 °C.

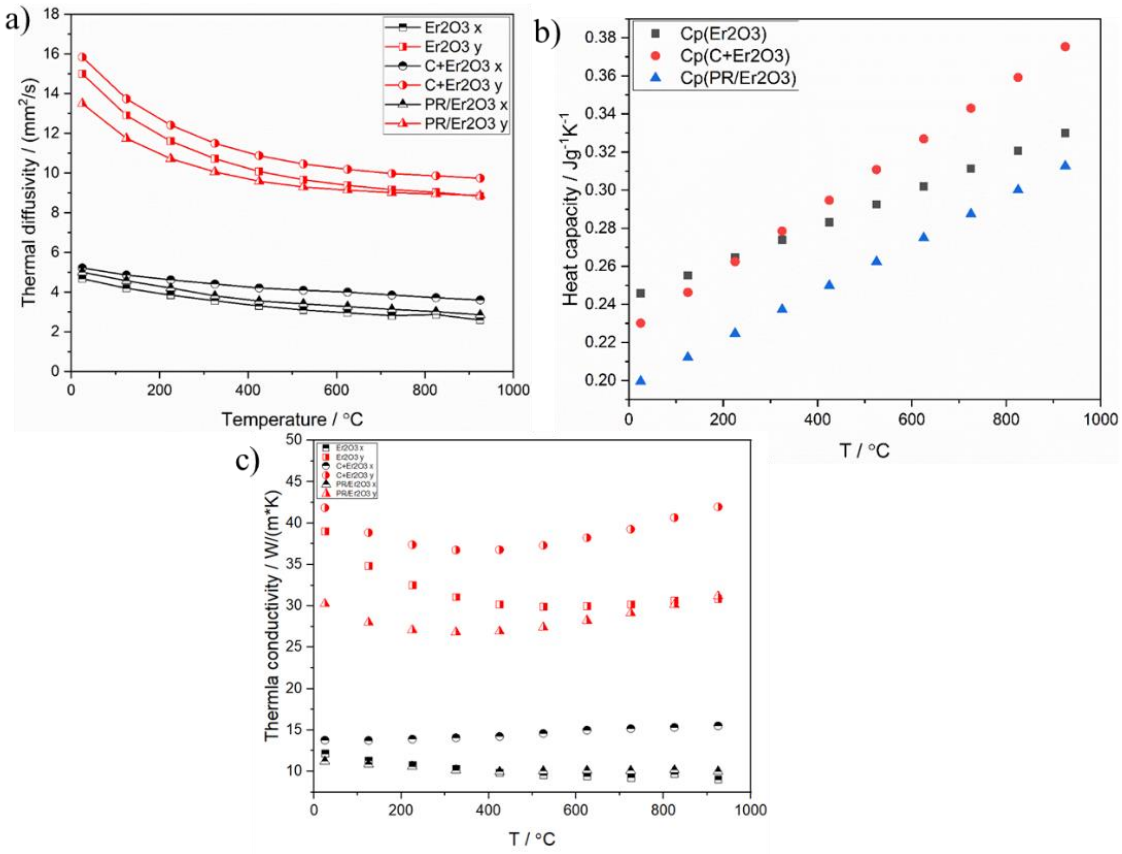

Figure 6.29 The thermal properties of unidirectional SiC fiber reinforced W composite with 0.08 mm foil with Er_2O_3 diffusion barrier fabricated at 1700 °C

The thermal property of SiCf/W composites with dispersed Er_2O_3 with or without C were revealed in Fig. 6.29. The highest thermal conductivity is 42.3 W/(m·K) in composite with Er_2O_3 and C powders, lower than composite without diffusion barrier of 55.6 W/(m·K) even high content of remained W in composite with diffusion barrier. The low thermal conductivity of Er_2O_3 of 6.5 W/(m·K) [31] might be responsible for low thermal conductivity of whole composites. In addition, the contents of Er_2O_3 of 16.63 vol%, 14.17 vol% and 17.21vol% in composites with Er_2O_3, Er_2O_3 and C powder, and PR/Er_2O_3 respectively, are a little high, which consistent with the results of thermal conductivity. Therefore, it is required to decrease the content of oxide with low thermal conductivity.

6.6 Conclusion

Seven materials (oxides (ZrO_2, TiO_2, and Er_2O_3), carbides (ZrC and TiC), and nitrides (ZrN and TiN)) produced by dipping method or sputtering method as diffusion barrier in W and SiC system were investigated by joined with W foils in this work, in order to select a proper interface for SiC fiber reinforced W composite. And for the dipping method after 5 times dipping, the Er_2O_3 coated CVD-SiC joined with W showed the thinnest reaction zone compared with other coatings by dipping method according to the cross-sectional images by SEM. TiO_2 and ZrO_2 film are not suitable as interface in SiC/W case, since reactions between SiC and the oxides can be identified after high temperature annealing. The carbides and nitrides by dipping method cannot work well owing to the defects on the coating because of volume variation generated during heat treatment. While both nitrides coating prepared by sputtering method can act as effective diffusion barrier. Er_2O_3 is also good diffusion barrier in SiC/Mo system. But for interface in composite, weak interface is also necessary to acquire pseudo ductility, so it is not appropriate to coat Er_2O_3 by dipping method on a circle surface. In addition, Er_2O_3 as interface need to investigated further. Besides, long time annealing is still very necessary to be carried out to make sure how long the diffusion barrier can work.

References

[1] T. Koyanagi, Y. Katoh, T. Nozawa, L.L. Snead, S. Kondo, C.H. Henager, M. Ferraris, T. Hinoki, Q. Huang, Recent progress in the development of SiC composites for nuclear fusion applications, J. Nucl. Mater. 511 (2018) 544–555. https://doi.org/10.1016/j.jnucmat.2018.06.017.

[2] H.X. Li, Z.H. Zhong, H.B. Zhang, Z.X. Zhu, P. Hua, C. Chen, Y.C. Wu, Microstructure characteristic and its influence on the strength of SiC ceramic joints diffusion bonded by spark plasma sintering, Ceram. Int. 44 (2018) 3937–3946. https://doi.org/10.1016/j.ceramint.2017.11.185.

[3] S.J. Son, K.H. Park, Y. Katoh, A. Kohyama, Interfacial reactions and mechanical properties of W-SiC in-situ joints for plasma facing components, J. Nucl. Mater. 329–333 (2004) 1549–1552. https://doi.org/10.1016/j.jnucmat.2004.04.285.

[4] H. Kishimoto, T. Shibayama, K. Shimoda, T. Kobayashi, A. Kohyama, Microstructural and mechanical characterization of W/SiC bonding for structural material in fusion, J. Nucl. Mater. 417 (2011) 387–390. https://doi.org/10.1016/j.jnucmat.2010.12.079.

[5] M.A. Umer, D. Lee, O.A. Waseem, H.J. Ryu, S.H. Hong, Fabrication of protective-coated SiC reinforced tungsten matrix composites with reduced reaction phases by spark plasma sintering, Met. Mater. Int. 22 (2016) 493–500. https://doi.org/10.1007/s12540-016-5700-y.

[6] X. Shi, M. Wang, S. Zhang, Q. Zhang, Fabrication and properties of W-20Cu alloy reinforced by titanium nitride coated SiC fibers, Int. J. Refract. Met. Hard Mater. 41 (2013) 60–65. https://doi.org/10.1016/j.ijrmhm.2013.02.002.

[7] Y. Du, T. Hinoki, Effect of tungsten matrix on the mechanical property of SiC fiber reinforced tungsten composites with foils fabricated at 1700 °C, Nucl. Mater. Energy. 31 (2022) 101142. https://doi.org/10.1016/j.nme.2022.101142.

[8] W.F. Seng, P.A. Barnes, Calculations of cobalt suicide and carbide formation on SiC using the Gibbs free energy, Mater. Sci. Eng. B Solid-State Mater. Adv. Technol. 76 (2000) 225–231. https://doi.org/10.1016/S0921-5107(00)00457-8.

[9] H.K. Kang, Microstructures of high volume SiC reinforced tungsten composites produced by plasma spray, Scr. Mater. 51 (2004) 1051–1055. https://doi.org/10.1016/j.scriptamat.2004.08.008.

[10] T. Hinoki, L.L. Snead, C.A. Blue, Development of refractory armored silicon carbide by infrared transient liquid phase processing, J. Nucl. Mater. 347 (2005) 207–216. https://doi.org/10.1016/j.jnucmat.2005.08.020.

[11] Z. Wang, S. DelaCruz, D.S. Tsai, R. Maboudian, W/TaC/SiC sandwich stack for high temperature applications, Ceram. Int. 45 (2019) 22292–22297. https://doi.org/10.1016/j.ceramint.2019.07.255.

[12] S. DelaCruz, Z. Wang, P. Cheng, C. Carraro, R. Maboudian, TiN diffusion barrier for stable W/SiC(0001) interfaces in inert ambient at high temperature, Thin Solid Films. 670

(2019) 54–59. https://doi.org/10.1016/j.tsf.2018.11.058.

[13] J. Roger, F. Audubert, Y. Le Petitcorps, Thermal stability of W-xRe/TiC/SiC systems (x = 0, 5 and 25 at % Re) at high temperature, Adv. Eng. Mater. 11 (2009) 399–407. https://doi.org/10.1002/adem.200800354.

[14] J. Roger, F. Audubert, Y. Le Petitcorps, Reactivity of M/TiN/SiC systems (M = W and Mo) at high temperature, J. Mater. Sci. 45 (2010) 3073–3079. https://doi.org/10.1007/s10853-010-4314-x.

[15] M.A. Golestani Fard, H. Baharvandi, Development of W–ZrC composite coating on graphite by a TIG-aided surface cladding process, Ceram. Int. 47 (2021) 27958–27971. https://doi.org/10.1016/j.ceramint.2021.06.227.

[16] R. Liu, Z.M. Xie, J.F. Yang, T. Zhang, T. Hao, X.P. Wang, Q.F. Fang, C.S. Liu, Recent progress on the R&D of W-ZrC alloys for plasma facing components in fusion devices, Nucl. Mater. Energy. 16 (2018) 191–206. https://doi.org/10.1016/j.nme.2018.07.002.

[17] X.F. Xie, K. Jing, Z.M. Xie, R. Liu, J.F. Yang, Q.F. Fang, C.S. Liu, X. Wu, Mechanical properties and microstructures of W–TiC and W–Y2O3 alloys fabricated by hot-pressing sintering, Mater. Sci. Eng. A. 819 (2021) 141496. https://doi.org/10.1016/j.msea.2021.141496.

[18] H. Kurishita, S. Matsuo, H. Arakawa, T. Sakamoto, S. Kobayashi, K. Nakai, T. Takida, M. Kato, M. Kawai, N. Yoshida, Development of re-crystallized W-1.1%TiC with enhanced room-temperature ductility and radiation performance, J. Nucl. Mater. 398 (2010) 87–92. https://doi.org/10.1016/j.jnucmat.2009.10.015.

[19] D. Lee, M.A. Umer, Y. Shin, S. Jeon, S. Hong, The effect of sintering conditions and ZrN volume fraction on the mechanical properties of spark plasma sintered W/ZrN composites, Mater. Sci. Eng. A. 552 (2012) 481–485. https://doi.org/10.1016/j.msea.2012.05.073.

[20] M. Kim, S. Kim, J. Kang, S.H. Song, D. Lee, Effects of ZrN and W Particle Sizes on the Mechanical and Ablation Properties of ZrN/W Composites, Met. Mater. Int. 25 (2019) 733–739. https://doi.org/10.1007/s12540-018-00226-7.

[21] J. Adachi, K. Kurosaki, M. Uno, S. Yamanaka, Thermal and electrical properties of zirconium nitride, J. Alloys Compd. 399 (2005) 242–244. https://doi.org/10.1016/j.jallcom.2005.03.005.

[22] W. Lengauer, Transition Metal Carbides, Nitrides, and Carbonitrides, Handb. Ceram. Hard Mater. (2008) 202–252. https://doi.org/10.1002/9783527618217.ch7.

[23] R.W. Harrison, W.E. Lee, Processing and properties of ZrC, ZrN and ZrCN ceramics: a review, Adv. Appl. Ceram. 115 (2016) 294–307. https://doi.org/10.1179/1743676115Y.0000000061.

[24] T. Chikada, A. Suzuki, Z. Yao, A. Sawada, T. Terai, T. Muroga, Basic study on self-healing of Er2O3 coating for vanadium-lithium blanket system, Fusion Eng. Des. 82 (2007) 2572–2577. https://doi.org/10.1016/j.fusengdes.2007.03.020.

[25] F. Xiao, Q. Miao, S. Wei, Z. Li, T. Sun, L. Xu, Microstructure and mechanical properties

of W-ZrO2 alloys by different preparation techniques, J. Alloys Compd. 774 (2019) 210–221. https://doi.org/10.1016/j.jallcom.2018.09.321.

[26] B. Jasper, S. Schoenen, J. Du, T. Hoeschen, F. Koch, C. Linsmeier, R. Neu, J. Riesch, A. Terra, J.W. Coenen, Behavior of tungsten fiber-reinforced tungsten based on single fiber push-out study, Nucl. Mater. Energy. 9 (2016) 416–421. https://doi.org/10.1016/j.nme.2016.04.010.

[27] J. Riesch, J.Y. Buffiere, T. Höschen, M. Scheel, C. Linsmeier, J.H. You, Crack bridging in as-fabricated and embrittled tungsten single fibre-reinforced tungsten composites shown by a novel in-situ high energy synchrotron tomography bending test, Nucl. Mater. Energy. 15 (2018) 1–12. https://doi.org/10.1016/j.nme.2018.03.007.

[28] T. Morimoto, T. Ogasawara, Potential strength of Nicalon^{TM}, Hi Nicalon^{TM}, and Hi Nicalon Type S^{TM} monofilaments of variable diameters, Compos. Part A Appl. Sci. Manuf. 37 (2006) 405–412. https://doi.org/10.1016/j.compositesa.2005.05.046.

[29] D.R. Hummer, P.J. Heaney, J.E. Post, Thermal expansion of anatase and rutile between 300 and 575 K using synchrotron powder X-ray diffraction, Powder Diffr. 22 (2007) 352–357. https://doi.org/10.1154/1.2790965.

[30] R. Dargis, D. Williams, R. Smith, E. Arkun, R. Roucka, A. Clark, M. Lebby, Structural and Thermal Properties of Single Crystalline Epitaxial Gd 2 O 3 and Er 2 O 3 Grown on Si(111) , ECS J. Solid State Sci. Technol. 1 (2012) N24–N28. https://doi.org/10.1149/2.005202jss.

[31] M. Alsboul, M.S.M. Ghazali, M.R. Gomaa, A. Albani, Experimental and Theoretical Investigations of the Thermal Conductivity of Erbium Oxide/Ethylene Glycol Nanofluids for Thermal Energy Applications, Chem. Eng. Technol. 45 (2022) 2139–2149. https://doi.org/10.1002/CEAT.202200159.

Chapter 7 Summary and Recommendation for Future Development

7.1 Summary

Radiation hardening is a phenomenon that can cause metals to become brittle over time. In order to improve the brittleness of tungsten (W) and molybdenum (Mo), a novel method of toughening metals based on SiC-based fibers reinforcement is proposed. This method is intended for use in structural materials that are utilized in thermonuclear fusion reactors. The objective of this thesis is to develop new composites that are reinforced by SiC-based fiber in order to exhibit ductile behavior even after irradiation. The toughening mechanism of these composites is similar to that of fiber-reinforced ceramic matrix composites, which results from the debonding and friction that occurs at the fiber/matrix interface. The composites were fabricated using hot press technology. In order to optimize the fiber reinforced composite, this study investigated the effect of fiber types, matrix, and sintering temperature on mechanical and thermal properties, from both in-plane and through-plane directions, as well as microstructure. Two sintering methods were used to sinter the 2D woven SiC fiber, with and without a powder sheet. The study also explored the potential diffusion barrier between SiC and brittle metals. In the following, the main results of this study will be discussed.

Effect of sintering temperature on properties and microstructure

Unidirectional (UD) Hi-Nicalon type S SiC fiber was used to reinforce W composites manufactured by hot press successfully. The stress-strain curves obtained at room temperature, lower than the ductile-brittle transition temperature (DBTT) of W, showed obvious pseudo-ductile behavior for specimen sintered until 1700 °C. So SiC fiber as reinforcement to strengthen W is feasible. But the ultimate tensile strength (UTS) is low and the highest value is 82.9 MPa in composite sintered at 1700 °C. Considering thermal conductivity, higher sintering temperature led to higher thermal conductivity. In addition, it is much higher in in-plane direction than through-plane direction. The composites sintered at 1700 °C showed the largest strength with pseud ductility. Therefore, the suitable sintering temperature to fabricate SiC/W composite is 1700 °C.

Effect of matrix on properties and microstructure

Metal foils were used as matrix in this work. W foils with 0.05 mm and 0.08 mm thickness and Mo foil with 0.08 mm were selected. The recrystallization temperature of foils was examined by annealing at high temperature. For W foils, the temperature is between 1200 °C and 1400 °C

independent of their thickness. In addition, the temperature of Mo foil is between 1000 °C and 1200 °C. All foils have recrystallized during sintering. Therefore, there is no contribution for ductility of composites from foil. Continuous unidirectional SiC fiber reinforced W composites with 0.05 mm or 0.08 mm foil as matrix were sintered at 1700 °C, and reinforced Mo composite with 0.08 mm foil was sintered at 1500 °C successfully. The tensile test implies that the W based composites obtained with 0.08 foil showed better apparent pseudo-ductile behavior due to the short pull-out fiber and foil with higher ultimate tensile strength (UTS) of 197 MPa. In addition, the pseudo ductility can also be found in Mo-based composite with the UTS of 109 MPa, worse than it of W composite. In addition, the thermal conductivity of Mo composite is also lower than W composite. Therefore, the best composite is unidirectional SiC/W composite with 0.08 mm foil. Besides, it is demonstrated that composite with suitable interface or diffusion barrier show better property.

Effect of fiber types on properties and microstructure

Three kinds of fiber, woven SiC fiber, unidirectional SiC fiber, and 2D SiC and W fiber reinforced W composites with foils were prepared. For SiC woven fiber by two methods, the results show that the method without powder sheet is more appropriate than that with powder sheet due to composite by powder sheet with foils delaminated during machining. In addition, all composites displayed pseudo-ductile behavior at room temperature. In addition, the strength of both composites by both 2D fibers were higher than the 50 % strength of UD composite, because only half fibers work in composites reinforced by 2D fibers. Therefore, 2D fibers are better than UD fiber. For thermal property, the composite reinforced by 2D W/SiC fiber shows higher conductivity at high temperature especially in through-plane direction compare with composites without W wire by introducing W wire with high conductivity. Therefore, it can be speculated that SiC/W woven fiber might be more suitable combined the thermal property and mechanical property.

The potential diffusion barriers between metals and SiC

Seven materials (oxides (ZrO_2, TiO_2, and Er_2O_3), carbides (ZrC and TiC), and nitrides (ZrN and TiN)) produced by dipping method or sputtering method as diffusion barrier in W and SiC system were investigated by joined with W foils to select a proper interface for SiC fiber reinforced W composite. And for the dipping method after 5 times dipping, the Er_2O_3 coated CVD-

SiC joined with W showed the thinnest reaction zone. In addition, 29.5 μm thick Er_2O_3 can work until 1950 °C. Er_2O_3 was also used in SiC/Mo joint, and it works at least 1800 °C. Unidirectional SiC fiber reinforced W with 0.08 mm foil with Er_2O_3 composite was sintered at 1700 °C. The SiC fiber can be protected well, but the pseudo ductility reduced due to strong interface between fiber and matrix. After adding C, the pseudo ductility can also be found. However, the strength and thermal conductivity is lower than composite without diffusion barrier. Therefore, the most appropriate interface in composite needs to be studied further.

7.2 Recommendation for future development

In this work, a novel toughening method for brittle metals, retaining toughness even under room temperature successfully, which is the embrittlement conditions, was proposed and developed based on the reinforcement of SiC fiber. The best composite in this work is (UD) SiCf/W with 0.08 mm foil without diffusion barrier fabricated by method without powder sheet at 1700 °C by hot press. Because 1700 °C is appropriate temperature to balance between high density to obtain high strength and weak interface to acquire pseudo ductility. Fiber reinforcement can ameliorate the brittle metals, and show pseudo-ductility at room temperature, lower than their DBTT. Therefore, there is no need to care about the radiation embrittlement. In addition, it can be assumed that pseudo-ductile behavior will be obtained in the composite even if metal as matrix is brittle caused by neutron irradiation. This work provides a guideline to improve the toughness of brittle metals as a structural material in fusion reactor. However, strength was sacrificed in some extent caused by the reaction between W and SiC. For working as diffusion barrier, Er_2O_3 is suitable. However, it is not suitable to contact to SiC directly, an inner thin (~200 nm) pyrolytic carbon (PyC) before coating Er_2O_3 is required. In addition, dipping method to coat Er_2O3 on fiber is not appropriate. Chemical vapor deposition (CVD) might be suitable. Moreover, another idea is to change the fabrication method from hot press to CVD by reducing the sintering temperature or to spark plasma sintering by reducing the holding time. In addition, it is necessary to carry out the neutron irradiation experiment after optimizing the composite.

Publication list

1 Y. Du, B. Wang, Y. Zhong, T. Hinoki, Assessment of the Potential Diffusion Barriers between Tungsten and Silicon Carbide for Nuclear Fusion Application, Coatings 2022, Vol. 12, Page 639. 12 (2022) 639. https://doi.org/10.3390/COATINGS12050639.

2 Y. Du, T. Hinoki, Effect of Sintering Temperature on Properties of SiC Fiber Reinforced Tungsten Matrix Composites, Mater. Trans. 63 (2022) 1550–1556. https://doi.org/10.2320/MATERTRANS.MT-M2022043.

3 Y. Du, T. Hinoki, Effect of tungsten matrix on the mechanical property of SiC fiber reinforced tungsten composites with foils fabricated at 1700 °C, Nucl. Mater. Energy. 31 (2022) 101142. https://doi.org/10.1016/j.nme.2022.101142.

Conference list

1.Yina Du, Bo Huang, Kanjiro Kawasaki, Fujio Shinoda and Tatsuya Hinoki，Effect of tungsten matrix on mechanical properties of SiC fiber reinforced W composite; 2020.9 AESJ, Oral.

2.Yina Du，Tatsuya Hinoki，Thermal stability of tungsten and SiC with or without diffusion barrier (ZrN and TiN) at 1700 °C, 2021.3 AESJ, Oral.

3.Yina Du，Tatsuya Hinoki，Effect of Er_2O_3 interphase on SiC fiber reinforced W composites；2021.9 AESJ. Oral.

4.Yina Du，Tatsuya Hinoki, Effect of the Thickness of Tungsten Foil on Mechanical Property of SiC Fiber Reinforced W Composites；The International Conference on Fusion Reactor Materials (ICFRM-20), 2021.10 AESJ. Poster.